Thesis advisor: Professor Katia Bertoldi Sicong Shan

Planar Soft Functional Periodic Structures Exploiting Instabilities And Large Deformation

Abstract

Soft materials can significantly change their shape and volume when subjected to various stimuli. Materials with deliberately designed periodic microstructure have long been proved to be characterized by properties that may exceed those of the corresponding bulk material. Though traditionally avoided as modes of failure, mechanical instabilities have recently been exploited to design systems with novel and tunable functionalities. Interestingly, the studies I conducted during my PhD show that the combination of soft materials, periodic structures, mechanical instabilities and large deformation give us the opportunity to design materials and structures with enhanced functionality.

In this thesis, I present a systematic study on the response of planar soft functional materials which use their large deformation and geometric rearrangements to dramatically change their properties. In particular, I used a combination of experiments and numerical simulations to investigate the effect of important parameters, such as pore shape, hole arrangement and loading conditions. With the fundamental understanding I gained, I developed a novel class of planar soft periodic materials with enhanced material functionalities such as tunable phononic band-gap, spontaneous symmetry breaking, chirality amplification and energy trapping. Remarkably, since the continuous 2D soft and porous structures I studied take advantage of reversible and scale-independent mechanisms, the proposed designs can be applied over a wide range of length scales.

The studies presented here show that by mastering the interplay between the microstructure of soft periodic structures and their large deformation behavior, novel materials with enhanced func-

tionalities can be designed, which may result in a generation of switchable devices and inspire new horizons for materials research.

Contents

Listing of figures

Dedicated to my parents, family and friends, and those who *INSPIRED* me

Acknowledgments

THOUGH only my name appears on the cover of this dissertation, a great many people have contributed to its production. I owe my gratitude to all those people who have made this dissertation possible and because of whom my graduate experience has been one that I will cherish forever.

First, I would like to express my heartiest gratitude to my PhD advisor Professor Katia Bertoldi. Katia has always been such an excellent engineer, caring mentor and enlightening teacher. I was so lucky to be admitted into the group five years ago. In the past five years, I learned from Katia in every of our meetings. Every meeting with her was extremely illuminative. She has tremendous enthusiasm in mechanics, and avidly pushing the frontier of traditional solid mechanics. I enjoy taking Katia's courses and love reading her class notes. The notes are as clear and complete as a book of manual. Her incredible inspiration and perseverance kept carrying me forward through the struggling periods. I really appreciate her not dropping me out during the most unproductive and tough days in my life. Thanks, Katia. I will miss you so much.

I am also deeply grateful to my long-term colleague, Dr. Sung Hoon Kang, who is now Professor at John Hopkins University. Most part of my thesis is based on a collaboration with him. We have

worked together closely since my second semester at Harvard, and we have shared the same office for the past three years. The difference in background and expertise allowed us to challenge and complete each other. Although as an experimentalist, Sung thinks deeper than theoreticians and understands all the details of the projects. His critical advise in the discussion are always helpful. We shared the happiness and frustration through the projects. I felt lucky to have Sung for the most part of my PhD.

It has been a joyful and inspiring research ride for past years with people in my group. I want to thank all those great colleagues: Sahab Babaee, Fionnuala Connolly, August Domel, Jia Hong Ray Ng, Johannes TB (Bas) Overvelde, Pai Wang, Jia Liu, Dr. Farhad Javid, , Dr. Michael Taylor, Dr. Filippo Casadei, Dr. Tianxiang Su, Michael Galli, Dr. Luca Francesconi. Also, the experience to work with and supervise the visiting students has been rewarding. Working in a advisory role allowed me to look inside myself as a mini PI. And I learned a lot during the process. For this, I want to thank Lichen Fang, Shuang Liu, Yushen Sun, Yao Xiao, Zhenhao Zhen, Yang Lai, Cangyu Qu, Yiwei Guo and Tianyu Gu.

Many other colleagues and collaborators at SEAS have been extremely generous with me, and have educated me through discussion and example; the incomplete list includes Qihan Liu, Jianyu Li, Kechao Xiao, Prof. Kejie Zhao. I am grateful for the welcome and support I received at the MIT, where I spent an aggregate of half a year doing experiments in Prof. Pedro Reis's lab and Prof. Nick Fang's lab. In particular, Prof. Pedro Reis, Mo Chen, Prof. Howon Lee provided an invaluable guidance to me.

I also want to thank my committee members, Professor Zhigang Suo, Professor David Clarke, and Professor Shmuel Rubinstein, for their suggestions and comments to my research.

This PhD work would not have come true if I had not been at Harvard. I thank Harvard University for the opportunity to work closely with phenomenal scientists, colleagues, staff. Throughout the course of my PhD, Harvard community has been a true privilege.

I have also been very fortunate to receive recognition from my own home country for my research as the awardee of Chinese Government Award for Outstanding Students Abroad from China Scholarship Council (CSC), which named me in the top 1% among all Chinese student who are studying overseas. I am truly thankful and humbled for this. This award also came in time to buoy up me during the most dark days of my PhD. I have to thank my home country for her constant support for me as an overseas student.

Most importantly, none of this would have been possible without the love and patience of my family. My family to whom this dissertation is dedicated to, has been a constant source of love, concern, support and strength all these years. I would like to express my heart-felt gratitude to my wife, and my parents. I cannot say thank you enough. And of course, thanks to my baby daughter, my little princess, Yu-An, who has just start teaching me, with bittersweetness, a lift-long lesson to be a real man and a good father.

1

Introduction

1.1 Soft materials

Soft materials, such as elastomers and gels, can undergo large deformation in response to diverse stimuli, including force, voltage, temperature, pH, salinity, and trace amount of enzymes. An elastomer may strain easily more than 100% under an applied force. A gel can absorb a large quantity of solvent and swell a thousand times its initial volume. From the theoretical point of view, several

efforts have been devoted to construct constitutive models that accurately describe the macroscopic mechanical behavior of such materials subjected subjected to finite deformations [66,160,185,114,108,48,4].

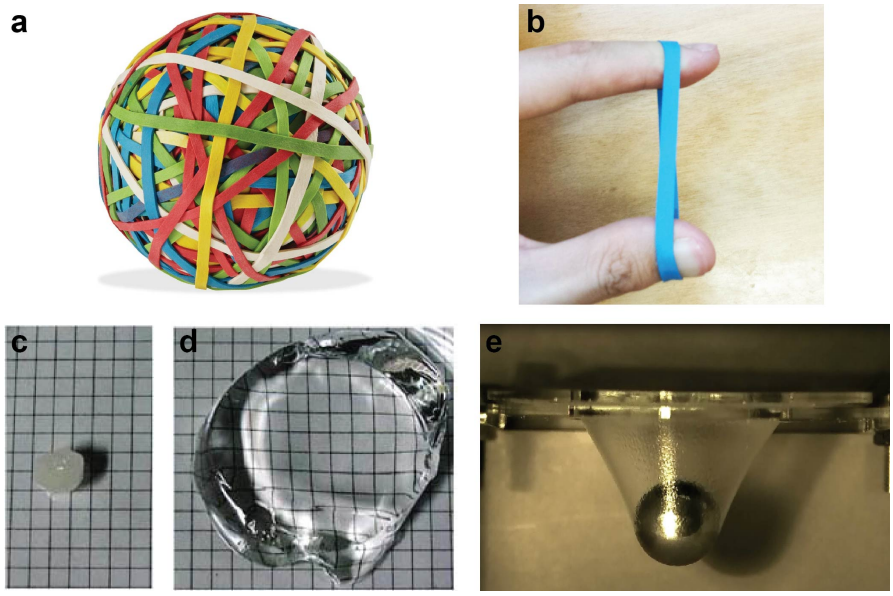

Figure 1.1: Examples of soft materials: a) Rubber bands arranged to form a sphere (from Amazon.com); b) A rubber band highly stretched by my hand; c)d) Dramatic volume change between the dry and swollen state of a gel [29]; e) Hydrogel largely deformed upon impact [159].

Moreover, an exciting field of engineering is emerging that uses soft materials to design a new class of active devices. Intense efforts are being made to develop soft materials for applications such as artificial muscles [133], implantable biomedical sensors [134], organic electronics [95,84], soft robots [70] and adaptive optics [183].

1.2 Periodic Structures

Materials with significant porosity, generally termed cellular solids, exhibit properties that differ from those of their solid counterparts [50] and have a large number of uses in mechanical and thermal applications. It has also been shown that the response of cellular solids can be enhanced by rationally designing a periodic microstructure. In fact, periodic porous materials offer novel and unique

properties, including light weight[137], high energy absorption[94], and the ability to control the propagation of both electromagnetic[138], elastic waves[88,103] and heat flow[102].

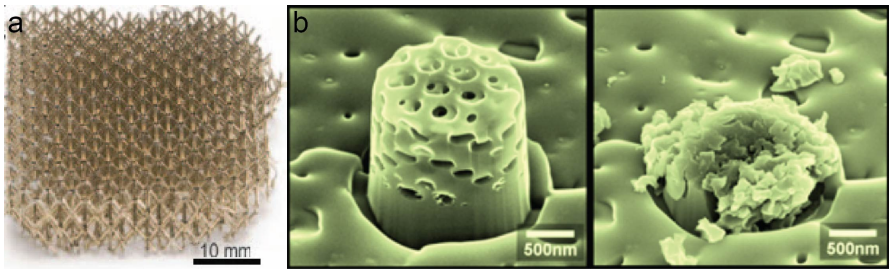

Figure 1.2: Examples of periodic structure: a)light weight structure [137]; b)underformed/deformed high energy absorption periodic structure [94].

1.3 Instabilities and large deformation

Although traditionally instabilities have been viewed as an inconvenience, buckling need not to be deleterious: buckling plays an important role in the morphogenesis of some plant parts[145,140]; the surface pattern of a dehydrated fruit is dominated by buckling[186]; bacteria use buckling to change direction[152]. Inspired by nature researchers have recently demonstrated instabilities to be instrumental in facilitating flexible electronics[78], fabricating micro-fluidic structures[79], controlling surface wettability[82], providing means for micro- and nano-patterning[100] and designing optical micro-devices[23], guiding cell alignment in tissue matrices[101].

1.4 Combining soft materials, periodic structures, instabilities and large deformation

Recently mechanical instabilities in soft planar periodic porous structures have received considerable attention because of the dramatic pattern transformations they generate[110,189,146]. Upon reaching a critical applied stress, a square array of circular holes in an elastomeric matrix is found to suddenly

transform into a periodic pattern of alternating, mutually orthogonal ellipses (see Figure 1.3). Interestingly, this parallel, cooperative buckling instability - a kind of "phase transition" from one to another - have been been demonstrated to be instrumental for the design materials with tunable properties, including systems with tunable negative Poisson's ratio[13], phononic[10,71,175] and photonic[87] switches and color displays[97].

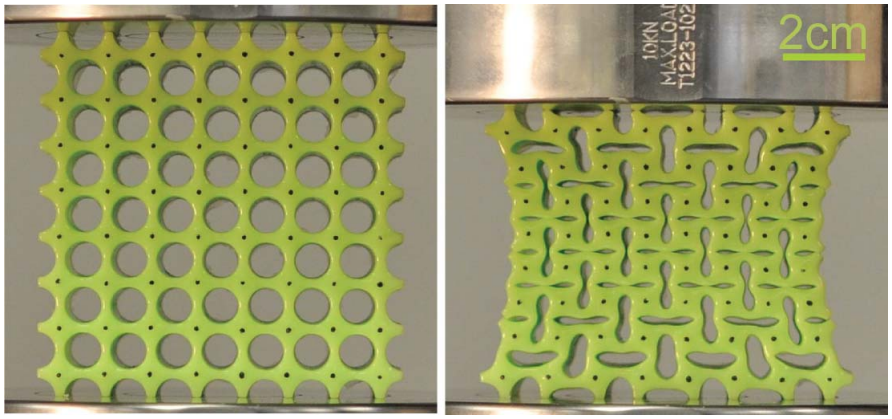

Figure 1.3: Upon reaching a critical applied deformation, a square array of circular holes in an elastomeric matrix suddenly transform into a periodic pattern of alternating, mutually orthogonal ellipses.

1.5 Goals and structure of this thesis

During my PhD I worked at the intersection of soft materials, periodic structures, instability & large deformation. In particular, I focused on 2D soft periodic structures and

1. developed an understanding of their non-linear behavior;
2. rationally designed systems that take advantage of their large deformation;
3. demonstrated possible exciting applications such as the design of deployable soft structures, tunable phononic crystals and energy trapping materials.

To achieve the goals outlined above, I studied:

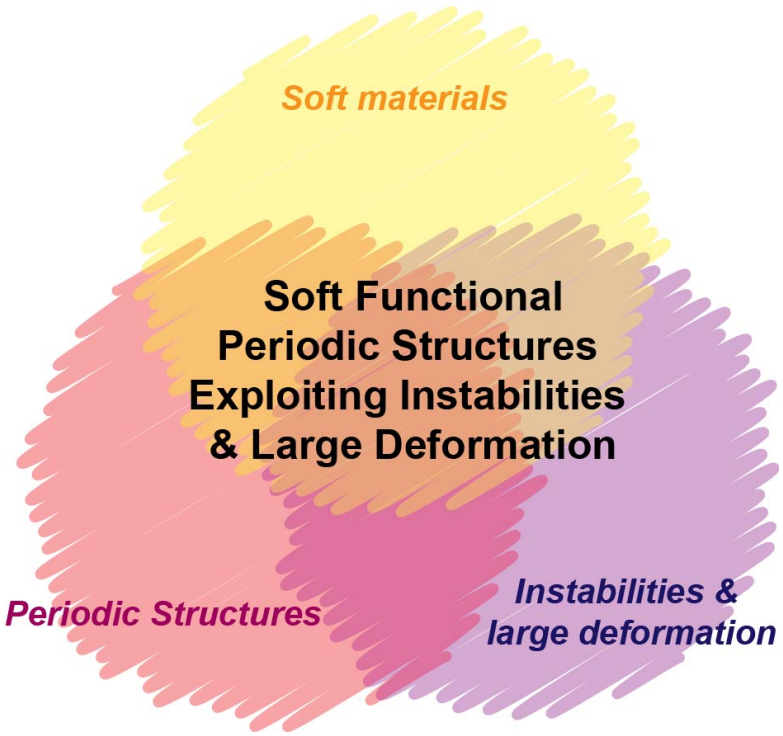

Figure 1.4: During my PhD I studied how soft materials, periodic structures, instability and large deformation can be combined to design new class of functional materials.

1. the effect of pore shape on the compaction of 2D periodic, soft and porous structures (Chapter 2).

2. the effect of hole arrangements in the design of soft reconfigurable auxetic/chiral materials (Chapter 3)

3. principles for designing planar isotropic negative Poisson's ratio structures (Chapter 4)

4. multiple folding mechanisms in soft periodic structures for tunable control of elastic waves (Chapter 5)

5. mechanism of buckling-induced reversible symmetry breaking in supported cellular structures (Chapter 6).

6. snap-through instability for the design of shape-recoverable, scale- and rate-independent energy-absorbing structures (Chapter 7)

This project was a collaboration with J. T. B. Overvelde under the supervision of Prof. Katia Bertoldi. I was the equal contribution author on this project. My role involves experiments, analysis and assistance in preparation of manuscript. The work in this chapter has already been published and the relevant citation is: Overvelde, J. T. B.†, Shan, S.†, Bertoldi, K. (2012). Compaction Through Buckling in 2D Periodic, Soft and Porous Structures: Effect of Pore Shape. Adv Mater, 24(17), 2337-2342.*

2

Compaction Through Buckling in 2D Periodic, Soft and Porous Structures: Effect of Pore Shape

2.1 Introduction

Adaptive structures allowing dramatic shape changes offer unique opportunities for the design of responsive and reconfigurable devices. Artificial morphing and foldable structures have traditionally been fabricated using stiff structural members connected by mechanical joints[124,28,1,64,86,178], resulting in a very challenging manufacturing process at small length scales. In contrast, there are many examples of soft adaptive structures in nature: mimosa leaves fold when touched[176,123], venus flytraps open and close to catch prey[44], and mechanical expansion and contraction of the pigment-filled sacks in squids result in dynamic color changes[161]. Applying these natural design principles in new ways could result in a novel class of responsive and reconfigurable devices. Soft structures where the folding mechanisms are induced by a mechanical instability may lead to origami materials that can be easily manufactured over a wide range of length scales. Possible and exciting applications include active materials for on-demand drug delivery, colorful and reconfigurable displays and robots that can squeeze themselves through small openings and into tight spaces.

Soft structures with deliberately designed patterns may significantly change their architecture in response to diverse stimuli[72,149], opening avenues for reconfigurable devices that change their

shape to respond to or alter their environment. Two-dimensional periodic porous structures recently attracted considerable attention because of dramatic transformations of the original geometry observed as the result of mechanical instabilities[110,189,147]. Upon reaching a critical applied stress, a square array of circular holes in an elastomeric matrix is found to suddenly transform into a periodic pattern of alternating, mutually orthogonal ellipses (see Fig. 2.2A). This behavior has been demonstrated to provide opportunities for the design of materials with tunable negative Poisson's ratio[14], phononic switches[71] and reprogrammable colorful displays[87]. However, so far only the response of structures with circular and elliptical holes has been investigated and the effect of the pores shape on the structural response has not been explored yet.

Shape plays an important role in the design and performance of materials and engineering devices. Computer analysis - known as shape and topology optimization[37,9,61] - is performed routinely in an effort to identify optimal shapes to improve a certain performance under some constraints. In this study we will investigate both numerically and experimentally the effect of pore shape on the non-linear response of a square array of holes in a soft matrix. The hole shape is found to provide a convenient parameter to control attractive features of soft porous systems, such as their compaction (quantified as change of structure planar area divided by original area) and negative Poisson's ratio (although the Poisson's ratio is rigorously defined in the framework of linear elasticity, here we extend the concept to finite elasticity and use it to quantify the lateral contraction/expansion of the material.). Our results show that the pore shape can be used effectively to design material with desired properties and pave the way for the development of a new class of soft, active and reconfigurable devices over a wide range of length scales.

2.2 Methods

2.2.1 Definition of pore shapes

Here, we focus on holes with four-fold symmetry and make use of Fourier series expansion to describe their contour as

$$x_1 = r(\vartheta)\cos\vartheta, \qquad x_2 = r(\vartheta)\sin\vartheta, \tag{2.1}$$
$$\text{with } r(\vartheta) = r_0\left[1 + c_1\cos(4\vartheta) + c_2\cos(8\vartheta)\right],$$

where $0 \leq \vartheta \leq 2\pi$ and three parameters have been introduced to control the pore size (r_0) and shape (c_1 and c_2). While $c_1 = c_2 = 0$ in Equation 2.1 provides a description of a circle of radius r_0, by varying c_1 and c_2 a variety of shapes can be obtained, as shown in Figure 2.1. Thus, in terms of optimization, c_1 and c_2 represent a 2D design space which allows for a systematic study of the effect of shape on the compaction of the structures.

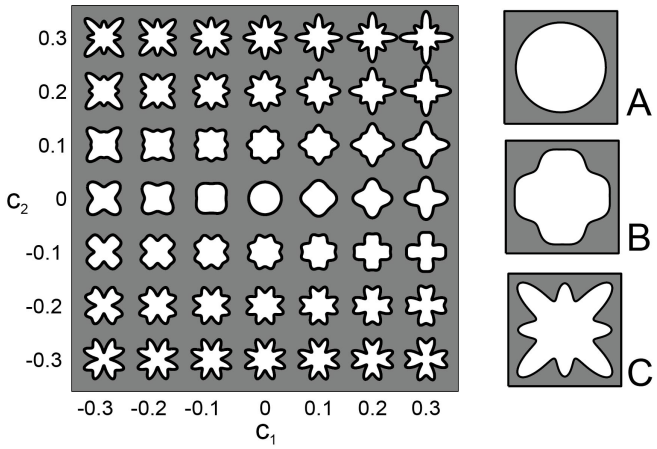

Figure 2.1: Left: Shapes obtained using Eqn. 2.1 and c_1=c_2=-0.3:0.1:0.3, while keeping r_0 constant. Right: Representative volume elements (RVEs) for the three shapes considered in this work, defined by $(\varphi^A, c_1^A, c_2^A) = (0.46, 0, 0)$, $(\varphi^B, c_1^B, c_2^B) = (0.47, 0.11, -0.05)$ and $(\varphi^C, c_1^C, c_2^C) = (0.44, -0.21, 0.28)$

To clearly identify the effect of shape on the material response, we focus on a specific arrangement of the pores and consider holes arranged on a square array, so that r_o is related to the porosity of the structure φ through

$$r_o = \frac{L_o\sqrt{2\varphi}}{\sqrt{\pi(2 + c_1^2 + c_2^2)}}, \tag{2.2}$$

with L_o denoting the center-to-center distance between neighboring holes in the undeformed configuration. Note that, to preserve the structural integrity, c_1 and c_2 have to be chosen such that $0 \leq x_1 \leq L_o/2$ and $0 \leq x_2 \leq L_o/2$.

While the results of an extensive numerical study on the effect of c_1 and c_2 on the non-linear material response are reported by Overvelde *et al*[118], here we will focus on two shapes showing qualitative and quantitative remarkably different behaviors, highlighting the important role played by the pore shape. The response of a soft structure with circular holes defined by $(\varphi^A, c_1^A, c_2^A) = (0.46, 0, 0)$ is compared to that of structures with pores defined by $(\varphi^B, c_1^B, c_2^B) = (0.47, 0.11, -0.05)$ and $(\varphi^C, c_1^C, c_2^C) = (0.44, -0.21, 0.28)$ (see Fig. 2.1). Note that the slight variation in porosity between the three structures is related to limited accuracy during the fabrication process.

2.2.2 Modeling and Analysis

Physical and numerical models of elastomeric structures consisting of 8x8 unit cells (or representative volume elements, RVEs) arranged on a square array were built as shown in Figs. 2.2(a) and (d).

Experiment

We used rapid prototyping techniques to fabricate the samples made out of a soft silicone-based rubber. Molds were fabricated using laser-cutting. Each mold comprised a base, four lateral walls and hundred spines to shape the contour of the pores. All parts were laser-cut from acrylic plates by a VersaLaser system and assembled together. Spines with desired thickness were fabricated stacking

several layers of acrylic plates and were inserted into the base using a hexagonal shaped key to orient them. Each mold comprised a 10 $\times$ 10 square array of holes with center-to-center spacing $L_o = 10mm$. The mold was open to the air, and the casted mixture(Vinylpolysiloxane from Zhermack. Inc.) was allowed to set at room temperature for 20 minutes. After demolding, the side walls were cut from the sample, leaving seven columns of seven holes, flanked by a column/row of seven semi holes on either sides (Fig. 2.2). The specimens for structures A, B and C measured $80 \times 80 \times 14.5mm$, $80 \times 80 \times 18.5mm$, $80 \times 80 \times 15.5mm$, respectively. The porosity of three specimens was measured as $\varphi^A = 0.46$, $\varphi^B = 0.47$ and $\varphi^C = 0.44$.

The final structures comprise a square array of 8x8 holes and to reduce the boundaries effect the RVEs closest to all boundaries are cut in half. All structures are measured to have a center-to-center distance between neighboring holes $L_o = 10\,mm.$ was used to fabricate the structures; uniaxial tension test performed on the bulk material revealed that its response up to a stretch of 2 is well captured using an incompressible Neo-Hookean model, with Young's modulus $E^* = 190kPa.$ The structures were then compressed at constant speed of 20 mm/min, while a video was captured and recorded by a high-resolution digital camera facing the specimen. During the tests out-of-plane buckling was prevented holding the specimens with a back plate). (more details of the manufacturing and experimental procedures are given in *Materials and Methods*

Simulation

To fully understand the effect of pore shape on the material response, numerical simulations were performed using the non linear finite element code ABAQUS/Explicit. Triangular, quadratic plane strain elements (ABAQUS element type CPE6M) were used and the accuracy of the mesh was ascertained through a mesh refinement study, resulting in a relative mesh density of around 800 to 1250 elements per RVE. An imperfection in the form of the first buckling mode (determined by a linear buckling analysis) was introduced in order to exclude the possibility of the simulation to fol-

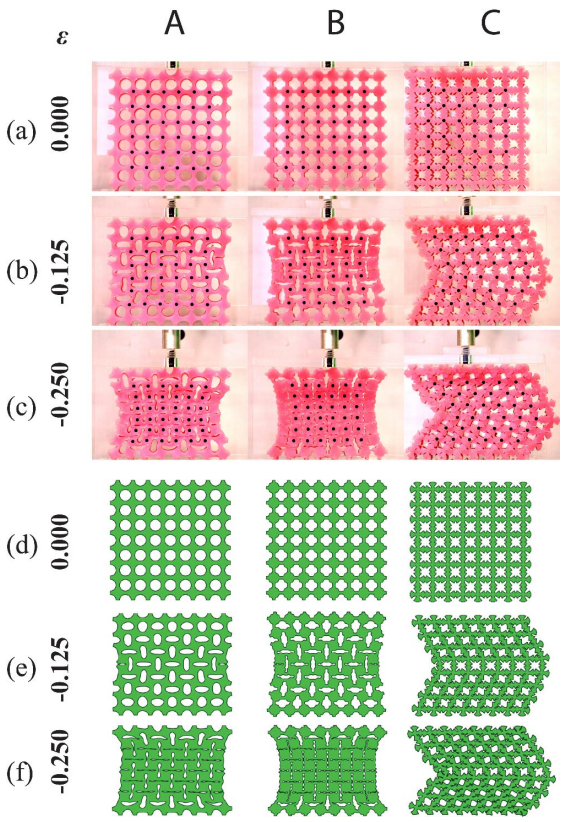

Figure 2.2: Experimental (top) and numerical (bottom) images of structures A, B and C at different levels of applied engineering strain $\varepsilon = 0, -0.125, -0.25$.

low an unstable deformation-path. Quasi-static conditions were ensured by monitoring the kinetic energy and introducing a small damping factor. In the simulations clamped conditions between the specimen and the horizontal fixtures were assumed to simplify the non-adhesive frictional boundary conditions occurring in the experiment.

2.3 Results

All the three structures were uniaxially compressed in vertical direction ensuring quasi-static conditions and representative pictures taken during the tests at different level of applied compressive engineering strain ε are presented in Fig. 2.2, showing excellent agreement between experiments and simulations. First, we observe that when a critical value of the compressive strain is reached, buckling occurs, leading to rapid and dramatic changes of the material microstructure. As can be clearly seen in Figs. 2.2(b) and (e) at a strain $\varepsilon = -0.125$ all three structures have buckled. Remarkably, the shape of the holes is found to strongly affect the instability. In structures A and B the critical instability is characterized by a wavelength equal to $2\,L_o$ in both vertical and horizontal direction and leads to the formation of a checkerboard pattern (see Figs. 2.2(b) and (e)). By contrast, a buckling mode with a wavelength equal to the size of the sample is observed in structure C, reminiscent of the twinning observed in austenite to martensite phase transformations in shape memory alloys[89].

Once formed, the new pattern becomes further accentuated for increased values of the applied strain, as can be seen in Fig. 2.2(c) and (f). Remarkably after unloading, the initial shape of the holes was always fully recovered regardless of the amount of applied deformation. Moreover, close inspection of Fig. 2.2 reveals that the hole shape not only affects the buckling of the structures, but also attractive features such as their lateral contraction and compaction. In structures A and B complete closure of the pores and a significant lateral contraction is observed at $\varepsilon = -0.25$, leading to a folded state characterized by an area reduction of $\backsim$ 40%. By contrast, a significantly lower area change at

$\varepsilon = -0.25$ is found in structure C, highlighting the important role played by microscopic instabilities (i.e. instabilities with wavelengths that are of the order of the size of the microstructure) in the design of novel, soft and foldable systems. Finally, comparison of the pattern in structures A and B at $\varepsilon = -0.25$ clearly shows that circular holes do not lead to optimal compaction; an optimized folded configuration that minimized the openings is found in structure B, demonstrating the significant effect that the pore shape has in the design of foldable soft structures.

A more quantitative comparison between the response of the structures investigated in this paper can be made by inspecting the evolution of stress, negative Poisson's ratio and compaction monitored during both experiments and simulations. Figure 2.3(a) presents the evolution of the nominal stress S (calculated by dividing the total applied force by the initial cross-sectional area) as function of the applied engineering strain ε (calculated as change of structure height divided by original height). For all three structures we observe a behavior typical for cellular solids with three distinct regimes[50]: a linear elastic regime, a stress plateau following thereafter, and densification by further compression. The departure from linearity is a result of buckling and corresponds to a sudden transformation in the periodic pattern as shown in the snapshots of deformed configurations at different levels of strain (Fig. 2.2). Eventually, at high strains, the holes collapse sufficiently for their boundary to touch, giving rise to the final steep portion of the stress-strain curve. Although all our structures are characterized by a very similar initial elastic response, their departure from linearity is well separated and it is found to strongly depend on the pore shape.

It is surprising to observe that the least porous structure (i.e. structure C) is characterized by the lowest buckling stress. This observation clearly confirms that the buckling observed in structures A and B is different in nature from that of structure C and that the shape of the holes has a strong effect on mechanical instability. While structures A and B are characterized by microscopic instabilities, a macroscopic instability (i.e. instability with a much larger wavelength than the size of the microstructure) is observed in structure C.

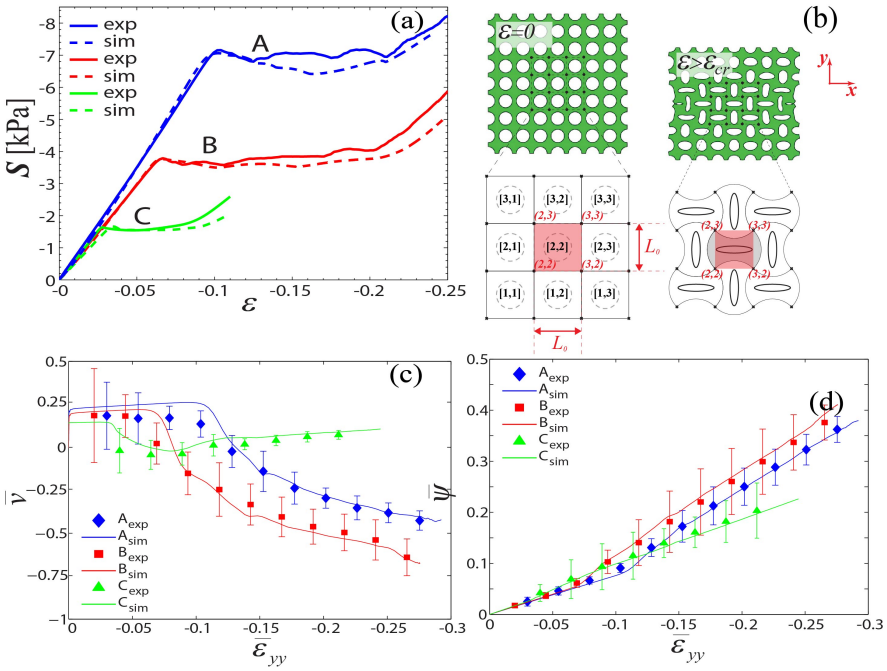

Figure 2.3: (a) Experimental and numerical stress-strain curves for the three structures. Solid curves correspond to experiments and dash lines to simulations. (b) Schematic diagram of the central region with 9 RVEs. (c) Evolution of Poisson's ratio $\bar{\nu}$ as a function of local compressive strain $\bar{\varepsilon}_{yy}$ for the three structures. Markers correspond to experiments and continuous lines to simulations. (d) Evolution of compaction $\overline{\psi}$ as a function of $\bar{\varepsilon}_{yy}$ for the three structures.

2.3.1 Poisson's ratio and foldability

To monitor the evolution of the microstructure, we focused on the behavior of the central part of the sample (nine RVEs) where the response was clearly more uniform and not affected by the boundary conditions. The vertices of the nine central RVEs were marked with black dots (see Fig. 2.3(b)) and their position was recorded using a high-resolution digital camera and then analyzed by digital image processing (Matlab). For each RVE, local values of the engineering strain, $\varepsilon_{xx}^{[i,j]}$ and $\varepsilon_{yy}^{[i,j]}$, were calculated from the positions of the markers, $x^{(i,j)}$ and $y^{(i,j)}$, as

$$\begin{aligned} \varepsilon_{xx}^{[i,j]} &= \frac{x^{(i+1,j)} - x^{(i,j)} + x^{(i+1,j+1)} - x^{(i,j+1)} - 2L_\circ}{2\,L_\circ} \\ \varepsilon_{yy}^{[i,j]} &= \frac{y^{(i+1,j+1)} - y^{(i+1,j)} + y^{(i,j+1)} - y^{(i,j)} - 2L_\circ}{2\,L_\circ}, \end{aligned} \tag{2.3}$$

where $i, j = 1, 2, 3$ and $L_\circ = 10mm$ denotes the distance between markers in the undeformed configuration. The local values of the engineering strain were used to calculate local values of the Poisson's ratio as

$$\nu^{[i,j]} = -\frac{\varepsilon_{xx}^{[i,j]}}{\varepsilon_{yy}^{[i,j]}}, \tag{2.4}$$

and of compaction as

$$\psi^{[i,j]} = \frac{A_\circ^{[i,j]} - A^{[i,j]}}{A_\circ^{[i,j]}} = 1 - (1 + \varepsilon_{xx}^{[i,j]})(1 + \varepsilon_{yy}^{[i,j]}), \tag{2.5}$$

$A^{[i,j]}$ and $A_\circ^{[i,j]}$ denoting the current and initial area of the $[i - th, j - th]$ RVE. Moreover, since the material used to fabricate the structures was incompressible and the change in thickness during the test was found to be negligible

$$A_\circ^{[i,j]} - A_{\circ,p}^{[i,j]} = A^{[i,j]} - A_p^{[i,j]}, \tag{2.6}$$

$A_{\circ,p}^{[i,j]}$ and $A_p^{[i,j]}$ denoting the area of the pores within $[i-th, j-th]$ RVE in the initial and deformed configuration, respectively. Combining Eqns. 2.5 and 2.6 a relation between compaction and porosity of the $[i-th, j-th]$ RVE is obtained as

$$\psi^{[i,j]} = 1 - \frac{1-\varphi_\circ^{[i,j]}}{1-\varphi^{[i,j]}}, \tag{2.7}$$

where $\varphi_\circ^{[i,j]} = A_{\circ,p}^{[i,j]}/A_\circ^{[i,j]}$ and $\varphi^{[i,j]} = A_p^{[i,j]}/A^{[i,j]}$ denote the initial and current porosity of the considered RVE. Then the ensemble averages $\bar{\varepsilon}_{yy} =< \varepsilon_{yy}^{[i,j]} >$, $\bar{\nu} =< \nu^{[i,j]} >$, $\overline{\psi} =< \psi^{[i,j]} >$ for the nine central RVEs under consideration were computed.

The evolution of the Poisson's ratio $\bar{\nu}$ as function of the local engineering strain $\bar{\varepsilon}_{yy}$ is presented in Fig. 2.3(c). The difference between structure C and structures A and B is striking; while in structures A and B noticeable lateral contraction induced by buckling is observed, eventually leading to negative values of Poisson's ratio, the Poisson's ratio in structure C is only marginally affected by deformation and buckling. Moreover, it is interesting to observe that the lateral contraction in structure B is remarkably larger than that observed in structure A, leading to larger negative values of Poisson's ratio.

The evolution of the compaction $\overline{\psi}$ for the three structures (Fig. 2.3(d)) shows similar features to that of the Poisson's ratio. Microscopic instabilities in structure A and B are found to lead to a significant increase in compaction, revealing the important role played by buckling in the design of novel soft foldable systems. As clearly shown in Figs. 2.2 and 2.3, using mechanical instabilities and different pore shapes, materials and devices can be designed capable of dramatic area and shape change in response to an external stimulus, opening avenues for novel active and soft foldable structures.

2.4 Discussion

Our results demonstrate the important role of the shape of the pores on the response of 2D porous structures. We reveal that the shape of the pores can be effectively used to tune their lateral contraction and compaction. To fully unravel the effect of the shape of the holes on the physical characteristics of the structures, we proceed by systematically investigating the effect of porosity φ on their response. Since our results clearly show that the finite element simulations were able to accurately reproduce the experimental results, we now investigate numerically the response of structures characterized by porosity φ ranging between 0.4 and 0.5. Note that smaller values of porosity would facilitate macroscopic instability[14], leading to structures characterized by limited compaction. On the other hand, higher levels of porosity would lead to structures characterized by very thin ligaments, making them fragile.

In Fig. 2.4(a) the evolution of the initial elastic modulus E, normalized by the Young's modulus of the bulk material E^*, is reported as a function of the porosity φ. The pore shape is found to strongly affect E/E^*; structures B and C both show an initial elastic modulus significantly lower than structure A and similarly we may expect to exploit the pore shape to design structures with stiffer initial elastic response.

Focusing on the non-linear response of the structures, Fig. 2.4(b) shows the buckling strain ε_{cr} for the three structures as a function of φ. Over the explored range of porosity, we found that structures A and B are always characterized by microscopic modes, while for structure C a macroscopic mode is observed. This difference is reflected by the different dependence of ε_{cr} by φ: for structure C ε_{cr} in only marginally affected by φ, while it shows a much stronger dependency for structures A and B.

Finally in Figs. 2.4(c) and (d) we investigated the effect of porosity on lateral contraction and compaction at a fixed local strain $\bar{\varepsilon}_{yy}$=-0.2. Structure C is found to be characterized by a limited compaction over the entire range of porosity explored in this study. Differently, we observe a significant

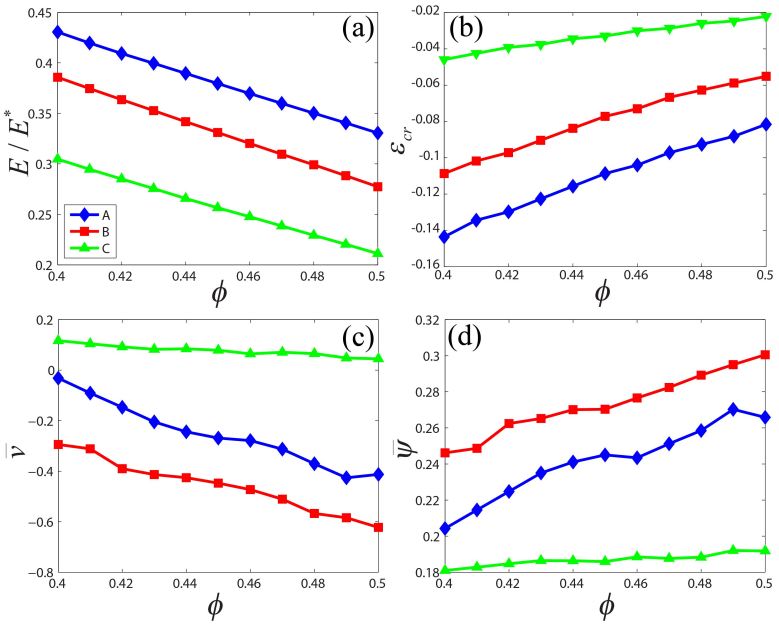

Figure 2.4: Results of the numerical investigation on the effect of the porosity φ for the three structures. (a) Effective modulus E/E^*. (b) Critical strain ε_{cr}. (c) Poisson's ratio $\bar{\nu}$ at a local strain $\bar{\varepsilon}_{yy} = -0.2$. (d) Compaction $\overline{\psi}$ at a local strain $\bar{\varepsilon}_{yy} = -0.2$.

increase of $\bar{\nu}$ and $\overline{\downarrow}$ in structures A and B with increased values of porosity. Moreover, the results clearly show the superior response of structure B in terms of compaction and lateral contraction over the entire range of porosity. More precisely, at a given level of porosity the negative Poisson's ratio and compaction for structure B are found to be more than 20% larger than those of structure A. Thus the numerical results strongly confirm the important effect of pore shape both on the initial and non-linear response of the structures and demonstrate that shape can be exploited to fine tune their mechanical response.

2.5 Conclusion

We have shown that cellular solids, which comprise a solid matrix with a square array of holes, open avenues for the design of novel soft and foldable structures. Unlike many other examples of foldable structures, our system does not contain rigid links, but comprises continuous 2D soft and porous structures and takes advantage of mechanical instabilities, allowing the actuation to be fast, reversible and applicable over a wide range of length scales. Our results demonstrate that by simply changing the shape of the holes the response of porous structure can be easily tuned and soft structures with optimal compaction can be designed. Surprisingly, we show that circular holes do not lead to optimal response and that the compaction of the system can be significantly improved through a careful design of the pore shape. The insights gained by performing a numerical parametric exploration serve as an important design guideline in fabricating practical materials towards applications.

This project was a collaboration with Jongmin Shim, Andrej Košmrlj, Sung H. Kang, Elizabeth R. Chen, James C. Weaver under the supervision of Prof. Katia Bertoldi. I was one of the lead researchers on this project and equal contribution author. I helped in formulating the idea, and I worked on experiments and part of simulations, and preparation of the manuscript. The work in this chapter has already been published and the relevant citation is: Shim, J.†, Shan, S.†, Kosmrlj, A., Kang, S. H., Chen, E. R., Weaver, J. C., Bertoldi, K. (2013). Harnessing instabilities for design of soft reconfigurable auxetic/chiral materials. Soft Matter, 9(34), 8198-8202.*

3

Harnessing instabilities for design of soft reconfigurable auxetic/chiral materials

3.1 Introduction

Mechanical instabilities are not always deleterious though they are conventionally regarded as failure modes. Because of the large deformation and dramatic shape changes that accompany them [69,187],

mechanical instabilities in elastic structures provide opportunities for designing responsive materials capable of reversibly switching between two different configurations with applications in sensors, microfluidics, bioengineering, robotics, acoustics and photonics [22,67,83,141,71,182]. In particular, instabilities in periodic porous structures comprising of square and triangular arrays of circular holes have been found to lead to the transformation of the pores in ordered arrays of high-aspect ratio (almost closed) ellipses [110,189,146] and have been demonstrated to be instrumental for the design of phononic switches [71], color displays [97] and materials with unusual properties such as large negative Poisson's ratio [117,14]. However, to design the next generation of responsive and reconfigurable materials and devices that take advantage of the dramatic changes in geometry induced by instabilities, the effect of pore shape and lattice topology on the response of the system need to be fully understood. While it has been recently shown that the pore shape has a strong effect both on the onset of instability and on the postbuckling behavior [117], there has been no systematic study on the effect of the hole arrangement. So far the selection of the architecture has been guided by intuition and buckling has been exploited as a folding mechanism only in square and triangular arrays of holes [110,71,97,117,14,149].

Here, we first identify possible periodic distributions of mono-disperse circular holes where buckling can be exploited to reversibly switch between expanded (i.e. with circular holes) and compact (i.e. with elongated, almost closed elliptical holes) periodic configurations. Then, we confirm the validity of our findings through a combination of experiments and numerical simulations. While two of these four configurations have been previously reported [110,12,189], the other two are newly discovered. Remarkably, in these two new configurations elastic buckling not only can be exploited to design materials with negative Poisson's ratio(also known as auxetic material), but also acts as a reversible chiral symmetry-breaking mechanism, enabling the reversible switch between the initial nonchiral and the buckled chiral pattern. Furthermore, since the proposed folding mechanism exploits mechanical instabilities, our study opens avenues for the design of reconfigurable materials over a wide range of length scales.

3.2 Identification of potential hole arrangements

We start by finding periodic monodisperse circular hole arrangements in plates where buckling can be exploited as a mechanism to reversibly switch between undeformed/expanded and deformed/compact configurations. Therefore, we require that the instability does not only reduce the symmetry, but also leads to the transformation of the circular holes into elongated (almost closed) ellipses. Inspired by recent work on buckling of spherical structured shells, where hole arrangements were systematically explored through polyhedra[141], here we investigate the hole arrangements by considering geometric constraints on the tilings (i.e., tessellations) of the 2D Euclidean plane.

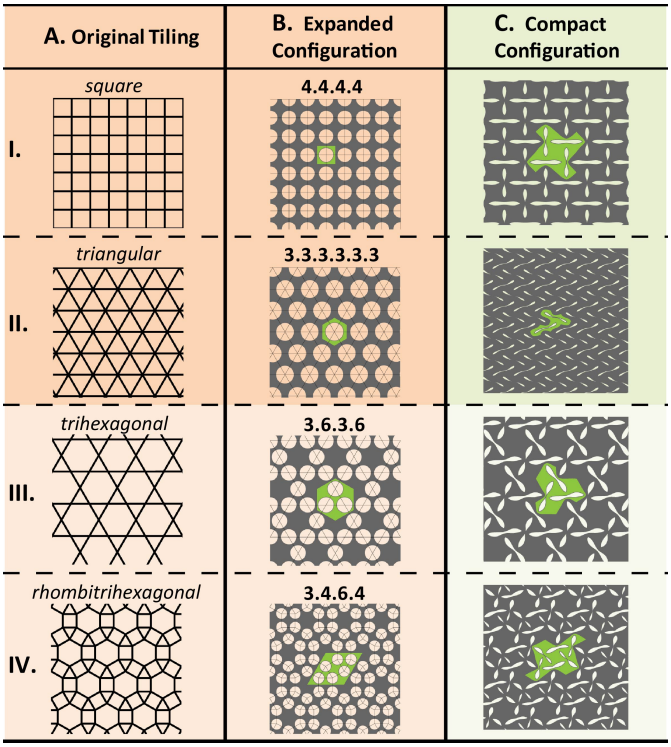

Figure 3.1: Geometric compatibility for the arrangement of circular holes on the porous structures, restricted to four specific configurations (shown in each row). (A) Tilings. (B) Expanded undeformed porous structures. (C) Compact porous structures, which are buckled under uniaxial compression. The green-shaded regions in (B) and (C) denote the unit cell in the undeformed and deformed configurations, respectively.

In order for all the monodisperse circular holes to close through buckling of the ligaments, the plates should meet the following requirements: (a) the center-to-center distances of adjacent holes are identical, so that all the ligaments are characterized by the same minimum width and undergo the first buckling mode in an approximately uniform manner; (b) there is an even number of ligaments around every hole, so that the deformation induced by buckling leads to their closure. Mathematically, these geometric constraints can be rephrased as: the skeleton of the porous structure should (a') be a convex uniform tiling of the 2D Euclidean plane (which are vertex-transitive and have only regular faces) (b') with an even number of faces meeting at each vertex. Focusing on convex uniform tilings (*i.e.* Platonic and Archimedean tilings) where all the vertices are the same, so that all the holes deform similarly, we find that there are only four tessellations which meet the above requirements: *square tiling*, *triangular tiling*, *trihexagonal tiling* and *rhombitrihexagonal tiling* (see Fig. 3.1-A). Note that these tilings can be fully described by their vertex figure (i.e. a sequence of numbers representing the number of sides of the faces going around the vertex): 4.4.4.4 for the square, 3.3.3.3.3.3 for the triangular, 3.6.3.6 for the trihexagonal and 3.4.6.4 for the rhombitrihexagonal tiling. The corresponding porous structures are then obtained by placing a circular hole at each vertex of the tiling (Fig. 3.1-B & Chapter B. To help us refer to to these four periodic porous structures, hereafter we use the vertex figure of the corresponding tiling to denote them, as indicated in Fig. 3.1-B. Fig. 3.1-C shows the compact/folded configurations of the porous structures, which are obtained through finite element (FE) buckling analysis under uniaxial compression. They clearly show that all the ligaments in the structures undergo the first buckling mode uniformly. The instability is found not only to change the planar symmetry group of the structures (i.e. for 4.4.4.4 from *p4m* to *p4g*, for 3.3.3.3.3.3 from *p6m* to *pgg*, for 3.6.3.6 from *p3m1* to *p3*, and 3.4.6.4 from *p6m* to *p6*), but also to lead to closure of the holes and compaction of the structures. It is worth noting that the same compact patterns can also be predicted using continuum elasticity theory and modeling each buckled elliptical hole as a dislocation dipole that interacts elastically with all the other dipoles

in the system[105] (see Chapter B).

3.3 Experiment and simulation methods

Guided by our analysis, we built physical and numerical models of all four porous structures (see Fig. 3.2-A). The structures are characterized by an initial void-volume-fraction $\psi_{4.4.4.4} = \psi_{3.6.3.6} = \psi_{3.4.6.4} = 0.49$ and $\psi_{3.3.3.3.3.3.} = 0.48$ (ψ = total hole area/total area). Note that the slight variation in porosity between the four structures is related to limited accuracy during the fabrication process. The samples for the experiments were fabricated using silicone rubber with Young's modulus $E = 0.9\ MPa$ and a mold-casting process with molds prepared by 3D rapid prototyping. In all the structures, the holes are characterized by radius $r = 4\ mm$ and a large out-of-plane thickness is employed to avoid out-of-plane buckling. Uniaxial compression tests were performed on a standard quasi-static loading frame under displacement-control (see *Supporting Information* for details on the experimental setup). On the numerical side, simulations were performed using the non-linear Finite Element(FE) code ABAQUS/Standard. Plane strain conditions were assumed and the behavior of the silicone rubber used in the experiments was captured using the Yeoh hyperelastic model[185]. Uniaxial compression tests were simulated by imposing vertical displacements at the top face, while keeping all other degree of freedom of both top and bottom faces fixed (see *Supporting Information* for details on the FE simulations).

3.4 Discussion

Representative pictures taken during the tests at different levels of nominal strain ε (calculated as change of height divided by the original height) are presented in Fig. 3.2, showing an excellent agreement between experiments and FE simulations. At small nominal strains, the holes are observed to deform uniformly (see Fig. 3.2-B). However, when a critical value of applied nominal strain is

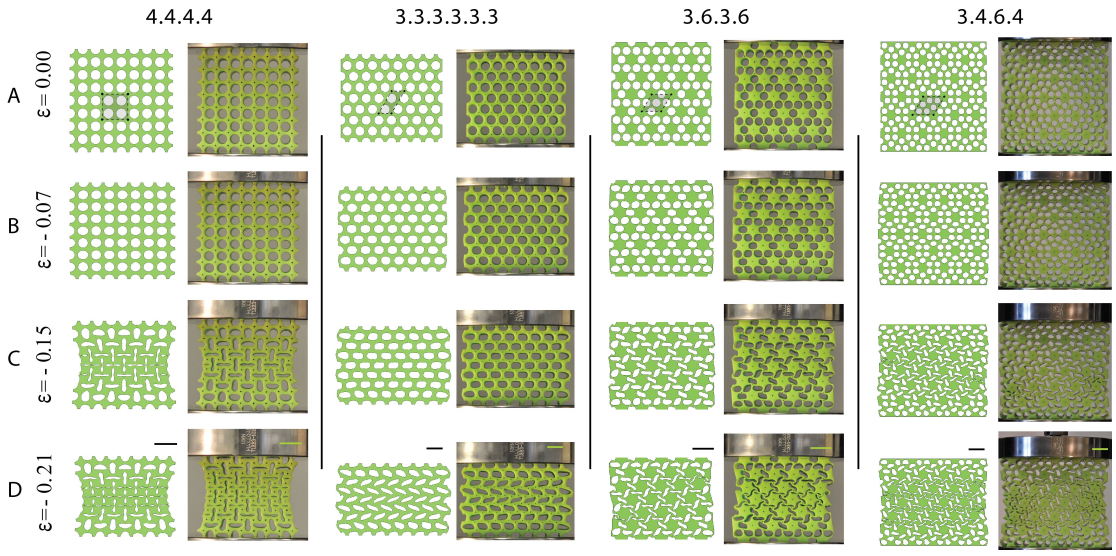

Figure 3.2: Numerical (left) and experimental (right) images of all four structures (4.4.4.4, 3.3.3.3.3.3, 3.6.3.6 and 3.4.6.4) at different levels of deformation: (A) $\varepsilon = 0.00$, (B) $\varepsilon = -0.07$, (C) $\varepsilon = -0.15$ and (D) $\varepsilon = -0.21$. All configurations are characterized by an initial void-volume-fraction $\psi \approx 0.5$. Scale bars: $20mm$.

reached, the thin ligaments between the holes start to buckle in a uniform manner. Eventually, at $\varepsilon = -0.15$ (Fig. 3.2-C), a distinctive buckled pattern is observed in the central part of the samples, only marginally affected by the boundary conditions. Finally, the buckled pattern becomes further accentuated for larger values of applied strain, leading to the formation of a periodic array of elongated, almost closed ellipses, as shown in Fig. 3.2-D for $\varepsilon = -0.21$. Since the specimens are made of an elastomeric material, the process is fully reversible and repeatable. Upon release of the applied vertical displacement, the deformed structures recover their original configurations.

Interestingly, Fig. 3.2-C and 3.2-D clearly shows that the porous structures 3.6.3.6 and 3.4.6.4 buckle into a chiral pattern, while the initially expanded configurations are non-chiral. Therefore, in these two systems buckling acts as a reversible chiral symmetry breaking mechanism. Despite many studies on pattern formation induced by mechanical instabilities[149], relatively little is known about the use of buckling as a reversible chiral symmetry breaking mechanism. Although several processes have been recently reported to form chiral patterns[34,125,41,58,99], all of these work only at a specific

length-scale, preventing their use for the formation of chiral structures over a wide range of length scales, as required by applications. Furthermore, most of these chiral symmetry breaking processes are irreversible[34,125,41] and only few systems have been demonstrated to be capable of reversibly switching between non-chiral and chiral configurations[58,99]. Remarkably, since the mechanism discovered here exploits a mechanical instability that is scale independent, our results raise opportunities for reversible chiral symmetry breaking over a wide range of length scales.

A

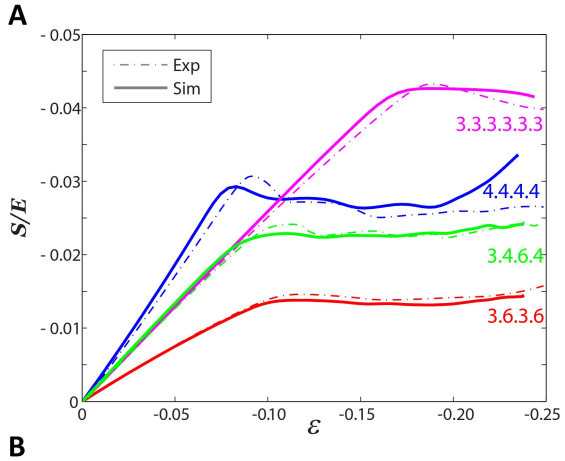

B

	4.4.4.4	3.3.3.3.3.3	3.6.3.6	3.4.6.4
$\overline{E}/E$ (Exp)	0.361	0.245	0.144	0.227
$\overline{E}/E$ (Sim)	0.373	0.254	0.145	0.234
ε_{cr} (Exp)	−0.090	−0.187	−0.112	−0.107
ε_{cr} (Sim)	−0.083	−0.169	−0.111	−0.097

Figure 3.3: (A) Experimental and numerical stress-strain curves for the four structures. S denotes the nominal stress (calculated as force divided by the cross -sectional area in the undeformed configuration). Dashed lines correspond to experiments and solid lines to simulations. Note that for $\varepsilon < -0.20$ the porous structure 4.4.4.4. shows a stiffening behavior due to densification. A similar response is observed also for the other three structures, but for larger values of applied strain ε.(B) Table summarizing the mechanical properties of the four periodic structures measured from experiments and simulations.

Both experiments and simulations reported in Fig. 3.2 clearly indicate that the onset of instability is strongly affected by the arrangement of the holes. A more quantitative comparison between

the response of the structures investigated in this paper can be made by inspecting the evolution of stress during both experiments and simulations (see Fig. 3.3). Although all structures are characterized by roughly the same porosity, the hole arrangement is found to strongly affect both the effective modulus $\overline{E}$ (calculated as the initial slope of the stress-strain curves reported in Fig. 3.3) and the critical strain ε_{cr} (calculated as the strain at which the stress-strain curves reported in Fig. 3.3 plateau), demonstrating that through a careful choice of the architecture materials with the desired response can be designed.

Finally, a feature that is clear in Fig. 3.2 is that after instability the lateral boundaries of three samples (i.e. 4.4.4.4, 3.6.3.6.and 3.4.6.4) bend inwards, a clear sign of negative Poisson's ratio[90,38]. To quantify the lateral contraction (and thus the negative Poisson's ratio) of the porous structures, we investigate the evolution of the microstructure during both experiments and simulations. The physical samples were marked with black dots (see Fig. 3.2) and their position was recorded using a high-resolution digital camera and then analyzed by digital image processing (MATLAB). We focused on the central part of the samples where the response was clearly more uniform and marginally affected by the boundary conditions. For each structure we constructed several parallelograms connecting the markers in the central part of the sample (see Figs. 3.2-A and 3.4-A and *Supporting Information* for details) and monitored their evolution. For each parallelogram, local values of the engineering strain ε_{xx} and ε_{yy} were calculated from the positions of its vertices at each recorded frame t as

$$\varepsilon_{xx}(t) = \frac{(x_4(t)-x_3(t))+(x_2(t)-x_1(t))}{2|\mathrm{L}^{\circ}_{34}|} - 1, \tag{3.1}$$

$$\varepsilon_{yy}(t) = \frac{\big(y_1(t)-y_3(t)\big)+(y_2(t)-y_4(t))}{2|\mathrm{L}^{\circ}_{13}|\cos} - 1, \tag{3.2}$$

where $(x_i,\ y_i)$ denote the coordinates of the i-th vertex of the parallelogram, $|\ \mathrm{L}^{\circ}_{34}\ |$ and $|\ \mathrm{L}^{\circ}_{13}\ |$ are the norm of the lattice vectors spanning the parallelogram in the undeformed configuration (see

Fig. 3.4-A) and $\vartheta = \arccos \frac{L^{\circ}_{34} \cdot L^{\circ}_{13}}{|L^{\circ}_{34}||L^{\circ}_{13}|}$. The local values of the engineering strain were then used to calculate local values of the Poisson's ratio as

$$\nu(t) = -\frac{\varepsilon_{xx}(t)}{\varepsilon_{yy}(t)}, \tag{3.3}$$

and

$$\nu_{inc}(t) = -\frac{\varepsilon_{xx}(t+\Delta t) - \varepsilon_{xx}(t)}{\varepsilon_{yy}(t+\Delta t) - \varepsilon_{yy}(t)}. \tag{3.4}$$

Note that ν characterizes the lateral contraction/expansion of the structure with respect to the initial/undeformed configuration. Differently, ν_{inc} quantifies the lateral contraction/expansion with respect to the deformed configuration induced by an increment in the applied strain $\Delta\varepsilon$ and allow us to describe the Poisson's ratio of a material that operates around a pre-deformed state. Finally, the ensemble averages $\bar{\varepsilon}_{xx} =< \varepsilon_{xx} >$, $\bar{\varepsilon}_{yy} =< \varepsilon_{yy} >$, $\bar{\nu} =< \nu >$, and $\bar{\nu}_{inc} =< \nu_{inc} >$ for the central parallelograms under consideration were computed.

On the numerical side, to verify that the values of $\bar{\nu}$ and $\bar{\nu}_{inc}$ calculated from the experiments were not affected by the boundary conditions, we considered infinite periodic structures and investigated the response of representative volume elements (see insets in Fig. 3.4-B) using periodic boundary conditions (see *Supporting Information* for details). The evolution of the macroscopic Poisson's ratio was then obtained from simulation using eqns. B.5 and B.6, in this case with ε_{xx} and ε_{yy} denoting the macroscopic component of the strain.

The evolution of the Poisson's ratio $\bar{\nu}$ and $\bar{\nu}_{inc}$ as function of the local engineering strain $\bar{\varepsilon}_{yy}$ is presented in Fig. 3.4. As expected, all the structures are characterized by initially positive values of $\bar{\nu}$ and $\bar{\nu}_{inc}$. However, as previously observed for a square array of circular holes[117,14], the dramatic pattern transformation introduced by instability strongly affects the Poisson's ratio, leading to enhanced compaction. Beyond the instability, $\bar{\nu}$ is found to monotonically decrease as a function of $\bar{\varepsilon}_{yy}$ in all the four structures and eventually becomes negative. While $\bar{\nu}$ gradually decrease after instability, $\bar{\nu}_{inc}$

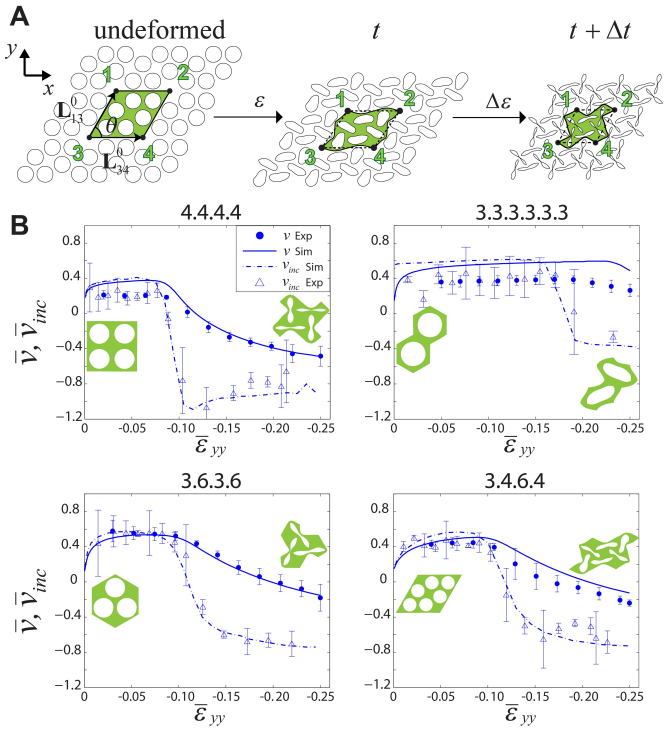

Figure 3.4: (A) Schematic diagram of the central parallelograms used to compute $\bar{\nu}$ and $\bar{\nu}_{inc}$. (B) Macroscopic Poisson's ratio $\bar{\nu}$ and $\bar{\nu}_{inc}$ as a function of the local nominal strain $\bar{\varepsilon}_{yy}$ for all the four periodic porous structures. Finite element simulations are performed on infinite periodic periodic structures. Error-bars on experimental curves are standard deviation of the quantity calculated for multiple parallelograms in the central region(See *Supporting Information*).

is characterized by two plateau. Before instability setting on, all structure are characterized by a constant and positive value of $\bar{\nu}_{inc} \approx 0.4$. At instability, a rapid transition to a negative value that then remains constant for increasing values of deformation is observed. More specifically, we find that after instability $\bar{\nu}_{inc\,4.4.4.4} \approx -0.95$, $\bar{\nu}_{inc\,3.3.3.3.3.3} \approx -0.39$, $\bar{\nu}_{inc\,3.6.3.6} \approx -0.78$ and $\bar{\nu}_{inc\,3.4.6.4} \approx -0.75$. Therefore, our results reveal that instabilities in the four periodic porous structures considered here can be exploited to design materials and devices whose response is characterized by large values of incremental negative Poisson's ratio $\bar{\nu}_{inc}$. The material will exhibit such unusual behavior if pre-loaded beyond the instability point.

The results reported here clearly show that by carefully choosing the initial architecture, materials

with unconventional response can be designed. In fact, our study demonstrate that buckling in four different periodic porous structures may be exploited to achieve large negative values of Poisson's ratio and two of them exhibit chiral patterns under deformation. Furthermore, while in this study we focused on the response of structures with $\psi \simeq 0.5$, the void-volume-fraction ψ can be also used to fine-tune the response of the structures, as revealed by previous studies[14,117]. To confirm the robustness of desired buckling phenomena, detailed FE simulations have been conducted to reveal that for structures with porosity in the range $\psi \in [0.4, 0.6]$ buckling always lead to the compact configurations shown in Fig. 3.2-C (See *Supporting Information*), demonstrating that the proposed folding mechanism can be effectively exploited to design a new class of reconfigurable materials.

3.5 Conclusion

In summary, we have identified four periodic distributions of mono-disperse circular holes in planar elastic structures where mechanical instability can be exploited to reversibly switch between expanded (i.e. with circular holes) and compact (i.e. with elongated, almost closed elliptical holes) configurations. Interestingly, in two of these structures (i.e. 3.6.3.6 and 3.4.6.4) the instability can be exploited to induce the formation of a chiral pattern. Furthermore, in all the structures the pattern transformation induced by instability is found to lead to large negative values of macroscopic Poisson's ratio. Also, due to the intrinsic characteristics of elastic buckling, our study opens avenues for the design of novel responsive and reconfigurable materials and devices over a wide range of length scales. In particular, recent developments in microscale fabrication open exciting opportunities for miniaturization of the proposed structures, with potential applications ranging from tunable mechanical metamaterials to switchable optics.

Finally we note that the design principles outlined in this paper, which combine concepts of topology (i.e. tilings) and mechanics (i.e. buckling), represent a powerful tool to design reconfig-

urable structures and can be further extended to curved surfaces and 3D structures.

This project was a collaboration with Sung H. Kang, Zhenhao Zhao, Lichen Fang under the supervision of Prof. Katia Bertoldi. I was the lead researcher on this project and primary author of the final manuscript. The work in this chapter has already been submitted to Extreme Mechanics Letters.

4

Planar Isotropic Negative Poisson's Ratio Structures

4.1 Introduction

The Poisson's ratio (ν) is the ratio of transverse contraction strain to longitudinal extension strain in the direction of stretching force. Most materials are characterized by a positive Poisson's ratio

($\nu > 0$) and contract in the directions orthogonal to the applied tensile load. However, in the recent years natural materials with negative Poisson's ratio (also called auxetic materials) have been discovered such as cubic metals[7], zeolites[56], ceramics[153] and silica[77]. Moreover, rationally designed geometries and structural mechanisms have also been reported to achieve negative Poisson's ratio. Examples include foams with re-entrant ribs[90,26], chiral microstructures[136,127,139] and rotating units[24,47,163,14,107]. In all these demonstrations, careful design of the microstructure has led to effective negative macroscopic Poisson's ratios ($\nu < 0$), even though the bulk materials have a positive Poisson's ratio. Remarkably, it has been shown that auxetic materials are characterized by enhanced mechanical properties, such as increased shear modulus, indentation resistance and fracture toughness[90,39], and can achieve extremely large strains and shape changes[25].

Most of the proposed auxetic materials are anisotropic[93] and exhibit different properties depending on the loading direction. While the anisotropy can result in larger negative values of Poisson's ratio[18,166], it also limits the application of auxetic materials, as they need to be carefully oriented during operation. In fact, failure to orient the structure may cause the material to exhibit a completely different behaviour from the designed one. Therefore, to enable practical use of auxetic materials in real applications, it is crucial to design and develop isotropic auxetic materials and structures.

Currently, there are few auxetic materials showing isotropic behavior. These include disordered systems such as foams[90], randomly oriented composite laminates[184], granular materials[132] and composites with randomly distributed inclusions[181,68]. Alternatively, to achieve better control and tunability of the Poisson's ratio, ordered auxetic isotropic systems have been numerically designed, such as intricate networks of rods, hinges and springs[3], assemblies of flexible frames and rigid cores[144] and systems of hard cyclic hexamers[179]. Moreover, topology optimization has been used to identify periodic composites with auxetic and isotropic response[92]. Still, it remains a fundamental challenge to design isotropic material systems with controllable auxetic behavior and simple manufacturing process.

4.2 Methods

In this study, we report a new, simple and scalable approach to design and fabricate planar auxetic materials with isotropic behaviour. Our starting points are the following two observations: (*i*) a square array of circular voids on elastic sheets can reversibly transforms into mutually orthogonal elongated elliptical voids under compressive stress and vice versa, exhibiting negative Poisson's ratio behavior[189,147,149]. Periodic arrays of elongated elliptical voids[163] and even elongated cuts[25,47] can exhibit auxetic behaviors without triggering instability; (*ii*) two-dimensional crystalline lattices with six-fold or three-fold rotational symmetry are transversely isotropic[91,112]- i.e. isotropic in their transverse plane. Inspired by these facts, here we investigate the mechanical response of elastic sheets with embedded periodic arrays of elongated cuts and focus on the effect of the degree of rotational symmetry of the pattern. Remarkably, our numerical and experimental results demonstrate that 2D auxetic materials with isotropic response can be easily realized by perforating a sheet with elongated cuts arranged to form a periodic pattern with either six-fold or three-fold symmetry. Moreover, we also show that the auxetic behavior can be easily tuned by varying the length of the cuts and it is retained even under large levels of applied deformation beyond the limit of small strains.

To demonstrate our approach, we start by studying the mechanical response under uniaxial tension of elastomeric thin sheets with a kagome (see Fig. 4.1-b) and square (see Fig. 4.1-c) array of elongated cuts. The square array of cuts has been already shown to result in auxetic response[163], but since the pattern has four-fold symmetry we expect the response of the system to be anisotropic. By contrast, the kagome pattern has six-fold symmetry, so we conjecture its response to be both isotropic and auxetic. To test our hypothesis we characterize the mechanical response of the systems for different orientations of the cut pattern with respect to the loading direction, as shown in Fig. 4.1-b and -c for ϑ ranging between 0 and 45°.

We start by performing numerical simulations using the non-linear Finite Element (FE) code

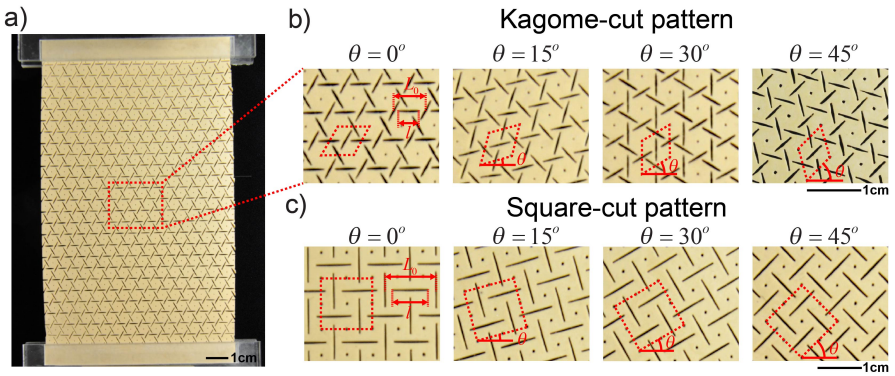

Figure 4.1: 2D auxetic materials are realized by embedding a pattern of elongated cuts into an elastomeric sheet. a) Snapshot of a sample with a kagome cut-pattern. To test whether the mechanical response of the system is isotropic, samples with the cut-pattern oriented at different angles ϑ with respect to the horizontal direction are tested uniaxially. b) Zoom-in views of the central region of samples with a kagome cut-pattern for $\vartheta = 0°, 15°, 30°, 45°$. c) Zoom-in views of the central region of samples with a square cut-pattern for $\vartheta = 0°, 15°, 30°, 45°$. Note that l is the length of cuts, while L_o denotes the upper bound of l. The representative volume elements(RVEs) for both cut-patterns are outlined by red dashed lines.

ABAQUS/Standard. In all our analysis the mechanical response of the elastomeric sheet is captured using an incompressible Neo-Hookean material with initial shear modulus μ_o. Since all considered structures are thin and planar, two dimensional finite-element models are constructed using six-node, quadratic, plane stress elements (ABAQUS element type CPS6M). The cuts are modelled as extremely elongated rhombi (with diagonals whose ratio is chosen to be 0.02) and the accuracy of the FE model is insured by locally refining the mesh around the sharp angles of the cuts. To reduce the computational cost and ensure the response is not affected by boundary effects, we consider two-dimensional, infinite periodic structures using representative volume elements (RVEs – see Fig. 4.2-a and -b) with suitable periodic boundary conditions[12,31]. Each model is loaded uniaxially by applying a macroscopic tensile strain in vertical direction, $\bar{\varepsilon}_{yy}$. The macroscopic Poisson's ratio, $\bar{\nu}$, is then obtained as $\bar{\nu} = -\bar{\varepsilon}_{xx}/\bar{\varepsilon}_{yy}$, where $\bar{\varepsilon}_{xx}$ is the resulting macroscopic strain in horizontal direction. The degree of anisotropy of each model is then examined by rotating the RVE by an angle ϑ, reapplying the tensile strain $\bar{\varepsilon}_{yy}$ in vertical direction and recalculating $\bar{\nu}$. In all our analysis we vary ϑ

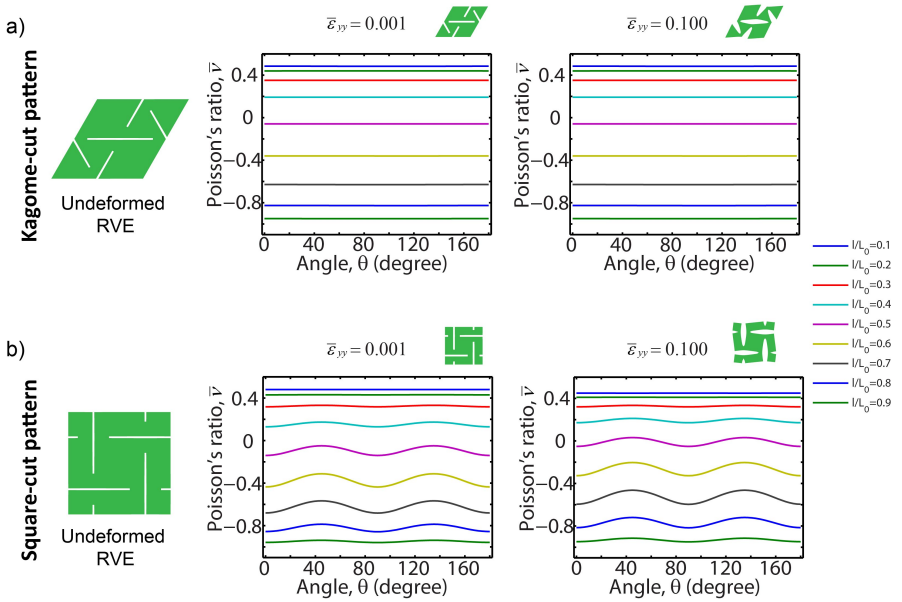

Figure 4.2: Numerical predictions for the in-plane Poisson's ratio, $\bar{\nu}$ as a function of the orientation of the cut pattern with respect to the loading direction. a) Results for the kagome cut-pattern. b) Results for the square-cut pattern. Results for both small ($\bar{\varepsilon}_{yy} = 0.001$) and large ($\bar{\varepsilon}_{yy} = 0.1$) values of applied strain are reported.

through the range $[0^\circ - 180^\circ]$ at intervals of 3°. Finally, we note that the length of the cuts, l, can vary between 0 and L_o, where L_o is the length at which adjacent cuts start touching. In our simulations we vary l/L_o between 0.1 and 0.9.

4.3 Discussion

The numerical results for the square and kagome patterns are shown in Fig. 4.2. For each pattern we report the evolution of the Poisson's ratio, $\bar{\nu}$, as a function of the orientation angle, ϑ, for different values of cut length, l/L_o. First, we note that for both patterns $\bar{\nu}$ monotonously decreases from 0.5 to -1 as l/L_o progressively increases. In particular, we find that $\bar{\nu} \sim 0$ for $l/L_o \sim 0.5$. Therefore, our results indicate that $\bar{\nu}$ can be easily controlled by varying the cut-length. Remarkably, the numerical analysis also reveal that the response of the kagome pattern is isotropic, since $\bar{\nu}$ is not affected

by the orientation of the pattern with respect to the loading. In stark contrast, the mechanical response of the square pattern depends on ϑ and $\bar{\nu}$ is found to be maximum for $\vartheta = 45^\circ$ and 135° and minimum for $\vartheta = 0^\circ$ and 90°. We also find that for the square pattern the extent of anisotropy is affected by l/L_o and is particularly accentuated for $0.4 < l/L_o < 0.7$. Note that this is the range of cut-lengths in which we are particularly interested, since for these intermediate values of l/L_o the cuts can be effectively used to control $\bar{\nu}$. In fact, for $l/L_o < 0.4$ the cuts do not affect significantly the response of the structure, so that its behavior is similar to that of the homogenous elastic sheet with $\bar{\nu} \sim 0.5$. On the other hand, when $l/L_o > 0.7$ the structure approximates a network of rigid polygons connected by rotating hinges, whose Poisson's ratio is known to be -1.0[55]. Our results indicate that as l/L_o approaches 1, even the square tiling behaves in an isotropic way. This is expected since networks of rigid polygons have a single degree of freedom and, therefore, their response is not affected by the direction of loading. However, for such large values of l/L_o the integrity and strength of the structures is severely reduced, limiting their possible applications. Finally, we note from the results for both an infinitesimal strain ($\bar{\varepsilon}_{yy} = 0.001$) and a large strain ($\bar{\varepsilon}_{yy} = 0.1$) (Fig. 4.2) that $\bar{\nu}$ is not affected by the amount of applied deformation, indicating that the structures remain auxetic even when largely deformed.

To verify our numerical analysis, we build physical models of the kagome and square patterns. We start with sheets of natural latex rubber of size $87mm \times 145mm$ and thickness 0.32 mm and use a high speed engraving laser system (*Kern Lasers Systems*) to fabricate the periodic array of cuts. In all our samples the cuts have an approximate width of $\sim 300\mu m$ and L_o (and therefore, the size of the RVE) is chosen so that each specimen comprises more than 10 RVEs to reduce the boundary effects. The cut-length is then determined to achieve $l/L_o = 0.3,\ 0.5$ and 0.7. To quantify the degree of anisotropy of the structures, a series of samples are fabricated with patterns orientated at different angle with respect to the vertical direction (see Figs. 4.1 and 4.3). In particular, by taking advantage of the symmetry of the cut patterns, we fabricate samples characterized by $\vartheta = 0^\circ, 7.5^\circ, 15^\circ, 22.5^\circ,$

30°, 37.5°, 45° and 52.5° for the kagome lattice, while we consider $\vartheta = 0°, 15°, 30°$ and 45° for the square lattice.

Uniaxial tensile tests are performed on a standard quasi-static loading frame (Instron 5566) with a 1 kN load cell (Instron 2525-806) in a displacement-controlled manner. The samples are stretched using two custom-made fixtures to enhance gripping. In all the tests a displacement of 15.0mm in vertical direction is applied (corresponding to a strain $\overline{\varepsilon}_{yy} = 0.1$) at a cross-head velocity of 0.15 mm/min, ensuring quasi-static loading conditions. To monitor the evolution of the deformation, small dots (with diameter$<$ 0.5mm) are engraved to mark the vertices of the RVEs during the cutting step, as shown in Fig.4.1. The position of the markers is recorded using a high-resolution digital camera (Nikon D90 SLR) and then analyzed by digital image processing (Matlab). In particular, we focus on the behavior of nine RVEs in the central part of the samples, where the response is more uniform and not affected by boundary effects. For each RVE, macroscopic values of the engineering strain, $\varepsilon_{xx}^{[i,j]}$ and $\varepsilon_{yy}^{[i,j]}$ were calculated from the positions of the markers. In fact, if we denote with $\mathrm{A}^{[i,j]}$, $\mathrm{B}^{[i,j]}$ and $\mathrm{a}^{[i,j]}$, $\mathrm{b}^{[i,j]}$ the two lattice vectors spanning the RVE in the undeformed and deformed configurations, respectively. It follows that (see Chapter C for details)

$$\begin{pmatrix} \varepsilon_{xx}^{[i,j]} + 1 & \varepsilon_{xy}^{[i,j]} \\ \varepsilon_{yx}^{[i,j]} & \varepsilon_{yy}^{[i,j]+1} \end{pmatrix} = \begin{pmatrix} a_x^{[i,j]} & b_x^{[i,j]} \\ a_x^{[i,j]} & b_y^{[i,j]} \end{pmatrix} \begin{pmatrix} A_x^{[i,j]} & B_y^{[i,j]} \\ A_x^{[i,j]} & B_y^{[i,j]} \end{pmatrix}^{-1} \tag{4.1}$$

where the components of the lattice vectors in x- and y- directions can be easily calculated from the positions of the markers. For each RVE macroscopic values of the Poisson's ratio are then obtained as

$$\nu^{[i,j]} = -\frac{\varepsilon_{xx}^{[i,j]}}{\varepsilon_{yy}^{[i,j]}}, \tag{4.2}$$

and finally the ensemble average, $\bar{\nu} =< \nu^{[i,j]} >$ of the nine central RVEs under consideration is

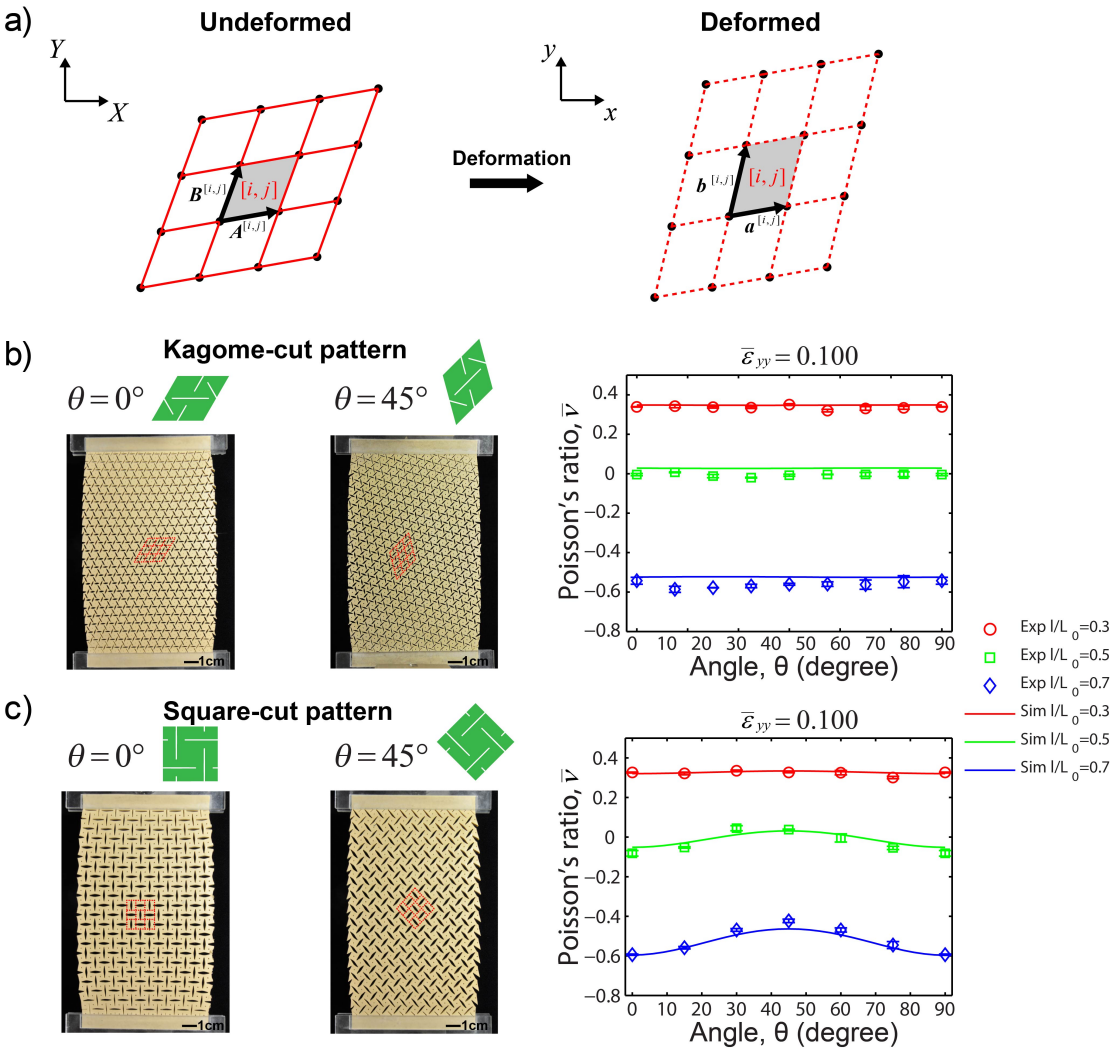

Figure 4.3: Comparison between experimental and numerical results. a) Schematic diagram of the central region with 9 RVEs, which are used to calculate $\bar{\nu}$. $\mathrm{A}^{[i,j]}$ and $\mathrm{B}^{[i,j]}$ are the lattice vectors spanning the RVE in undeformed state, while $\mathrm{a}^{[i,j]}$, $\mathrm{b}^{[i,j]}$ are the lattice vectors in the deformed state. b) Comparison between experimental (markers) and numerical results (continuous lines) for the kagome cut- pattern. c) Comparison between experimental (markers) and numerical results (continuous lines) for the square cut-pattern. Snapshots of the samples with $\vartheta = 0^\circ$ and 45° at a tensile strain of $\bar{\varepsilon}_{yy} = 0.1$ are shown on the left.

computed.

In Fig. 4.3 we report the experimentally measured Poisson's ratio, $\bar{\nu}$, as a function of the orientation of the pattern for the kagome and square array of cuts. The experimental results (markers) are compared to the numerical predictions (continuous lines), showing excellent agreement and confirming the validity of our numerical analysis. Again, we note that the kagome-cut pattern exhibit nearly identical Poisson's ratio in all loading directions, regardless of the cut-length. By contrast, the square cut-pattern exhibits an orientation- dependent Poisson's ratio, except for short cuts ($l/L_o = 0.3$) when the response of the material is similar to that of the homogeneous elastic sheet.

Having demonstrated our method for kagome and square patterns (with 6-fold and 4-fold rotational syssmetry, respectively), we now show that the approach can be generalized to arbitrary cut-patterns. In particular, in Fig. 4.4 we report experimental and numerical results for a rhombitrihexagonal-cut pattern, a Y-cut pattern and a Z-cut pattern. Again, we observe the excellent agreement between all numerical (markers) and experimental (continuous lines) results. As expected, since the rhombitrihexagonal cut-pattern and Y-cut pattern have six-fold and three-fold rotational symmetry, for these structures the response is found to be isotropic for all values of l/L_o and even at large strain levels. Differently, the Z-cut pattern exhibits strong anisotropy and its Poisson's ratio for $l/L_o = 0.7$ varies from -0.57 to -0.90 when the loading direction changes. This behaviour is expected since the Z-pattern has two-fold rotational symmetry. Finally, all our results demonstrate that the cut-length can be effectively used to tune the Poisson's ratio of the system. Simply by increasing $l/L_o = 0.3$ to $l/L_o = 0.7$, the $\bar{\nu}$ is significantly reduced from ≈ 0.3 to ≈ -0.6, giving us the opportunity to easily realize auxetic systems. Therefore, our results confirm the robustness of our approach. By patterning elastic sheets with arrays of cuts, we can not only achieve negative Poisson's ratio, but also isotropic behavior by carefully choosing the degree of rotational symmetry of the pattern.

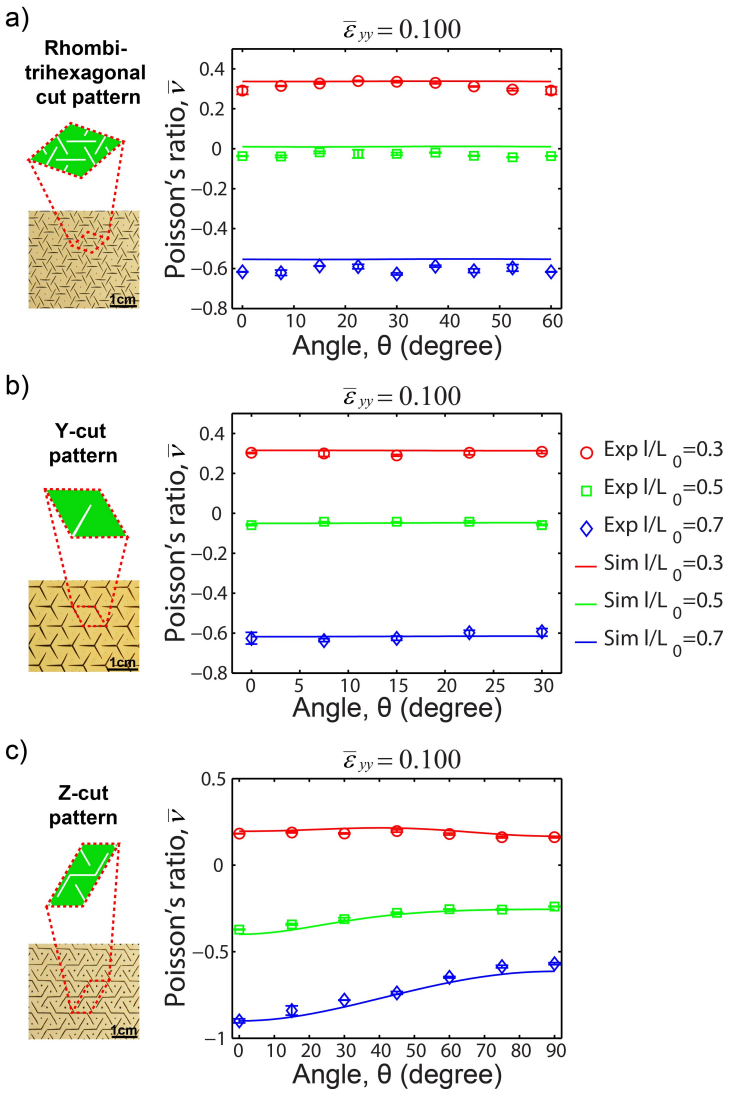

Figure 4.4: Comparison between experimental and numerical results. a) Comparison between experimental (markers) and numerical results (continuous lines) for the rhombitrihexagonal cut-pattern. b) Comparison between experimental (markers) and numerical results (continuous lines) for the Y-cut pattern. b) Comparison between experimental (markers) and numerical results (continuous lines) for the Z-cut pattern.

4.4 Summary

In summary, our findings demonstrate a fundamentally new way of generating isotropic 2D materials with negative Poisson's ratio by embedding periodic arrays of cuts in elastomeric sheets. Interestingly, we showed that Poisson's ratio of the system can be easily tuned and drastically altered by varying the length of the cuts, while the isotropy of the system is controlled by the degree of rotational symmetry of the cut-patterns. Combining numerical analysis and experiments, we investigated the response of five different cut-patterns and found that patterns with three- and six-fold symmetry result in an isotropic response, while arrays of cuts with two- and four-fold symmetry lead to anisotropic responses. Remarkably, the systems we have explored can be easily fabricated and have a robust behavior. We believe that the insights gained in this study can serve as an important guideline for designing isotropic auxetic materials and structures and provide a simple, practical fabrication approach for applications.

This project was a collaboration with Pai Wang, Cangyu Qu, Samuel Shian, Elizabeth R. Chen under the supervision of Prof. Katia Bertoldi. I was the lead researcher on this project and primary author of the final manuscript. Pai simulated the phononic response, and helped on the wave propagation measurement. Elizabeth formulated the classification of the folding mechanisms. The work in this chapter has already been published and the relevant citation is: Shan, S., Kang, S. H., Wang, P., Qu, C., Shian, S., Chen, E. R., Bertoldi, K. (2014). Harnessing Multiple Folding Mechanisms in Soft Periodic Structures for Tunable Control of Elastic Waves. Advanced Functional Materials, 24(31), 4935-4942.

5

Harnessing multiple folding mechanisms in soft periodic structures for tunable control of elastic waves

5.1 Introduction

Porous materials with well-defined periodicity are ubiquitous not only in nature, but also in synthetic structures and devices.[50] Periodic porous materials offer novel and unique properties, including light weight,[137] high energy absorption,[94] and the ability to control the propagation of both electromagnetic[138] and elastic waves[88,103] and heat flow.[102] The properties and functionality of such materials are generally determined by the deformation mechanisms of the ligaments, which buckle under compression at relatively low values of strain.

In elasto-plastic porous materials buckling of the beam-like ligaments results in collapse bands that progress at relatively constant stress, providing an efficient energy absorbing mechanism.[177,120,121,180,62] However, this deformation process cannot be exploited to dynamically tune the macroscopic response of the system, since it is irreversible. By contrast, in periodic porous elastic structures, buckling of the ligaments may trigger dramatic homogeneous and reversible pattern transformations.[110,189] Remarkably, it has been demonstrated that this parallel, cooperative buckling - a kind of 'phase transition' from one to another microstructure - can be instrumental to design materials with tunable properties, including systems with tunable negative Poisson's ratio,[13] phononic[10,71,175] and

photonic[87] switches and color displays.[97]

Most of the porous systems studied so far are dual-shaped, since mechanical instability is found to trigger only one distinct new buckled pattern. Although different buckling modes have been observed in hexagonal honeycombs under biaxial compression depending on the loading conditions,[51,50,120,121,27,116] the multiple pattern transformations induced by buckling have never been exploited to reversibly tune the properties of the system.

Here, we show that the ability to induce the formation of multiple ordered patterns in periodic porous elastic structures opens avenues for creating highly tunable systems. First, we develop a robust framework to identify periodic distributions of circular holes for which buckling and the direction of the applied loading can be exploited to form multiple folding patterns. Then, we confirm our findings through a combination of numerical simulations and experiments. Finally, we demonstrate numerically and experimentally that structures with multiple folding mechanisms open avenues for the design of highly tunable phononic crystals, whose response is effectively controlled by both the direction of loading and the magnitude of the applied deformation.

5.2 Design of soft periodic structures with multiple folding mechanisms

5.2.1 Periodic networks of rigid polygons

To identify periodic porous elastic structures with multiple folding mechanisms, we start by investigating the flexibility of periodic planar networks built from rigid corner-connected polygons, which can rotate freely. While a network of connected squares has a single folding mechanism (see Chapter E), it has been recently shown that in planar networks built from equilateral triangles the number of folding mechanisms grows with the size of unit cell.[76] Here, we focus on the simplest of such tilings made of triangles - the kagome lattice. In this rigid network the triangles are corner-connected to form hexagonal holes in the undeformed configuration and the smallest unit cell consists of only two

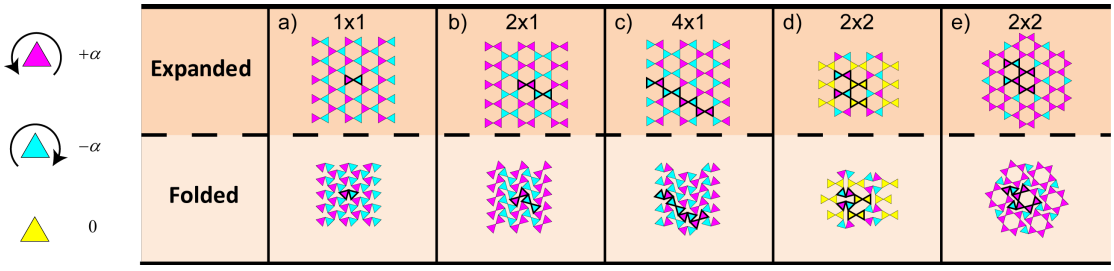

Figure 5.1: Schematic of the basic folding mechanisms in a rigid kagome network. The basic unit cell for each folding mechanism is outlined in black. The color of the triangles corresponds to their rotation. a) Mode with a basic cell of size 1×1 ; b) Mode with a basic cell of size 2×1 ; c) Mode with a basic cell of size 4×1; d) Mode with a basic cell of size 2×2; e) Mode with a basic cell of size 2×2.

triangles (see Fig. 5.1-top).

If we consider a single unit cell (i.e. two corner-connected triangles) as a building block, it is easy to see that the periodic network has only one folding mechanism, in which all hexagonal holes progressively reduce to 3 point star-like shapes (see Fig. 5.1-a and Chapter E). However, if we focus on a representative volume element (RVE) comprising an array of 1×2 unit cells (i.e. four corner-connected triangles) another folding mechanism emerges, resulting in a pattern of sheared voids where the shear direction alternates back and forth from row to row (see Fig. 5.1-b and Chapter E). Finally, for a RVE consisting of 8 triangles, three other mechanisms are found: one consisting of alternating rows of sheared and 3 point star-like voids (see Fig. 5.1-c); another characterized by alternating rows of elongated holes oriented in horizontal and vertical direction and at $\pm 30^\circ$ with respect to the vertical direction (see Fig. 5.1-d); and a chiral pattern comprising six highly deformed voids surrounding an undeformed one (see Fig. 5.1-e).

Additional folding mechanisms can then be identified by considering larger RVEs (see Chapter E). However, all these mechanisms share the same basic elements found in the patterns shown in Fig. 5.1. We also note that in all the identified folding mechanisms the triangles are found either to rotate by $\pm\alpha$ (i.e. by the same amount either in clockwise or anti-clockwise direction, see magenta and cyan triangles in Fig. 5.1) or not to rotate at all (i.e. $\alpha = 0$, see yellow triangles in Fig. 5.1),

facilitating the construction of folding mechanisms for large RVEs.

Finally, given the finite size of the elastomeric samples considered in this study, it is worth pointing out that we expect only the basic folding mechanisms shown in Fig. 5.1 to be triggered during loading.

5.2.2 From networks of rigid polygons to continuum porous structures

Having found a planar network built from rigid corner-connected triangles with multiple folding mechanisms, we then identify the corresponding porous structure. This can be easily done by replacing all the hexagonal voids with circular ones,[142] as shown in Fig. 5.2. It is interesting to see that the outcome of this simple process is a porous structure comprising a periodic array of circular holes on a triangular lattice. In this continuum structure all the hinges of the original kagome network are replaced by thin ligaments and we expect these ligaments to buckle during loading.

Although the stability under biaxial compression of similar structures such as hexagonal honeycombs has been previously studied,[51,50,120,121,27,116] the ability to induce multiple pattern transformations has never been exploited to design materials and devices with enhanced tunability. In the next sections we investigate both numerically and experimentally how loading paths with different angles can be exploited to trigger the different folding mechanisms shown in Fig. 5.1, enabling the design of materials with highly tunable responses.

5.3 Mechanics of soft periodic structures with multiple folding mechanisms

5.3.1 Numerical analysis

We continue by performing finite element (FE) simulations to investigate the patterns induced by buckling in a triangular array of circular holes in an elastomeric matrix. We focus on a structure char-

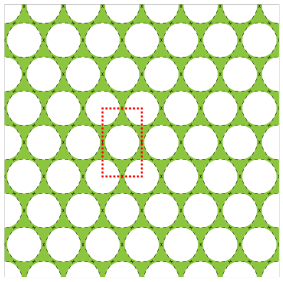

Figure 5.2: From a rigid networks of triangles to its corresponding continuum structure. All the hinges of the original kagome network (dashed black line) are replaced by thin ligaments in the continuum structure (shaded in green). The dotted red line indicates the unit cell of the structure.

acterized by an initial porosity $\psi_o = 70\%$ and assume plane strain conditions. The nonlinear finite-element code ABAQUS/STANDARD is used to deform the structures as well as to investigate its stability. For all the analyses, 2D finite element models are constructed using triangular quadratic elements (element type CPE6H in ABAQUS) and the accuracy of the mesh is ascertained through a mesh refinement study. Moreover, the response of the silicone rubber used in the experiments to cast the samples is captured using the incompressible Neo-Hookean hyperelastic model[115] with initial shear modulus μ_o.

Since the finite-sized specimens are necessarily influenced by boundary conditions at the edges, we focus on the response of the corresponding infinite periodic structure and study the response of rectangular RVEs by applying periodic boundary conditions.[31,112] We investigate the response of the porous structure under biaxial loading so that the macroscopic deformation gradient $\overline{F}$ is given by

$$\overline{F} = (1 + \varepsilon_{xx})e_x \otimes e_x + (1 + \varepsilon_{yy})e_y \otimes e_y + e_z \otimes e_z, \tag{5.1}$$

where ε_{xx} and ε_{yy} denote the macroscopically applied nominal strains and e_x, e_y and e_z are the basis vectors of Cartesian coordinates.

Without loss of generality, we focus our attention to proportional straining paths in principal nominal strain space. More specifically, we assume that the ratio of the principal nominal strains is fixed, namely:

$$\varepsilon_{xx} = \lambda \cos \vartheta, \qquad \varepsilon_{yy} = \lambda \sin \vartheta, \tag{5.2}$$

where λ is the monotonically increasing load parameter and ϑ is the load path angle. In this study we consider $\pi < \vartheta < 3\pi/2$ to investigate various biaxial compression loading conditions. To facilitate the comparison between deformed configurations obtained for different values of ϑ, we also introduce the areal strain ε_{Area} defined as[111]

$$\begin{aligned} \varepsilon_{Area} = \quad & \frac{A - A_0}{A_0} = (1 + \varepsilon_{xx})(1 + \varepsilon_{yy}) - 1 = \\ & \lambda(\cos \vartheta + \sin \vartheta) + \lambda^2 \cos \vartheta \sin \vartheta, \end{aligned} \tag{5.3}$$

A_0 and A denoting the area of the RVE in the undeformed and deformed configuration, respectively.

To understand the patterns emerging as the result of buckling in the structure, we start by investigating the stability of the system. Taking the rectangular domain highlighted by red box in Fig. 5.2 as unit cell, we consider RVEs consisting of $m \times n$ cells subjected to periodic boundary conditions. For a given value of ϑ we progressively load each RVE and calculate its natural frequency along the loading path, accounting for the effect of large deformation induced by loading. As an example, in Fig. 5.3-a we show the results of the stability analysis for an RVE comprising 2×2 unit cells and loading path angle $\vartheta = \pi$. In the undeformed configuration (i.e. $\lambda = 0$) all eigenvalues ω^2 are positive. However, as λ increases, the eigenvalues associated with each mode gradually decrease and eventually become negative. The critical loading parameter λ_{cr} associated with each mode can be easily extracted from the data, since it corresponds to the intersection point between each curve and the horizontal line $\omega^2 = 0$. For this specific case, we find that the lowest critical loading parame-

ter $\lambda_{cr,1} = 0.0331$ is associated with a mode that resembles the folding mechanism shown in Fig. 5.1-d for the kagome network. Here and in the following we refer to this mode as to the X-mode. The second mode is then triggered at $\lambda_{cr,2} = 0.0357$, resulting in a pattern similar to that reported in Fig. 5.1-b, which we denote as Z-mode. Subsequently, the third and fourth modes are found at $\lambda_{cr,3} = \lambda_{cr,4} = 0.0476$ consisting of alternating rows of sheared and 3 point star-like voids as that shown in Fig. 5.1-c. Finally the fifth mode is triggered at $\lambda_{cr,5} = 0.0665$, comprising an array of 3 point star-like voids as that reported in Fig. 5.1-a.

Identical calculations are then repeated for RVEs of different sizes and the critical strain of the infinite periodic structure for the given load path angle ϑ is then defined as the minimum of λ_{cr} on all possible periodic RVEs. In Fig. 5.3-b we report the critical strains for periodic RVEs with $m \times n$ cells for $\vartheta = \pi$. The results indicate that the critical loading parameter is minimum for RVEs comprising an even number of unit cells in both directions and it is associated with the X-mode. Higher λ_{cr} is found for RVEs with an odd number of unit cells either in vertical or horizontal direction, for which the Z-mode is found to be critical. Therefore, when the structure is compressed with loading path angle $\vartheta = \pi$, we expect the X-mode to be triggered during loading.

Finally, to construct the instability surface we repeat the same calculations for different loading path angles ϑ. We first note that for all considered values of ϑ, the X- and Z-mode are always triggered either as first or second mode. In Fig. 5.3-c we then plot the critical load parameter associated with the X- and Z-mode as a function of ϑ. The critical load parameter λ_{cr} associated with the X-mode is found to decrease at first, to reach a minimum at $\vartheta = (5/4 - 1/36)\pi$ and then to progressively increase. Similar behavior is found for the critical loading parameter associated to the Z-mode, but in this case the minimum occurs at $\vartheta = (5/4 + 1/36)\pi$. Interestingly, for $\vartheta < 5\pi/4$ the critical loading parameter λ_{cr} associated to the X-mode is always lower than that corresponding to the Z-mode, so that the X-mode is expected to emerge during deformation for this range of loading path angles. By contrast, the Z-mode is expected to be triggered when $5\pi/4 < \vartheta < 3\pi/2$, since

in this case the lowest critical loading parameter is that corresponding to the Z-mode. Finally, it is worth noting that both the X- and Z-mode are characterized by the same critical loading parameter for $\vartheta = 5\pi/4$, suggesting that for this specific loading direction a pattern corresponding to a linear combination of both modes may be triggered.

Next, guided by the stability analysis we conduct a post-buckling analysis on a RVE consisting of 2×2 unit cells by applying periodic boundary conditions and introducing a geometrical imperfection with the form of the first two eigenmodes. In Fig. 5.4-a, -c and -e we report numerical predictions of the pattern evolution for $\vartheta = \pi, 5\pi/4$ and $3\pi/2$ at different values of areal strain ε_{Area}. Initially, the circular holes deform gradually and homogeneously. However, a transformation to a strikingly different pattern is triggered very early along the loading path (see images at $\varepsilon_{Area} = -0.05$) and the new patterns become further accentuated in shape with increasing strain as seen in the images at ε_{Area} = -0.10, -0.15, -0.20 and -0.25. As predicted by the stability analysis, the structure deforms into the X- and Z-mode when $\vartheta = \pi$ and $3\pi/2$, respectively. However, a new chiral pattern resembling that reported in Fig. 5.1-e for the kagome network emerges when the structure is compressed equibiaxially (i.e. $\vartheta = 5\pi/4$). Interestingly, this chiral pattern does not correspond to one of the modes predicted by the stability analysis, but it can be obtained as a linear combination of the X- and Z-mode (see Chapter E).

5.3.2 Experiments

To verify our numerical analysis, we fabricate centimeter scale elastomeric structures comprising 10 × 12 unit cells and characterized by initial porosity $\psi_o = 70\%$, hole diameter D_o =8 mm and out-of-plane thickness ∼50 mm. The samples for the experiments are fabricated using silicone rubber (Mold Max 60 from Smooth-On Inc, Young's modulus $E = 2.16$ MPa) and a mold-casting process with molds prepared by 3D rapid prototyping. In-plane biaxial compression tests are performed using a custom-built testing set-up with four linear stages (see Chapter E).

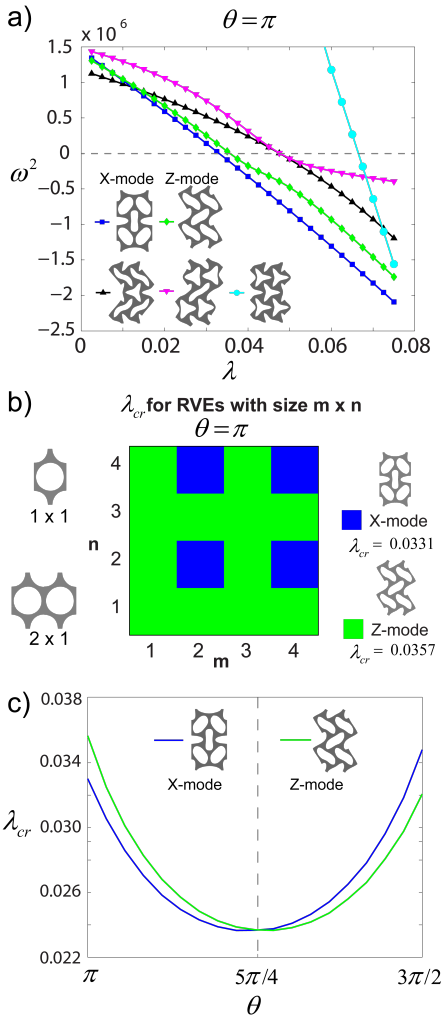

Figure 5.3: Numerical study of the instability of a periodic structure with multiple folding mechanisms. a) Evolution of eigenvalues at different levels of compression (loading along $\vartheta = \pi$ path) and corresponding deformation modes. The intersection points of each curve with the horizontal line $\omega^2 = 0$ corresponds to the critical loading parameter λ_{cr} for each mode. b) Critical loading parameter λ_{cr} for RVEs consisting of $m \times n$ unit cells (loading along $\vartheta = \pi$ path), where a unit cell consists of a rectangular domain with two voids. The results indicate that configurations with even number of unit cells along the two directions have the minimum critical strain. c) Critical loading parameter λ_{cr} associated to the X-mode (blue line) and Z-mode (green line) as a function of the loading path angle ϑ.

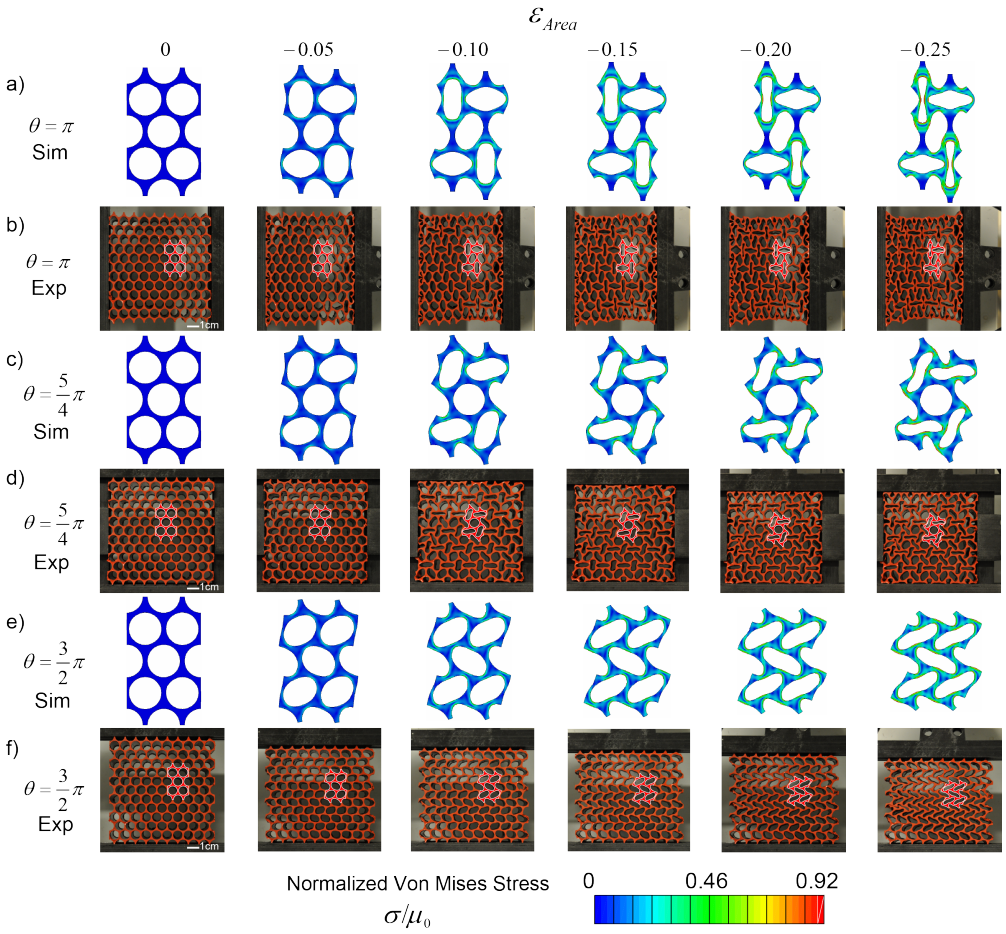

Figure 5.4: Numerical and experimental images of the triangular lattice loaded along $\vartheta = \pi$ (a and b), $\vartheta = 5\pi/4$ (c and d), $\vartheta = 3\pi/2$ (e and f) at different levels of deformation. The results show three distinct folding mechanisms: X-mode under horizontal compression (i.e. $\vartheta = \pi$), Z-mode under vertical compression (i.e. $\vartheta = 3\pi/2$) and a chiral mode under equibiaxial compression (i.e. $\vartheta = 5\pi/4$). The deformed shapes from simulation (colored in bright-red and outlined in white) are superimposed on the experimental pictures showing excellent agreement. For the numerical images, we also show the normalized Von Mises stress distributions in the deformed configurations.

Representative pictures taken during the tests at different levels of ε_{Area} are presented in Fig. 5.4-b, -d and -f for $\vartheta = \pi, 5\pi/4$ and $3\pi/2$, respectively. We start by noting that there is excellent agreement between numerical (Fig.5.4-a, -c and -e) and experimental (Fig. 5.4-b, -d and -f) results. In particular, the effect of the boundary conditions is found to be negligible and the pattern transformations induced by instability are remarkably uniform across the samples, so that the behavior of the finite size sample does not deviate from that of the infinite periodic structure investigated numerically. Note that for the tests performed with $\vartheta = \pi$ and $\vartheta = 3\pi/2$, we do not constrain the deformation in lateral direction, since we find the lateral strain to be negligible (more specifically, we find the absolute value of lateral strain to be less than 0.05). Finally, since the specimens are made of an elastomeric material, the process is fully reversible and repeatable. Upon release of the applied loading condition, the deformed samples recover their original configurations, suggesting that this deformation mechanisms can be exploited for the design of materials with tunable properties.

5.4 Harnessing multiple folding mechanisms to design tunable phononic crystals

Having demonstrated that multiple folding mechanism can be easily triggered in a triangular array of circular voids by simply changing the loading path angle ϑ, in this section we show that the system can be exploited to design highly tunable phononic crystals for the control and manipulation of elastic wave propagation.

Phononic crystals are periodic structures in which Bragg scattering is exploited to effectively filter elastic waves by the generation of bandgaps - frequency ranges of strong wave attenuation - at wavelengths comparable to the unit cell size.[88] Motivated by technological applications such as the design of waveguides,[80,74,81,156,157,158,171] frequency modulators,[74] noise-reduction devices,[36,35,20] and vibration isolators,[33,19] the effects of both material properties,[17,170,190] and geometry (i.e., volume fraction

and topology)[98,109] on the characteristics of phononic crystals have been investigated. Moreover, it has been recently recognized that large deformations induced by instabilities can be exploited to design phononic crystals whose bandgap position and width can be reversibly tuned.[10,71,175] Here, we show both numerically and experimentally that the tunability of the periodic system can be greatly enhanced in the presence of multiple folding mechanisms.

5.4.1 Numerical analysis

To investigate the effect of different instability-induced patterns on the propagation of small amplitude elastic waves in the periodic structure, we first conduct finite element analysis (see Chapter E). We start by constructing the dispersion diagram for the undeformed configuration, as shown in Fig. 5.5-a. When undeformed, the periodic structure possesses a complete band gap (i.e. bandgap for all directions of wave propagation) for $\tilde{f} = \omega a/(2\pi c_T) = 1.189 - 1.238$, where ω is the angular frequency of the propagating wave, the lattice constant $a = 10$ mm is defined as the center-to-center distance between holes in the undeformed configuration and $c_T = 18.3$ m/s is the transverse speed of sound in the constituting homogeneous elastomeric material. Therefore, elastic waves with frequency $f = \omega/(2\pi)$ in the range $2176 - 2266$ Hz are not allowed to propagate within the undeformed structure due to the band gap.

Next, we investigate the effect of the applied load on the propagation of elastic waves, by considering three deformed configurations obtained by different loading path angles $\vartheta = \pi, 5\pi/4$ and $3\pi/2$, but under the same areal strain, $\varepsilon_{Area} = -0.24$. As shown in Fig. 5.4, these three different values of ϑ result in three distinct patterns. Interestingly, the dispersion diagrams shown in Fig. 5.5-b, -c and -d indicate that the variation in patterns has a strong effect on the propagation of elastic waves, demonstrating that in periodic elastic structures with multiple folding mechanisms the band gaps can be dramatically altered not only by the extent of deformation but also by the choice of the loading path.

In fact, when the X-mode is triggered (i.e. $\vartheta = \pi$), the pre-existing complete band gap is shifted and widened to $\tilde{f} = 1.180 - 1.307$. In addition, two new complete band gaps that do not exist in the undeformed structure appear at $\tilde{f} = 0.699 - 0.765$ and $\tilde{f} = 1.045 - 1.070$. Differently, for $\vartheta = 5\pi/4$ the chiral folding mechanism is triggered and in this case the system is characterized by five complete band gaps for $\tilde{f} = 0.724 - 0.745, 0.795 - 0.884, 1.199 - 1.278, 1.351 - 1.386$, and $1.461 - 1.509$. Finally, the Z-mode is triggered for $\vartheta = 3\pi/2$ and in this case the deformation is found to widen the pre-existing complete band gap and to open only one complete new band gap for $\tilde{f} = 1.207 - 1.277$.

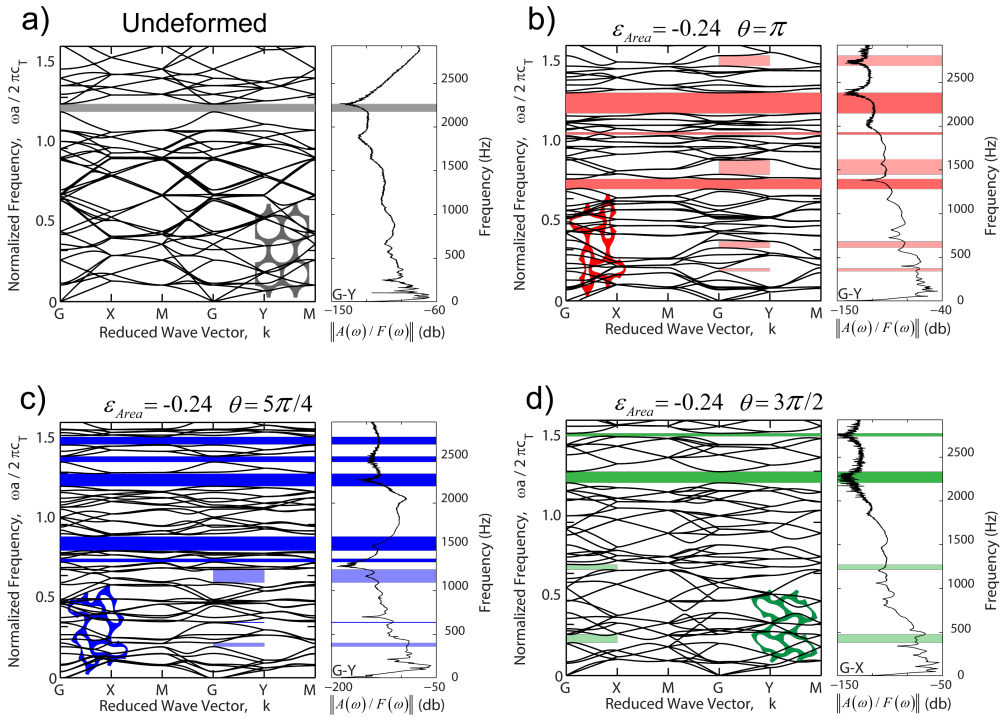

Figure 5.5: Comparison between the numerical dispersion relations (left) and the experimental frequency response functions (right) of the system obtained for different values of ϑ.

5.4.2 Experiments

To validate the predictions of the numerical simulations, frequency response measurements of the elastomeric structure are made using an electrodynamic shaker directly connected to one end of samples through a load cell to provide vibrations. The dynamic response is recorded using a miniature accelerometer attached to the far end of the sample (see Chapter E). Measurements are conducted at different level of deformation and the transmittance is computed as the ratio between the output acceleration signal recorded at the far end of the sample and the input force signal from the load cell (i.e., $\|A(\omega)/F(\omega)\|$).

Fig. 5.5 shows the comparison between numerical and experimental results. For each of the four panels in Fig. 5.5, the dispersion plots on the left are calculated numerically and plots on the right show the transmittance curves from experiments. Here, the numerical calculations consider all propagation directions in an infinitely periodic structure, while the experimental results are shown for only one propagation direction (G-Y direction for Fig.5.5-a, -b and -c; G-X direction for Fig.5.5-d). Nevertheless, we still observe a good match between these two sets of results. In the undeformed case, the experimental response indicates an apparent attenuation at the numerically calculated band gap frequency. After the structure is deformed into different patterns, the calculated complete band gaps can still find their signatures in the experimental results, with very few exceptions due to finite-size boundary effects that are not investigated in this study. Furthermore, the transmittance curves from experiments also exhibit some features of directional band gaps, indicated by the lighter color-shaded areas in Fig.5.5.

5.5 Conclusions

We demonstrated both numerically and experimentally the design of highly tunable phononic crystals by harnessing multiple folding mechanisms in periodic elastomeric structures comprising a tri-

angular array of circular holes. We started with a geometrical analysis of 2D rigid periodic networks and found that a kagome lattice can have multiple folding mechanisms. Guided by these results, we rationally designed the corresponding continuum soft periodic porous structure and showed that three different patterns induced by buckling can be triggered during compressive loading by changing the direction of loading. Remarkably, the dynamic response of the system was found to be highly affected by the pattern induced by buckling, demonstrating that the band gaps can be tuned both by deformation mode and the extent of deformation.

Our finding opens new opportunities to design multi-functional devices with enhanced tunability because (i) the mechanism can be applied to various length-scales; (ii) the various patterns can be triggered upon application of different stimuli and using different materials; (iii) the process is fully reversible and (iv) more importantly, the formation of different patterns can be easily controlled by changing the loading direction. By engineering geometry, length scales, and materials, we can envision smart systems that control the wave propagation autonomously depending on the loading conditions.

This project was a collaboration with Sung H. Kang, Wim L. Noorduin, Mughees Khan, Lichen Fang and Francisco Candido under the supervision of Prof. Joanna Aizenberg and Prof. Katia Bertoldi. I was one of the lead researcher on this project and equal contribution author. Sung and I did experiments and analysis together. I derived equations, worked on simulations and assisted in preparation of the manuscript. The work in this chapter has already been publshed and the relevant citation is: Kang, S. H.†, Shan, S.†, Noorduin, W. L.†, Khan, M., Aizenberg, J., & Bertoldi, K. (2013). Buckling-Induced Reversible Symmetry Breaking and Amplification of Chirality Using Supported Cellular Structures. Advanced Materials, 25(24), 3380-3385. .

6

Buckling-Induced Reversible Symmetry Breaking and Amplification of Chirality Using Supported Cellular Structures

6.1 Introduction

Robust routes to induce chirality in centrosymmetric systems are not only of fundamental interest in unraveling the origin of single chirality as found in nature, but also have a broad range of practical applications including optical devices[188,173,154], sensors[63], pharmaceuticals[73], and advanced structural components[15]. Since many chiral systems show distinctive proper-ties depending on their handed-ness[63,54,16], elucidating routes to induce chiral symmetry breaking and to control the handed-ness across different length scales is crucial. In general, the emergence of chiral structures of single handedness relies on a two-step process: (i) spontaneous symmetry breaking, followed by (ii) full amplification of this chiral imbalance to yield a uniform configuration. On the molecular scale, experimental demonstrations of such processes have been reported only for few crystallizing systems and chemical reactions[151,85,172,113], in which the amplification relies on activating and inhibiting interactions at the molecular scale[45]. Extending these principles to larger length scales requires fundamentally different concepts. Although centrosymmetric nanopost arrays[126,75,57] and swellable confined nanoscale gel films[148,149] were recently reported to form chiral structures in the absence of chiral induction, no study has been reported on the spontaneous and reversible chiral symmetry breaking

and subsequent full amplification to yield large areas of ordered structures with single handedness.

Guided by a theoretical model, we here exploit buckling in rationally designed supported cellular structures at the mesoscale to reversibly switch between the initially achiral configuration and subsequent uniform left- or right- handed configurations. Moreover, we demonstrate that the underlying principles can be generalized using different geometries, materials, stimuli, and length scales. Although buckling is often regarded as a failure mode that needs to be avoided in structural mate-rials, there are numerous natural[44,143], and artificial[21,189,71,149,130,83,14,141] systems that use it to their advantage. Buckling of surface-attached strips[167] and free-standing structures[50] has been studied extensively, but little has been known about mechanical instabilities in surface-attached cellular structures. Moreover, while the deformation and unique mechanical properties of chiral cellular structures have been the focus of many studies[127,155], here we demonstrate spontaneous and reversible chiral symmetry breaking in initially achiral structures followed by full amplification of the chiral imbalance across the entire structure to yield configurations of single handedness.

6.2 Methods

We start by recognizing that the formation of a chiral pattern, in which all vertices rotate in the same direction, requires that all the individual plates buckle in a higher mode comprising an integer number of complete sinusoids, as shown at the bottom of Figure 1a for a honeycomb as a model cellular structure. It is not sufficient to simply buckling a free-standing honeycomb structure to form a chiral structure, since this induces a first-order mode in all plates[50,6], leading to an achiral configuration where adjacent vertices alternately rotate clockwise and counterclockwise, as shown at the top of Figure 6.1. However, the attachment of the cellular structure to a rigid substrate allows higher order buckling modes, so that one can design architectures capable of deforming into either achiral or chiral configurations. Based on plate theory, we anticipate that the buckling mode can be controlled

by carefully designing the dimensions of the cellular architecture. Furthermore, we expect that the connectivity of these cellular structures contributes to the uniform spreading of the chiral pattern once the symmetry is locally broken.

6.2.1 Analytical derivation

To define the design criteria and predict the deformation of the ensemble, we conducted elastic buckling analysis of an individual supported thin plate. Assuming that the thin plate of length l, height h, and thickness tmay be described as a linear elastic material with Young's modulus E, Poisson's ratio ν, and bending stiffness $D = Et^3/[12(1-\nu^2)]$, its buckling behavior is described by[165],

$$\frac{\partial^4 w}{\partial x^4} + 2\frac{\partial^4 w}{\partial x^2 \partial y^2} + \frac{\partial^4 w}{\partial y^4} + \frac{Et\varepsilon_{sw}}{D}\frac{\partial^2 w}{\partial x^2} = 0, \tag{6.1}$$

where w is the deflection in the out-of-plane direction and ε_{sw} denotes the differential swelling strain which is assumed to be uniform within the plate. To consider the effect of the neighboring plates in the lattice structures, we assume the two vertical edges at $x = 0$ and $x = l$ to be supported (i.e. $w = 0$ and $\frac{\partial^2 w}{\partial x^2} + \nu\frac{\partial^2 w}{\partial y^2} = 0$), so that the solution of Eq. 6.1 has the form $w = f(y)\sin\frac{m}{l}x$, m being an integer (see Chapter D). For a plate attached to a rigid substrate (i.e. free at $y = h$ and clamped at $y = 0$), the critical swelling strain ε_{sw}^{cr} and the wavelength $2l/m$ of the corresponding mode can then be solved as a function of the aspect ratio l/h, as shown in Figure 6.1(b). This stability diagram unambiguously reveals that in an initially straight plate with $0 < l/h < 2.321$ a buckling pattern with half sinusoidal wavelength (i.e. $m = 1$) will emerge upon reaching a critical swelling strain, resulting in an achiral pattern (space group: P31m). Differently, if $2.321 < l/h < 4.015$ the buckling will be a full sinusoid (i.e. $m = 2$), yielding a chiral pattern (space group: P6). To fully define the geometry of supported cellular structure for experiments, we investigated the effect of the thickness of the plates using non-linear finite element analyses (see Chapter D for details and Supple-

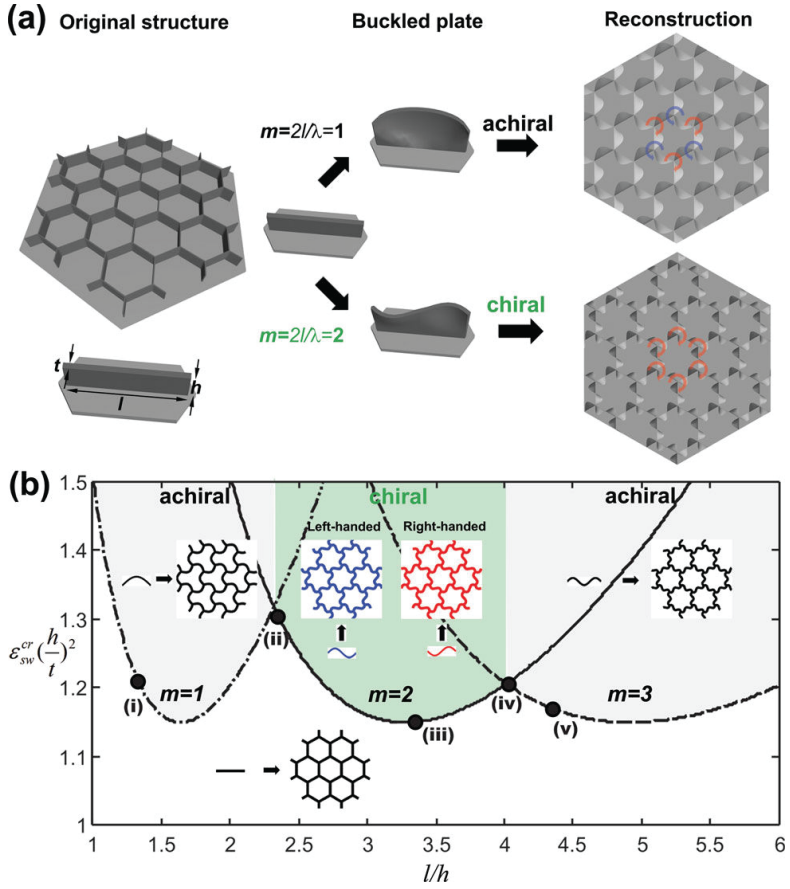

Figure 6.1: Design of structures. (a) Schematic approach to the design of supported cellular architectures with buckling-induced chiral or achiral reconfigurations. First, the cellular structure is deconstructed into individual supported plates and the wavelength λ of their buckling pattern is calculated. Then, the buckled pattern of the structure is reconstructed by connecting individual buckled plates. The color-coded arrows indicate the handedness of the vertices. (b) Results of the buckling analysis for a single supported thin, elastic plate are plotted in a stability diagram. Upon reaching a critical swelling strain $\varepsilon_{sw}^{c}r$, buckling modes of both half and full sinusoids can be achieved by adjusting l/h (the aspect ratio of the plate), resulting in respectively achiral and chiral patterns upon reconstruction of the cellular architecture. The circular black markers and corresponding Roman numbers indicate the aspect ratio l/h of macroscale honeycomb lattices ($l = 5\,mm$ and $t/l = 0.18$, see Figure 6.2(a)) that were fabricated and tested to verify the validity of the analytical model.

mentary Figures D.1 and D.2). These numerical calculations show that the thickness only marginally affects the buckling modes (Supplementary Figure D.2), confirming that the buckling-induced pattern of supported cellular structures is dictated by the aspect ratio l/h of the individual plates.

6.2.2 Experiments

Having ascertained the critical design parameters, to test the validity of our analytical model we fabricated surface-attached cellular structures with aspect ratios l/h that correspond to different regimes in the stability diagram, as indicated by the circular markers in Figure 6.1(b). We started with macroscale honeycomb structures ($l = 5\ mm$) comprising few unit cells and made from silicone rubber (see Experimental). When swelled, the structures yielded either chiral, achiral or mixed patterns (Figure 6.2(a) and Supplementary Figure D.3), exactly as predicted by our analysis (Figure 6.1(b)). We then fabricated samples comprising a larger number of unit cells with geometry corresponding to both the achiral ($l/h = 2$, $t/h = 0.37$ and $l = 5\ mm$) and chiral ($l/h = 3.17$, $t/h = 0.40$ and $l = 5\ mm$) regime in the stability diagram. Furthermore, since the analytical model is not limited to a specific cellular geometry, we also fabricated macroscale ($l = 5\ mm$) square lattices comprising plates with the same aspect ratio (Figure 6.2b). Again all the samples buckled as predicted by the analytical model (Figure 6.2c,d-left/center), showing that the design principles can be applied to different geometries.

Because the pattern formation exploits a mechanical instability that is scale-independent (where the continuum assumption holds), we extended the principle to microscale honeycombs ($l = 20\ \mu m$) made from epoxy resin (see Chapter D). The structures buckled upon immersion in N-methyl-2-pyrrolidone, and the stability diagram again correctly predicted the emergence of either chiral or achiral patterns (Figure 6.2(c,d)-right). Subsequently evaporating the solvent led to reconversion of the buckled structures back into the original configurations, demonstrating that the controlled pattern formation is fully reversible.

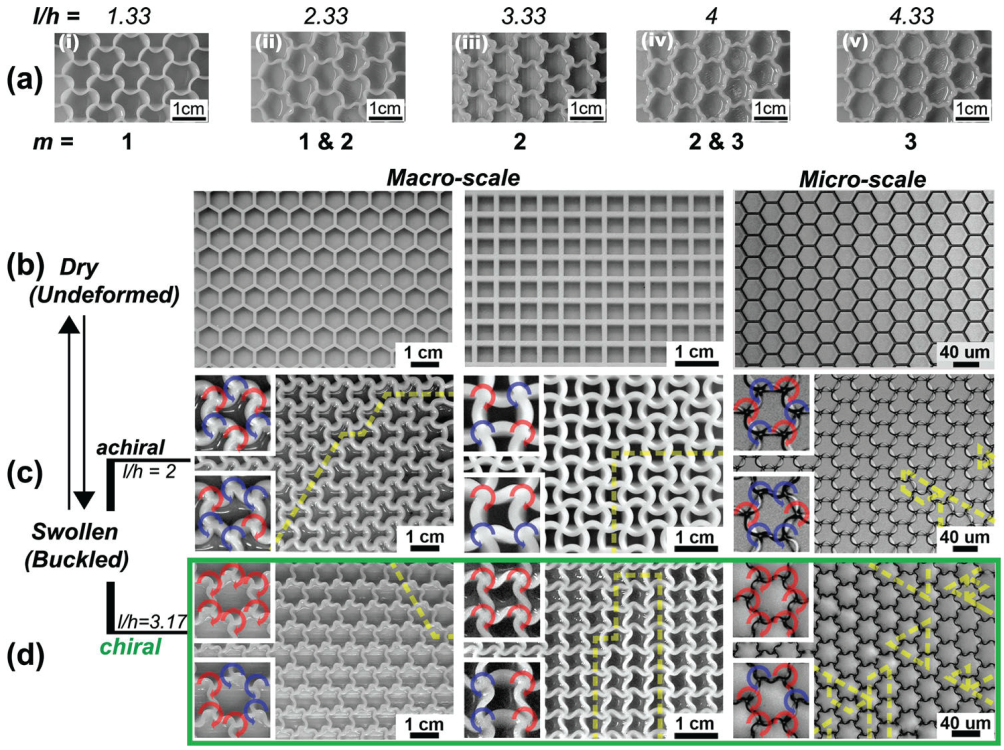

Figure 6.2: Verification of the stability diagram. (a) Buckling patterns of macroscale honeycombs with different aspect ratio l/h ($t/l = 0.18$ and $l = 5\,mm$ for all samples). The Roman numbers indicate the corresponding marker in the stability diagram (Figure 6.1(b)). The observed buckling mode (m) is shown below each image. Note that a mixture of modes is found for geometries lying on the boundary of adjacent regimes. (b)-(d) Buckling-induced reversible pattern formation in a supported macro-scale honeycomb lattice (left), macro-scale square lattice (center) and micro-scale honeycomb lattice (right) upon rapid swelling. (b) Optical images of original, undeformed structures. (c) For $l/h = 2, t/h = 0.37$, buckling induces an achiral pattern. (d) For $l/h = 3.17, t/h = 0.40$, a chiral pattern is observed. These buckling patterns are in agreement with the analytical predictions, but multiple domains are observed, whose boundaries are highlighted by the yellow dashed lines. The insets show zoomed-in images of the buckled patterns within the domains (top) and at the domain boundaries (bottom). The color-coded arrows indicate the handedness of the vertices.

6.3 Discussion on chiral amplification

Although all the experimental results show an excellent agreement with the analytical predictions, we observed a racemic mixture of chiral domains displaying both right- and left- handedness evolved from several nucleation events. At the boundaries of these domains (shown as yellow lines in Figure 6.2), the plates buckled either in the 1^{st} or 3^{rd} mode. Avoiding such racemic mixtures and making defect-free patterns with a single-handedness thus requires the prevention of multiple nucleation sites. We therefore gradually wetted the samples from a single location. This approach induced a unique nucleation event that propagated over the entire sample to yield uniform buckling patterns (Figure 6.3(a)). Remarkably, we observed that during the spreading of the pattern some plates initially buckled either in the wrong direction or with an unpredicted mode (Figure 6.3(b)). These defects were, however, repaired upon propagation of the swelling front through the defect site when the majority of the plates connected to the defect buckled correctly. The interconnected cellular architecture is therefore crucial to conserve the propagation of a single handedness over the entire substrate (Figure 6.3(d)) by allowing a self-repair mechanism through connected plates.

While instabilities can be induced by a number of stimuli, including thermal, electrical, and mechanical loadings (Supplementary Figure D.4), the convenience, versatility and, most importantly, the reversibility and directionality of the reconfiguration process that arises from swelling-induced buckling enables a unique mechanism where chirality can be chosen, reversibly written and amplified as described below.

Repeated swelling-unswelling revealed that the same buckling pattern reoccurred every time. The structure thus possesses memory of deformation, likely embedded in a previous reorganization of the polymeric network, which can steer the chiral outcome in a subsequent symmetry breaking event. This memory effect can be used to select the handedness of the chiral patterns at will. Since statistical analyses showed equal probability of left-handed and right-handed patterns in rapidly s-

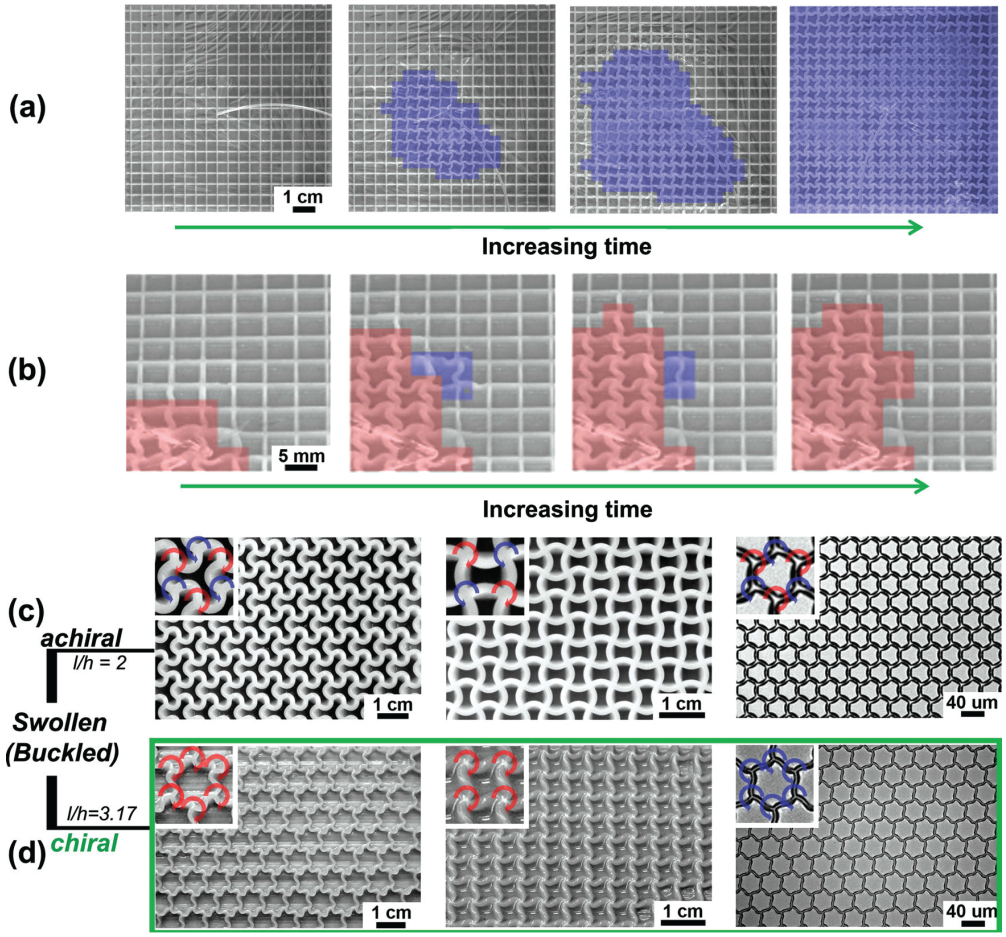

Figure 6.3: Uniform pattern formation by controlling nucleation. (a) Time-lapse series showing a single nucleation event and subsequent slow spreading of a buckling-induced chiral pattern by gradually wetting from a single location. (b) Time-lapse series of the self-repairing process. The initial defect in the form of few clockwise vertices (blue) is overwhelmed by the surrounding counterclockwise vertices (red), thus amplifying the chiral patterns of the nucleus. (c)-(d) The combination of the unique nucleation event and amplification mechanism results in either uniform achiral ($l/h = 2, t/h = 0.37$) (c) or chiral ($l/h = 3.17, t/h = 0.40$) (d) patterns. Zoomed-in images of the buckled patterns are shown in the insets; the color-coded arrows indicate the handedness of the vertices.

wollen structures (Figure 6.4(a,b)), one can map the domains of different handedness and choose a region of desired handedness as a seed. After unswelling the structure back into the initial pattern, we can initiate the slow, directional swelling of the structure starting from one of the mapped domains (Figure 6.4(c)). Remarkably, when the progressing pattern reached the previously identified domain boundaries, the handedness of the spreading pattern was still preserved, thereby overwriting the memory of these domains to yield patterns of uniform handedness by the repair mechanism discussed above. When the structure subsequently was unbuckled by drying and rapidly swollen again, we recovered the single-chirality pattern, confirming that the memory of initially racemic domains was indeed overwritten. This chiral memory is also durable: even after four months the memory is still preserved. Information on the handedness can thus be stored, read out, and overwritten providing a versatile programmable mechanism.

6.4 Conclusion

Guided by an analytical model and numerical calculations, here we show a proof of principle of buckling-induced local symmetry breaking and subsequent spreading of a chiral pattern to yield globally uniform configurations of single handedness in supported cellular structures. We experimentally demonstrate that this strategy offers a unique range of advantages: (i) it can be applied to structures with various length scales (where the continuum hypothesis holds); (ii) the reconfiguration occurs upon application of different stimuli and using different materials, so that it can be used to dynamically alter surface properties and morphology; (iii) the transformation can be made fully reversible; and (iv) most importantly, it can be controlled to yield either uniform achiral or chiral configurations with user-defined handedness.

In contrast to molecular symmetry-breaking reactions and crystallization systems, both the nucleation and propagation of chirality can be visualized directly to unravel the underlying mechanisms

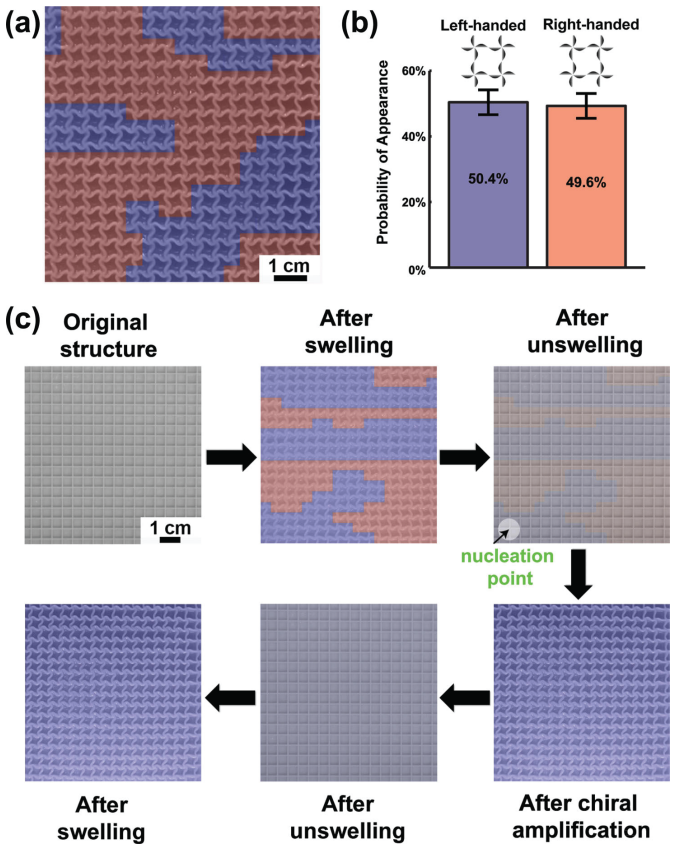

Figure 6.4: . Memory effect allowing readout, selection and overwriting of the handedness of the chiral pattern. (a) An example of a rapidly swollen macro-scale square lattice structures, showing a racemic mixture of left- and right-handed domains. (b) Statistical probabilities of the vertices rotate into right- and left-handed configurations from nine independent experiments using different samples. The error bar indicates the standard deviation of the respective probability. (c) These chiral domains can be selected and amplified. For this, we first map the chiral domains upon rapid swelling. Subsequently the structure is reconverted into the unbuckled configuration, where the handedness map is given in faded red and blue. Buckling is then initiated at a location selected from the chirality map to induce a uniform pattern of the desired handedness. If the structure is subsequently unbuckled and rapidly swollen, the uniform pattern is recovered, demonstrating that the chiral memory of the original racemic pattern is overwritten.

and fully control the pattern formation. This process not only provides a remarkable example of spontaneous symmetry breaking, but also outlines a general strategy in which a judicious choice of dimensions, materials, stimuli and architectonic designs provides a foundation for a wide range of multidisciplinary basic and applied studies. For example, our results could be used to design templates to facilitate fabrication of free-standing chiral structures. Moreover, in structures with sizes comparable to the wavelength of the light, our approach could lead to the design of novel thin film polarization converters, waveguides and circular dichroism spectroscopy substrates.

This project was a collaboration with Sung H. Kang, Jordan R. Raney, Pai Wang, Lichen Fang and Francisco Candido under the supervision of Prof. Jennifer A. Lewis and Prof. Katia Bertoldi. I was the one of lead researcher on this project and equal contribution author. I formulated the initial idea, finalized simulation, fabricated macroscale sample, and helped in preparation of the manuscript. The work in this chapter has already been submitted to Advanced Materials.

7

Multistable architected materials for trapping elastic strain energy

7.1 Introduction

Energy absorbing materials are widely deployed for personnel protection, crash mitigation in automobiles and aircrafts, and protective packaging of delicate components. Many strategies have

been investigated to create materials that efficiently dissipate mechanical energy, including plastic deformation in metals[50,122,128,131], fragmentation in ceramics[162], and rate-dependent viscous processes[50,32,52]. However, in all of these systems there are challenges associated with either reusability or rate dependency. Most recently, mechanical metamaterials have been fabricated in novel geometries to realize recoverable energy-absorbing behavior in elastic systems[42,106,30,135], suggesting novel strategies for mechanical dissipation of energy.

Here, we report a new class of architected materials in which all of the energy inserted into a system during loading is trapped in the form of elastic deformation of a large number of bistable elastic beams. Using direct ink writing[96], an extrusion-based 3D printing method, we rapidly fabricate customized energy-absorbing architectures. Their design, which is inspired by the exotic response of bistable elastic elements[59,119,46,44,65,60], is guided by numerical Finite Element simulations. Importantly, their energy trapping mechanism depends solely on the (reversible) change in state of prescribed structural geometries. Hence, their mechanical response is reversible and repeatable, and independent of scale, rate and loading history. Remarkably, these architected materials improve impact protection by an order of magnitude compared to the mechanisms previously proposed for elastic metamaterials[42,30].

7.2 Methods

7.2.1 Design Principle

To illustrate the proposed mechanism, we consider an elastic constrained tilted beam. In contrast to a vertical elastic beam that buckles under axial compression, but fully recovers its initial shape when unloaded (Figure 7.1a), a tilted beam may snap between two different stable configurations[8,164,40,119] and retain its deformed shape after unloading (Fig. 7.1b). Interestingly, such a bistable tilted beam is capable of locking in most of the energy inserted into the system during loading (quantified by the

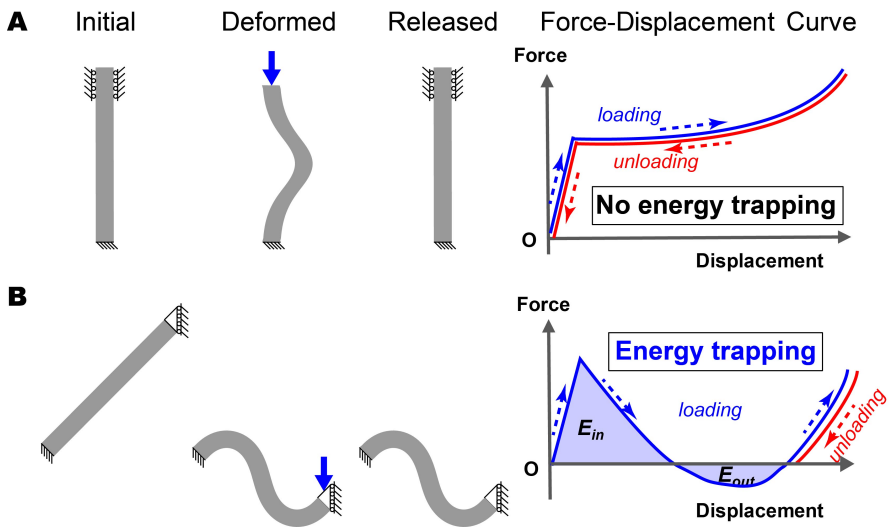

Figure 7.1: Energy absorption in an elastic beam. a, An elastic beam buckles when axially compressed, yet fully recovers to its initial shape when unloaded. **b,** A constrained tilted elastic beam may snap between two stable configurations, when one of its ends is moved vertically. In this case, the structure maintains its deformed shape when unloaded. [Note The bistable beams lock in most of the energy inserted into the system during loading ($E_{locked} = E_{in} - E_{out}$). Their initial (undeformed) configuration can be recovered when an amount of energy larger than E_{out} is supplied to the system.]

shaded area under the corresponding force-displacement curve), indicating that it can be used as an energy absorbing element.

To create energy trapping architected materials that exploit the bistability of tilted elastic beams, it is necessary to accurately control structural features. Direct ink writing offers a facile method for rapidly fabricating materials composed of arrays of tilted elastic beams in programmable motifs, whose mechanical response can then be systematically characterized. Using this 3D printing technique, viscoelastic inks are extruded through fine deposition nozzles in a layer-by-layer manner[53,150,2]. The inks exhibit shear-thinning behavior, which facilitates their flow through the nozzle during printing, as well as a shear elastic modulus that ensures that the printed features are self-supporting. Specifically, we used a polydimethylsiloxane (PDMS) ink to print energy-trapping, architected materials (Figures F.1-F.2). This silicone-based ink maintains its structural integrity prior

to cross-linking the printed structures at 100°C for 30 min to yield an elastomeric material with an initial shear modulus $\mu_o = 0.32$ MPa (Figure F.3). We note that direct ink writing is particularly well-suited to our beam-based geometries, since narrow features with tunable aspect ratios can be readily fabricated by locally varying the print velocity.

7.2.2 Parametric Study

To optimize their geometry, we combined experiments and simulations to systematically investigate the effects of tilting angle ϑ and beam slenderness t/L (with t and L denoting the thickness and length of the beam, respectively) on the desired energy-trapping response (Figure 7.2). We designed and fabricated a minimal structure consisting of two identical tilted beams, arranged symmetrically to prevent asymmetric deformation, and connected by two stiff horizontal layers (in-filled epoxy) to constrain lateral motion at their ends (Fig. 7.2a,b). We rapidly printed dozens of functional, but minimal, units (each structure requiring only a few minutes to fabricate). We specifically explored geometrical parameters (Fig. 7.2a-b) ranging from $\vartheta \sim 1.5°$-$70°$ and $t/L \sim 0.10$-0.33 with $L \sim 1$-6 mm. We note that smaller structures could be fabricated using smaller nozzle sizes, while larger structures can be produced via a molding approach (Figures F.4 and F.5).

Using Finite Element (FE) simulations, we built two-dimensional numerical models of tilted beams characterized by different combinations of ϑ and t/L and investigated their response under uniaxial compression using the commercial finite element package ABAQUS/Explicit. Each tilted beam is deformed by applying a vertical displacement to the top end, while constraining the motion of both ends in the horizontal direction (see Fig. 7.2c). Quasistatic conditions are ensured by monitoring the kinetic energy and introducing a small damping factor (see Chapter F). Our experimental and numerical results are in good agreement, as reported in Fig. 7.2d-e. The force-displacement curves shown in Fig. 7.2d clearly indicate that the system's response can be tuned by controlling ϑ and t/L. For example, we find that the beams snap during compression when

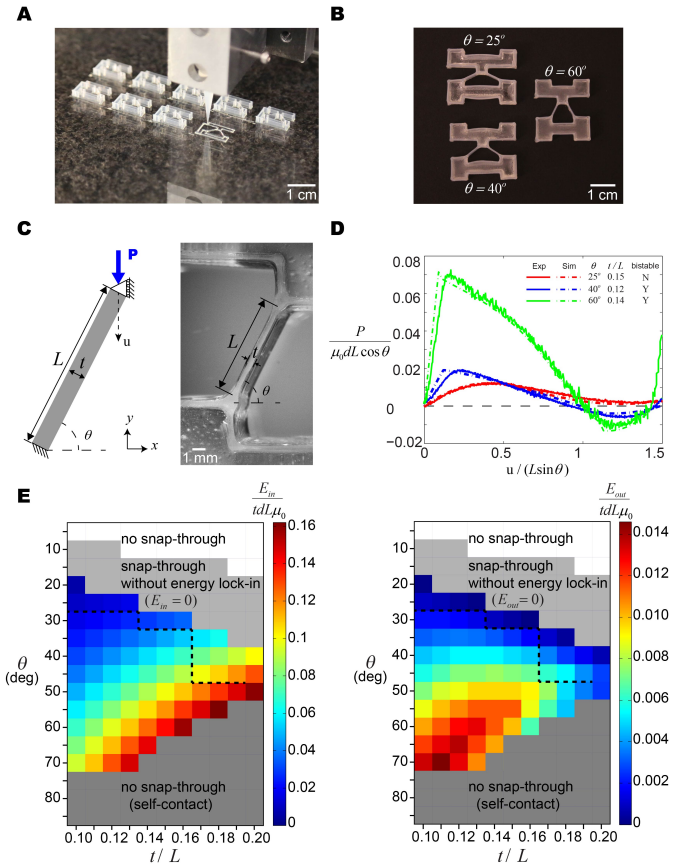

Figure 7.2: Mechanical response of a constrained, tilted elastic beam. **a,** Minimal functional structures, each with a unique combination of geometrical parameters, are rapidly printed (150-200 s each) using direct-write 3D printing. **b,** Minimal structures consisting of two identical tilted beams. **c,** Schematic view showing the 2D model used in our FE simulations (left) and the corresponding beam in the fabricated minimal unit (right). **d,** Numerical and experimental force-displacement curves for three beams characterized by $(\vartheta,\ t/L)\ =(25^{\circ},\ 0.15),(40^{\circ},\ 0.12),(60^{\circ},\ 0.14)$. The force is normalized by $\mu_{o}L\,d\,\cos\vartheta$ (d denoting the out-of-plane thickness of the samples), while the displacement is normalized by $L\sin\vartheta$. **e,** Effect of ϑ and t/L on the energy absorbed by the elastic beam (E_{in}) and the energy cost for the beam to snap back to its undeformed configuration (E_{out}). The black dashed lines indicate the experimentally observed transition between the geometries that result in bistability and those that merely possess the snap-through instability, but are not bistable.

$(\vartheta,\ t/L) = (25°,\ 0.15)$, but return to their initial (undeformed) configuration after the load is removed (i.e., only the initial configuration is stable). However, for $(\vartheta,\ t/L) = (40°,\ 0.11)$ and $(60°,\ 0.14)$, there is a brief period of tensile reaction force (see region with negative force in the results in Fig. 7.2d), so that the system is bistable and can lock in most of the energy applied during loading.

To further explore the effect of t/L and ϑ, we carried out a combined numerical and experimental parametric study. The numerical results, summarized in Fig. 7.2e, indicate that by increasing ϑ, at constant t/L, the response of the beams undergoes several transitions. For low values of ϑ (i.e., nearly horizontal beam orientation, perpendicular to the loading direction), the system exhibits no instabilities (white region in Fig. 7.2e). Above a critical value of ϑ, a snap-though instability is triggered (light grey region in Fig. 7.2e), but without bistability. However, in both of these cases, the system returns to its initial configuration upon unloading, i.e., no energy is trapped, which greatly limits their potential for energy absorption. If ϑ is further increased, the beam becomes bistable (colored area in Fig. 7.2e), enabling energy trapping. The geometrical transformation between undeformed and deformed stable states is akin to a phase change, in which the quantity of energy that is trapped depends solely on the net change in deformation, i.e., independent of how the load is applied and of loading history. Finally, if ϑ is increased above a critical threshold, the snap-through instability is suppressed (grey area in Fig. 7.2e) due to self-contact.

Within the bistable domain, the energy that the system absorbs (E_{in}) increases as a function of both ϑ and t/L. However, the energy cost for a beam to snap back to its undeformed state (E_{out}) tends to decrease. As a result, it is likely that for large values of ϑ and t/L (within the bistable region) the system cannot maintain the second stable configuration due to small geometric imperfections or even a time dependency (e.g., viscoelasticity) of the material itself. To design optimal energy trapping beams, one must maximize E_{in} while maintaining E_{out} above a threshold that depends on the environment for which the system is designed. To complement the numerical study, we carried out

an experimental parametric study by fabricating minimal structures over the same combinations of ϑ and t/L. Of particular interest is the transition between the geometries that exhibit bistability and those that merely possess the snap-through instability, but are not bistable. The black dashed lines in Fig. 7.2e indicate the approximate location of this transition, as measured experimentally, which is in good agreement with the numerical results. Discrepancies arise from the fact that structural defects become more important near the transition, since E_{out} is very low there (see Chapter F). Note, this transition is important, not only because the bistability enables energy trapping, but also because it could be used in the design of deployable mechanical structures to achieve controlled sequential displacement. Finally, we have also observed that this structural design can be combined with stimuli-responsive materials to produce structures capable of recovering when exposed to an environmental cue.

7.2.3 Quasi-static Tests

Interestingly, the bistable elastic beams can be arranged to form 1D, 2D or 3D energy-trapping metamaterials (Fig. 7.3a). To demonstrate the concept using a system designed to deform uniaxially, we fabricated a 4x4 array of minimal units (i.e., two symmetric beams), for a total of 32 tilted beams. As shown in Fig. 7.3b, if t/L and ϑ are chosen such that each beam is bistable (in this case, ϑ=40° and t/L=0.12, with L =5 mm), the structure is characterized by multiple stable configurations that can be triggered by applying a compressive force and that are maintained also when the force is removed. In fact, a tensile force needs to be applied to recover the initial shape. We then characterized the response of the structures under uniaxial compression using a single-axis Instron with a 10 N load cell. As shown in Fig. 7.3c, the force-displacement response is characterized by four similar peaks, each corresponding to the collapse of a row of beams. Since each row is designed with the same geometrical parameters, these peaks occur at a nearly identical force (with small imperfections or the environment leading to sequential, rather than simultaneous, collapse of the rows). Remarkably, the

magnitude of these peaks for the 4x4 structures is in excellent agreement with that observed from the tests of the minimal unit, highlighting the modularity and scalability of this structural motif. When these structures are compressed at different speeds (between 10 mm/s and 0.1 mm/s), their force-displacement curves are shown to be rate-independent, and they absorb the same amount of energy per unit mass when fully compressed. Their remarkable insensitivity to loading conditions is due to the fact that all energy inserted into these architected metamaterials is locked-in in the form of elastic strain energy. Therefore, the absorbed energy depends only on the morphological change between the initial (undeformed) state and the final (deformed) state of the beam.

Each of the four layers of the structure in Fig. 7.3 consists of eight tilted beams in parallel, with each of these layers arranged in series. Given this modularity, the total structural response can be predicted using the FE result for the corresponding single beam (see Chapter F). The agreement between numerical and experimental results (Fig. 7.3d) is excellent, demonstrating that the knowledge of the response of our simple building block is enough to design larger and more complex structures with tailored properties. Moreover, although the results reported in Fig. 7.3b-d are for a structure characterized by L =5 mm, the same strategy can be applied to structures with various length scales (Fig. 7.3e), since we exploit a geometrical transformation that is scale-independent (where the continuum assumption holds) and relies solely on the aspect ratio and the orientation angle of the beams.

7.2.4 Impact Tests

We also characterized the ability of the system to provide protection during impact by dropping the samples from different heights, h, while recording the acceleration with a piezoelectric accelerometer (PCB Piezotronics, Inc., model number: 352C23) attached to their top surface. To investigate the general efficacy of this energy-trapping mechanism, we performed impact tests (*i*) on multistable structures in their low-energy, undeformed configuration; (*ii*) on the same multistable structures

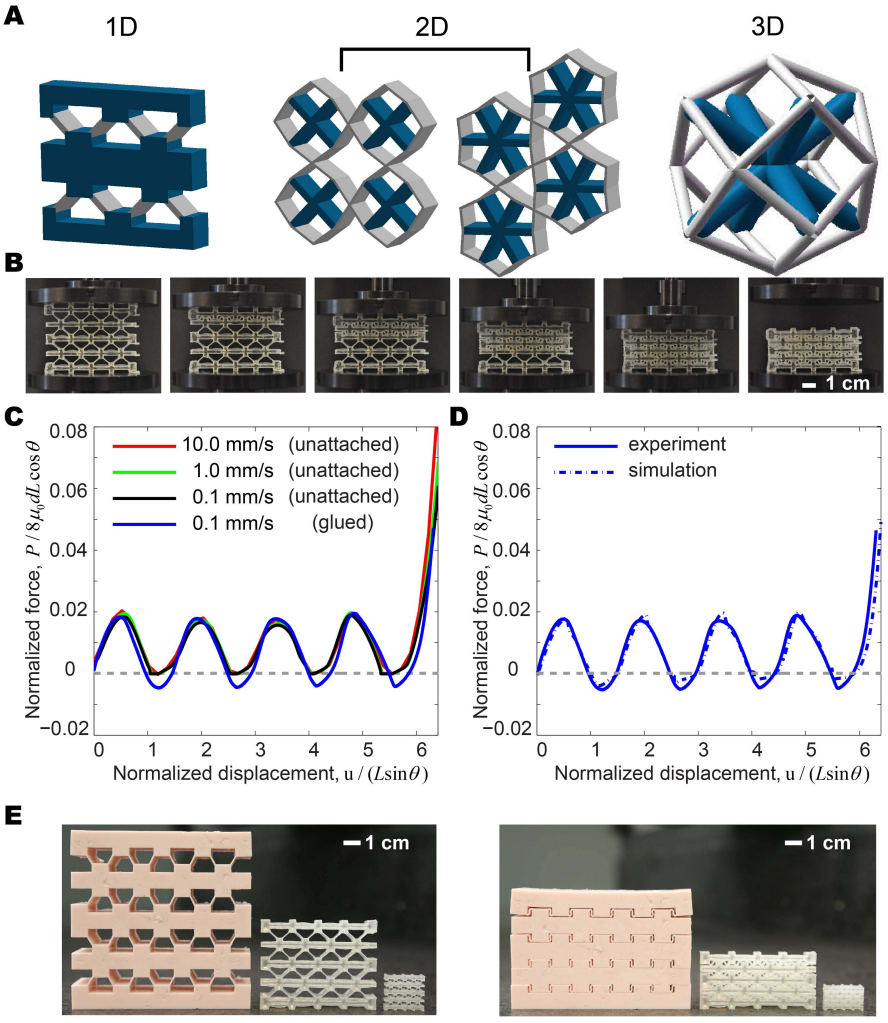

Figure 7.3: Mechanical response of an elastic multistable structure. a, Schematic views of 1D, 2D and 3D energy-trapping metamaterials. The bistable beams are colored in grey, while the rigid support structures are colored in blue. **b,** Sequential images of the multistable structure loaded vertically. The sample retained its deformed shape after unloading. **c,** Stress-strain curves for the multistable structure at multiple strain rates. The measurements are repeated five times for each strain rate, showing excellent repeatability for a given sample and also between multiple samples with the same geometric properties. **d,** Comparison between experiments and simulations. The numerical predictions are obtained using the FE results for a single tilted beam with $\vartheta = 40^\circ$ and $t/L = 0.12$ and by assuming that the structure consists of four layers arranged in series, each with eight tilted beams in parallel. **e,** Examples of different structures fabricated at different length scales (left - initial, right -deformed).

in their densified state (effectively, the "control" case, behaving as a block of material); and (*iii*) on structures with low beam angles ($\vartheta = 20°$), which possess a snap-through instability, but are not multistable. First, we see that the control sample, which is the densified multistable structure, propagates a very large peak acceleration during impact (grey line in Fig. 7.4a-b). As we demonstrate, elastic metamaterials that are based on the snap-through instability, similar to those reported previously[30,42,106], show a reduced peak acceleration (green line) relative to the densified structure due to their material-dependent, viscoelastic dissipation. However, by introducing energy-trapping via our multistable samples (red line), the peak acceleration during impact and the structure's protective capability are improved by an order of magnitude for a given mass of material (Fig. 7.4a-b).

Further comparison between the multistable, snap-through, and control samples clearly shows the ability of the energy-trapping beams to improve impact performance, yielding up to an order of magnitude reduction in peak acceleration amplitude when h was varied between 5 and 10 cm (Fig. 7.4c). For samples designed to possess the snap-through instability without energy-trapping ($\vartheta = 20°$ and t/L=0.11), significantly less energy is absorbed despite having very similar relative density to the energy-trapping structures. The simulations predict no energy absorption for the samples without energy-trapping, since material dissipation is not accounted for; however, there is a small amount of energy absorption in the experiments because of viscoelasticity.

The acceleration-time curve for multistable samples is characterized by 4 peaks at $a \sim 80$ m/s^2, each corresponding to the collapse of a line of beams. This acceleration corresponds to a force $F = m \times a = 0.125g \times 80m/s^2 = 10N$, which is in excellent agreement with the collapse-force measured during the quasi-static compression of the structures (see Chapter F). This remarkable result further highlights the rate-independent mechanics, since the collapse-force during impact would not typically be expected to be the same as during quasistatic compression[191]. As the drop height h is increased (Fig. 7.4d), eventually the kinetic energy of the structure immediately prior to impact exceeds the cumulative absorptive potential of the snapping beams in all four rows. As a result, for

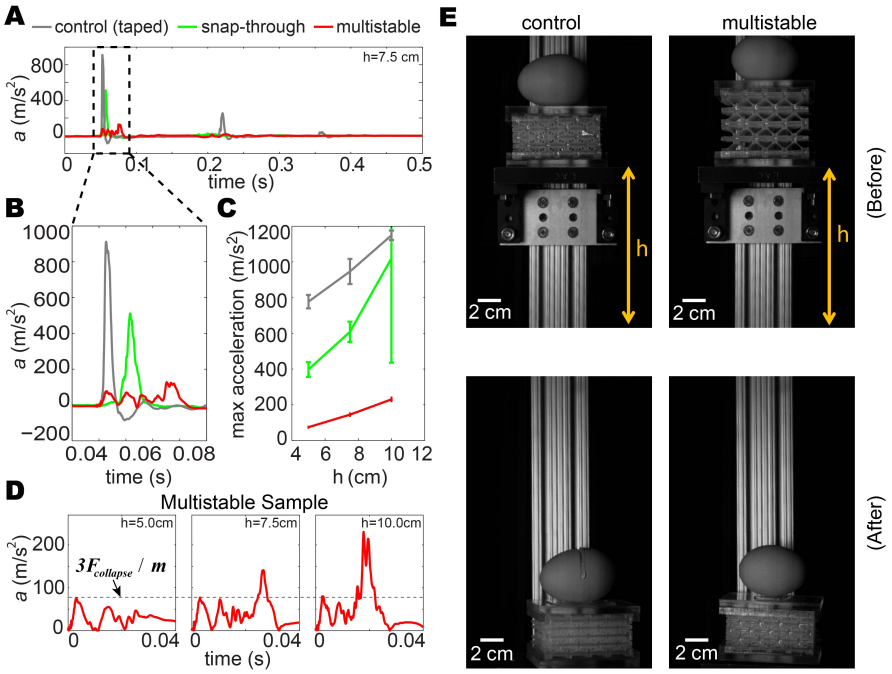

Figure 7.4: Drop tests. **a,** Acceleration-time curve for a multistable structure, the corresponding control sample (consisting of the same structures but taped to make all beams intentionally collapsed prior to the drop test), and a structure designed to possess snap-through instabilities but not energy-trapping, with samples dropped from $h = 7.5$ cm. **b,** Zoom-in of the acceleration-time curves. **c,** Peak acceleration amplitude as a function of the dropping height h for the multistable structure, the control sample, and the snap-through sample. The error bars indicate standard deviations from multiple (N>5) measurements. **d,** Acceleration-time curves for the multistable sample obtained from drop heights of $h = 5$ cm, 7.5 cm and 10 cm. The horizontal dotted line indicates the collapse-force divided by the mass of the egg for a line of tilted beams. The force is three times larger than that measured in the static compression tests since here we used three identical structures arranged in parallel for the drop tests. **e,** Drop of multistable and control samples with raw eggs attached to their top from $h = 12.5$ cm. The eggs attached to the multistable structures survive, while those on the control samples break upon impact.

high enough h (7.5 cm and above in this case) an additional acceleration peak emerges, corresponding to loading of the densified structure after all four rows of beams have fully collapsed. We can optimize the design for a given application by maximizing the energy dissipated during collapse of the beams subject to the constraint that the acceleration remains below a particular damaging acceleration. This can be controlled by varying the structural parameters (ϑ and t/L) as well as the out-of-plane thickness of the structure.

The energy-trapping capability of our multistable, architected materials could be beneficial for protecting an object and/or a person from impact. To illustrate this, we dropped multistable and control samples with raw eggs attached to their top surface. As shown in Fig. 7.4e, the eggs attached to the energy-absorbing structure remain intact, while those attached to the control samples break upon impact. Importantly, after the impact, these multistable architected materials can be reused, maintaining the same energy absorption characteristics regardless of loading history.

7.3 Conclusion

In summary, by combining numerical calculations and 3D printing, we have developed fully elastic and reusable energy-trapping architected materials based on localized locking-in of strain energy in tilted elastic beams. Our strategy offers several advantages; it can be applied to structures with various length scales (from micro to macro) and provides a simple modular design scheme, so that the mechanical response can be tuned by controlling geometric parameters guided by a "phase diagram". Moreover, the loading process is fully reversible, allowing the structures to be consistently reused many times, with the energy absorption unaffected by loading rate or history. Since the quantity of energy that is trapped in these metamaterials depends solely on their morphological change between the initial (undeformed) and final (deformed) state of the elastic beams, their response is highly predictable for a wide variety of loading conditions. Our findings open new op-

portunities for designing energy absorbing materials for applications including reusable personnel protection, crash mitigation in automobiles and aircraft, and protective packaging of delicate components.

8

Conclusion and summary

By combining numerical simulations and experiments, I showed that a novel class of soft functional structures can be designed that use their large deformation and geometric rearrangements induced by instabilities to change their properties, including shape, volume, Poisson's ratio, chirality, energy absorption and phononic band-gaps. Interestingly, since the structures are built using elastomeric materials, their response is fully reversible and they can be consistently reused many times. Moreover, since the structures I studied take advantage of buckling, which is a scale-independent mech-

anism, the principles can be applied over a wide range of length scales. With recent developments in microscale fabrication, I believe the miniaturization of the proposed structures can lead to the generation of a new class of tunable devices.

The major accomplishments and findings of the thesis are summarized as follows:

1. We showed that by simply changing the shape of the holes the response of porous structure can be easily tuned and soft structures with optimal compaction can be designed.

2. We have identified four periodic distributions of mono-disperse circular holes in planar elastic structures where mechanical instability can be exploited to reversibly switch between expanded and compact configurations. Interestingly, in two of these structures (i.e. 3.6.3.6 and 3.4.6.4) the instability can be exploited to induce the formation of a chiral pattern.

3. We discovered a fundamentally new way of generating isotropic 2D materials with negative Poisson's ratio by embedding periodic arrays of cuts in elastomeric sheets. Interestingly, we showed that Poisson's ratio of the system can be easily tuned and drastically altered by varying the length of the cuts, while the isotropy of the system is controlled by the degree of rotational symmetry of the cut-patterns.

4. We demonstrated both numerically and experimentally the design of highly tunable phononic crystals by harnessing multiple folding mechanisms in periodic elastomeric structures comprising a triangular array of circular holes. Remarkably, the dynamic response of the system was found to be highly affected by the pattern induced by buckling, demonstrating that the band gaps can be tuned both by deformation mode and the extent of deformation.

5. Guided by a theoretical model, we here exploit buckling in rationally designed supported cellular structures at the mesoscale to reversibly switch between the initially achiral configurationand subsequent uniform left- or right- handed configurations.

6. We combined 3D printing and numerical analysis to design a new class of elastic metamaterials in which all the energy inserted into the system during loading is trapped in the elastic deformation of a large number of bistable elastic elements.

In summary, I believe that the insights gained in the thesis can serve as basis and guidelines for designing novel soft active material and structures, and can lead to more practical applications in the future. Let me finish this thesis by sharing a belief which I hold throughout my PhD - *Soft functional materials start where conventional materials fail.*

A

Supporting Information for Chapter 2

A.1 Materials

A silicone-based rubber (Elite Double 8, Zhermack) was used to cast the experimental specimen. The mechanical response of the material was characterized performing uniaxial tensile tests on samples with rectangular cross-section and shoulders. In addition, an extensometer was used to provide a more accurate measure of the stretch. The material response up to an applied stretch $\lambda = 2$ was

found to be well captured using a nearly incompressible Neo-Hookean model, whose strain energy is $W = \mu_0/2(\bar{I}_1 - 3) + K_0/2(J-1)^2$, with $\mu_0 = 0.33\,kPa$ and $K_0 = 555\,kPa$. Here, $\bar{I}_1 = \mathrm{tr}\left[\mathrm{dev}\left(\mathrm{F}^T\mathrm{F}\right)\right], J = \det\mathrm{F}$, F is the deformation gradient and μ_0 and K_0 denote the shear modulus and bulk modulus at zero strain, respectively. Note that Young's modulus E^* and Poisson ratio ν^* at zero strain can be easily obtained as $E^* = 9K_0\mu_0/(3K_0+\mu_0)$ and $\nu^* = 0.5(3K_0-2\mu_0)/(3K_0+\mu_0)$.

A.2 Testing and analysis

Compression tests were performed using an Instron machine with a 10N load cell. During the tests the specimens were positioned on an horizontal plate and compressed by a flat fixture mounted to the vertical compressing head. Both fixtures were made of transparent acrylic. Note that the specimens were not clamped to the two horizontal fixtures and that friction between the sample and fixture surface was enough to fix the position of the specimen top and bottom boundary (no lubrificant was used on the horizontal surfaces). The parallelism of the two horizontal flat fixtures was carefully monitored during the tests. The specimen during the test was held by an acrylic plate at the back directly mounted to the load cell to avoid out-of-plane buckling. The sample faces were covered with vaseline to reduce any frictional effects resulting during the loading process. The compression tests were performed at 20mm/min until the maximum load of the load cell, 10N, was reached. The results were independent of the rate of change of displacement for slower speeds and hence a good approximation to the rate independent conditions of the numerical investigation was obtained in the experiments. The load associated with the displacement was recorded and used to produce stress-strain curves for the compression process. During the test, a Nikon D90 SLR camera facing the specimen was used to take pictures and videos. Marking the corners of RVEs in our specimen with black dots enabled us to evaluate the geometric change quantitatively with a post-processing code in MATLAB.

B

Supporting Information for Chapter 3

B.1 Analysis - Design principles

B.1.1 From tilings of the 2D Euclidean plane to porous structures

To identify possible periodic monodisperse circular hole arrangements in elastic plates where buckling can be exploited as a mechanism to reversibly switch between undeformed/expanded and deformed/compact configurations, we investigate the hole arrangements by considering geometric

constraints on the tilings (i.e., tessellations) of the 2D Euclidean plane.

In order for all the monodisperse circular holes to close through buckling of the ligaments, the plates should meet the following requirements: (a) the center-to-center distances of adjacent holes are identical, so that all the ligaments are characterized by the same minimum width and undergo the first buckling mode in an approximately uniform manner; (b) there is an even number of ligaments around every hole, so that the deformation induced by buckling leads to their closure. Mathematically, these geometric constraints can be rephrased as: the skeleton of the porous structure should (a') be a convex uniform tiling of the 2D Euclidean plane (which are vertex-transitive and have only regular faces) (b') with an even number of faces meeting at each vertex. Focusing on 1-uniform tilings (i.e. Archimedean tilings) where all the vertices are the same, so that all the holes deform similarly, we find that there are only four tessellations which meet the above requirements: *square tiling*, *triangular tiling*, *trihexagonal tiling* and *rhombitrihexagonal tiling* (see Fig. B.1-A). The corresponding porous structures are then obtained by placing a circular hole at each vertex of the four tilings (see Fig. B.1-B). Finally, we note that each periodic porous structure has an underlying kinematic model which comprises of a network of rigid polygons and hinges (see Fig. B.1-C). These kinematic models can be obtained by transforming the circular holes either to (*i*) squares, if they are surrounded by four thin ligaments (as in the cases of 4.4.4.4, 3.6.3.6, 3.4.6.4); or (*ii*) hexagons, if they are surrounded by six thin ligaments (as in the cases of 3.3.3.3.3.3).

The kinematic models can then be used to study the deformation mechanism of the corresponding porous structures. Fig. B.2 shows the folding mechanism of the four kinematic models investigated in this study.

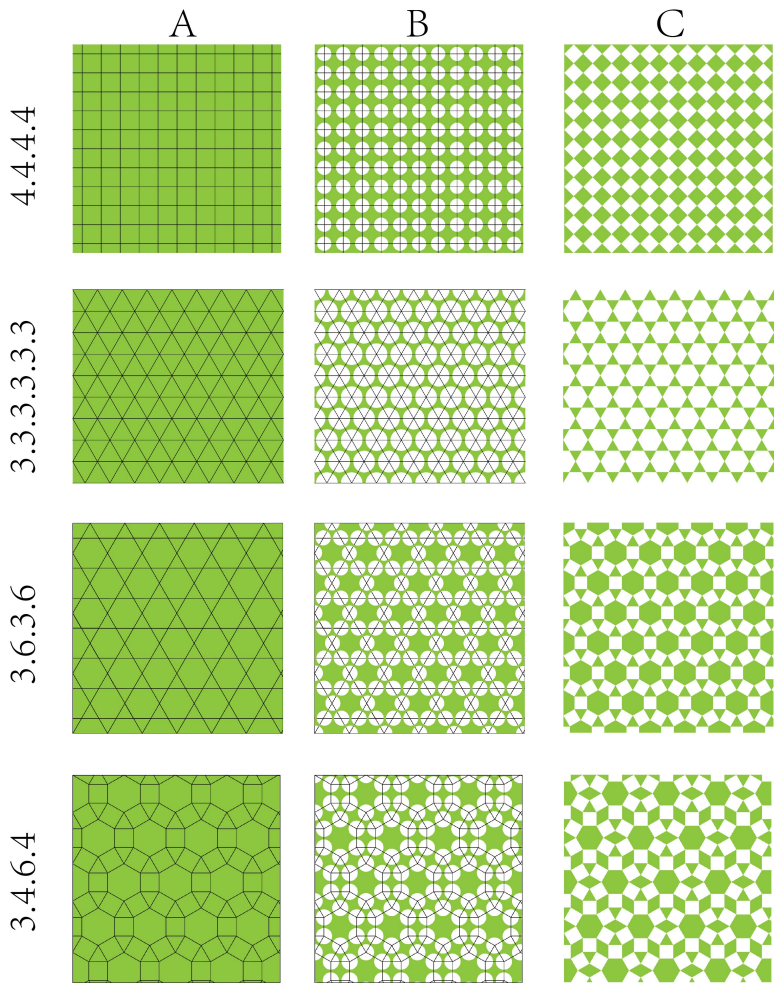

Figure B.1: From tilings to porous structures. (A) We start with a solid sheet of material and draw a tiling pattern on the sheet. (B) The corresponding porous structure is then obtained by placing a circular hole at each vertex of the tiling. (C) The corresponding kinematic model can be obtained by transforming the circular holes either to squares or hexagons.

B.2 Dislocation Dipole Model

It has been recently shown that the patterns induced by buckling in periodic porous structures can be investigated by making use of continuum elasticity theory and approximating the deformed holes as elastic dipoles[105]. The stress fields due to elastic dipoles are long ranged and dipoles interact with

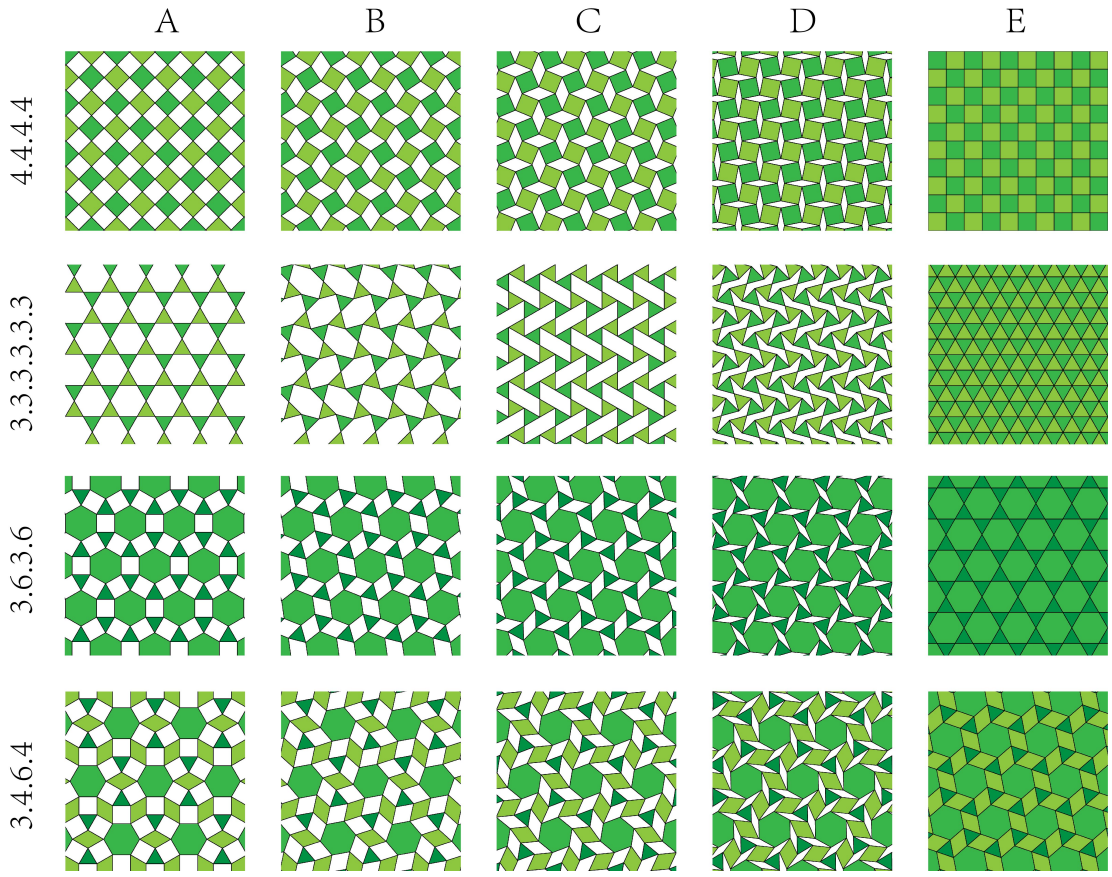

Figure B.2: Folding mechanism of the kinematic models. (A) completely unfolded configuration; (B),(C) and (D) intermediate configurations; (E) completely compact/folded configuration. The polygons are colored differently only for visualization purposes.

each other with interaction energy [105]

$$U_{\text{int}} = -\frac{E}{\pi}\frac{b^2 d_1 d_2}{R^2}\left[\cos\left(\vartheta_1 + \vartheta_2\right)\sin\vartheta_1 \sin\vartheta_2 + \frac{1}{4}\right], \tag{B.1}$$

where E is the 2-dimensional Young's modulus of bulk elastic medium, R is distance between two dipoles, d_1 and d_2 are magnitudes of dipole vectors, and ϑ_1 and ϑ_2 are dipole orientations (Fig. B.3A). We note that individual elastic dipoles also feel the effect of the external uniaxial compression [105], but this contribution is neglected in this study. Assuming periodic boundary conditions and inde-

pendent orientations of dipoles inside the primitive cell (Fig. B.6), we minimized the interaction energy of elastic dipoles B.1. For each dipole, we included interactions with $\sim$ 100 nearest dipole neighbors. The patterns that correspond to the minimized interaction energy of elastic dipoles in the four arrangements investigated in this study are shown in Fig. B.3. The patterns closely resemble the patterns obtained with FE analysis (see Fig. 1-C).

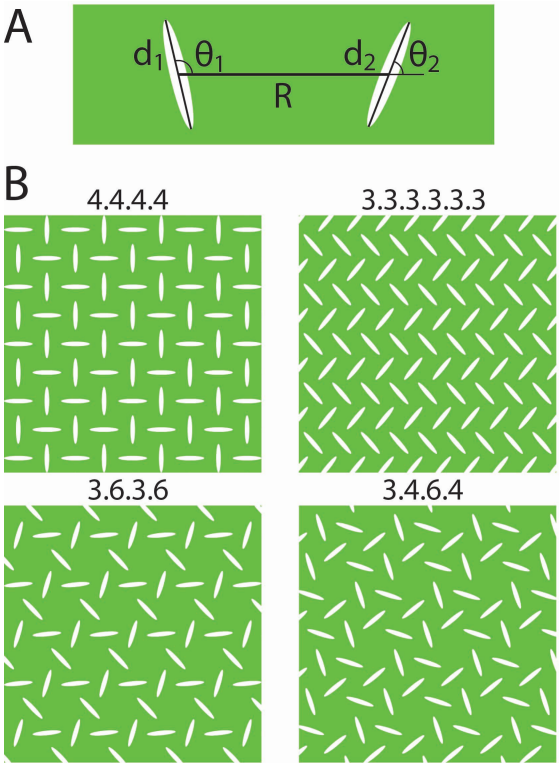

Figure B.3: (A) Diagram of the interaction between two elastic dipoles (d_1 and d_2) separated by R. (B) Patterns that correspond to the minimum free energy of interactions between elastic dipoles for the four structures considered in this study.

B.3 Experiments

B.3.1 Material

Silicone rubber (Vinylpolysiloxane: Elite Double 32, Zhermack) was used to cast the experimental specimens. The material properties were measured through tensile testing, up to a nominal strain $\varepsilon = 0.82$. No hysteresis and rate dependence was found during loading and unloading. The stress-strain behavior was found to be accurately captured by a Yeoh hyperelastic model[185], whose strain energy density is

$$W_{\text{Yeoh}} = \sum_{i=1}^{3} \left[C_{i0} \left(\bar{I}_1 - 3 \right)^i + (J-1)^{2i} / D_i \right] \tag{B.2}$$

where $\bar{I}_1 = \text{tr}\left[\text{dev}\left(\text{F}^T\text{F}\right)\right], J = \det[\text{F}]$, and F is the deformation gradient. Note that two of the parameters entering in Yeoh model are related to the conventional shear modulus (G_0) and bulk modulus (K_0) at zero strain as $C_{10} = G_0/2$ and $D_1 = 2/K_0$. To capture the behavior of the silicone rubber used in the experiments we used $C_{10} = 154\ kPa$, $C_{20} = 0\ kPa$, $C_{30} = 3.5\ kPa$, and $D_1 = D_2 = D_3 = 38.2\ GPa^{-1}$.

B.3.2 Specimens fabrication

The molds to cast the specimens were fabricated using a 3-D printer (Connex 500, Objet Ltd.) having a resolution of 600 *dpi* and a claimed printing accuracy of 30 μm. A very thin layer of mold release oil (Ease Release 200, Smooth-on Inc.) was sprayed onto the mold prior to molding. Then, the silicone rubber was cast into the mold. The casted mixture was first allowed to set in a vacuum for 10 minutes and then was placed at room temperature until curing was completed. The overall sizes of the four specimens are $W(\text{width}) \times H(\text{height}) \times T(\text{thickness}) = 80.0 \times 80.0 \times 35.0 mm$, $86.6 \times 75.0 \times 35.0 mm$, $93.3 \times 97.0\ mm \times 35.0\ mm$ and $132.0 \times 137.1\ mm \times 55.0\ mm$ for 4.4.4.4, 3.3.3.3.3.3, 3.6.3.6, 3.4.6.4, respectively. Note that large out-of-plane thicknesses were employed for all the specimens in

order to avoid out-of-plane buckling modes during the uniaxial compression tests. The four samples were designed to have a void-volume-fraction $\psi = 0.50$ and holes with radius $r = 4.0\ mm$. This resulted in a center-to-center distance between adjacent holes of $a = 10.8\ mm$ for the 3.3.3.3.3.3 pattern, $a = 9.3\ mm$ for the 3.6.3.6 pattern, and $a = 9.7\ mm$ for the 3.4.6.4 pattern. Note that the fabricated samples were found to have a slightly lower void-volume-fraction (i.e. $\psi_{4.4.4.4} = 0.49$, $\psi_{3.3.3.3.3.3} = 0.48$, $\psi_{3.6.3.6} = 0.49$, $\psi_{3.4.6.4} = 0.49$), due to the limited accuracy of the 3D printer. This deviation has been accounted for in the simulations.

B.3.3 Testing

Uniaxial compressive experiments were performed on a standard quasi-static loading frame (Instron 5566) with a 10 kN load cell (Instron 2710-106) in a displacement-controlled manner. The specimens were compressed within flat compression fixtures. Note that the specimen was not clamped to the fixtures, but friction between the specimen and fixture surface was enough to hold the position of the specimens' top and bottom faces because no lubricant was used on the horizontal surfaces. The compression tests were performed at the cross-head velocity of 20 mm/min until the holes were almost closed. During the test, a Nikon D90 SLR camera facing the specimen was used to take pictures at every nominal strain increment of $\Delta\varepsilon = 0.006$. The specimens were marked with black dots, so that we were able to quantify the changes in the geometry of the structures induced by deformation with a post-processing code in MATLAB.

B.3.4 Calculation of $\bar{\varepsilon}_{xx}$, $\bar{\varepsilon}_{yy}$, $\bar{\nu}$ and , $\bar{\nu}_{inc}$ from experiments

To quantify the lateral contraction (and thus the negative Poisson's ratio) of the porous structures in experiments, we investigated the evolution of the microstructure. The physical samples were marked with black dots as shown in Fig. 2 in the main text and their position was recorded using a high-

resolution digital camera and then analyzed by digital image processing (MATLAB). All the black markers were identified in the initial frame (Fig. B.4-A), and followed through the loading process. We only focused on the central part of the samples where the response was clearly more uniform and marginally affected by the boundary conditions. We first constructed several parallelograms connecting the markers in the central part of the sample (Fig. B.4-B) and monitored their evolution as a function of the applied deformation. All the markers and their corresponding parallelograms which were used in the calculations, are highlighted in green in Fig. B.4-C. For each parallelogram, local values of the engineering strain ε_{xx} and ε_{yy} were calculated from the positions of its vertices at each recorded frame t as

$$\varepsilon_{xx}(t) = \frac{(x_4(t)-x_3(t))+(x_2(t)-x_1(t))}{2|\mathrm{L}^{\circ}_{34}|} - 1, \tag{B.3}$$

$$\varepsilon_{yy}(t) = \frac{\big(y_1(t)-y_3(t)\big)+(y_2(t)-y_4(t))}{2|\mathrm{L}^{\circ}_{13}|\cos\vartheta} - 1, \tag{B.4}$$

where $(x_i,\ y_i)$ denote the coordinates of the i-th vertex of the parallelogram, $|\ \mathrm{L}^{\circ}_{34}\ |$ and $|\ \mathrm{L}^{\circ}_{13}\ |$ are the norm of the lattice vectors spanning the parallelogram in the undeformed configuration (see Fig. 4-A in the main text) and $\vartheta = \arccos \frac{\mathrm{L}^{\circ}_{34}\cdot\mathrm{L}^{\circ}_{13}}{|\mathrm{L}^{\circ}_{34}||\mathrm{L}^{\circ}_{13}|}$. The local values of the engineering strain were then used to calculate local values of the Poisson's ratio as

$$\nu(t) = -\frac{\varepsilon_{xx}(t)}{\varepsilon_{yy}(t)}, \tag{B.5}$$

and

$$\nu_{inc}(t) = -\frac{\varepsilon_{xx}(t+\Delta t) - \varepsilon_{xx}(t)}{\varepsilon_{yy}(t+\Delta t) - \varepsilon_{yy}(t)}. \tag{B.6}$$

Note that ν characterizes the lateral contraction/expansion of the structure with respect to the initial/undeformed configuration. Differently, ν_{inc} quantifies the lateral contraction/expansion with

respect to the deformed configuration induced by an increment in the applied strain $\Delta\varepsilon$ and allow us to describe the Poisson's ratio of a material that operates around a pre-deformed state. Finally, the ensemble averages $\bar{\varepsilon}_{xx} =< \varepsilon_{xx} >, \bar{\varepsilon}_{yy} =< \varepsilon_{yy} >, \bar{\nu} =< \nu >$ and , $\bar{\nu}_{inc} =< \nu_{inc} >$ for the central parallelograms under consideration were computed.

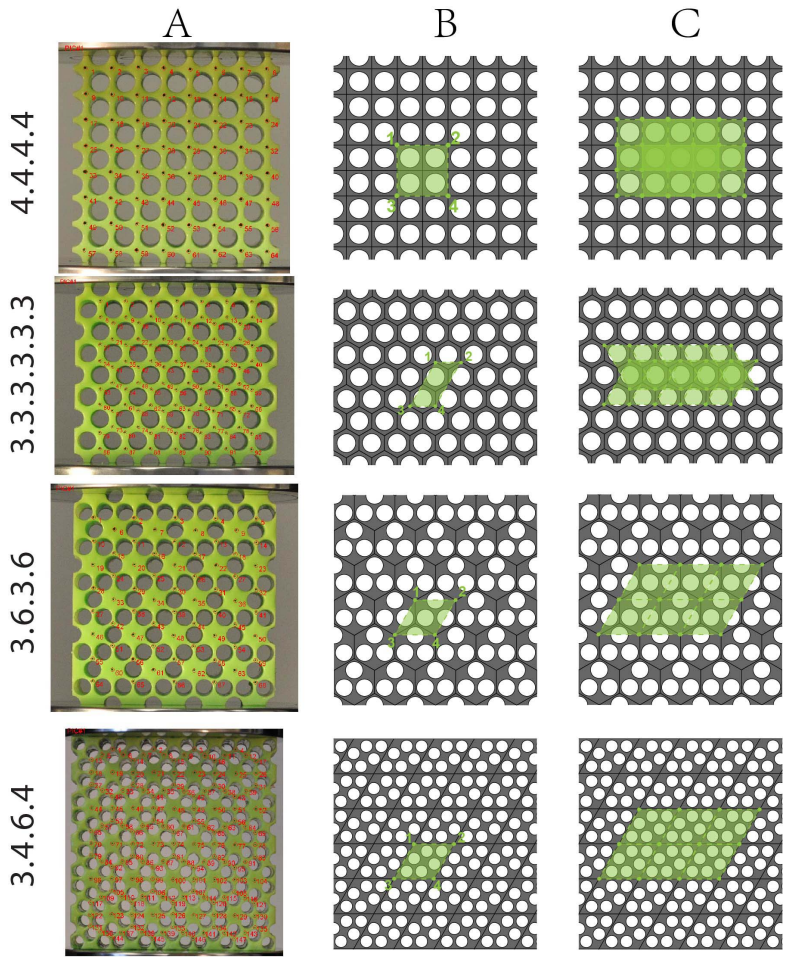

Figure B.4: Illustration of calculation of $\bar{\varepsilon}_{xx}$, $\bar{\varepsilon}_{yy}$, $\bar{\nu}$ and $\bar{\nu}_{inc}$ from experiments. (A) The samples were marked with black dots. These markers were identified with a tracking number in the initial frame and followed through the loading process. (B) Parallelograms connecting four markers in the central part of the sample were constructed and their evolution was monitored as a function of the applied deformation. (C)All the parallelograms used in the calculations are highlighted in green.

B.4 Finite-Element simulations

B.4.1 Load-displacement analysis

The commercial finite element (FE) code ABAQUS/Standard was used for simulating the post-buckling response of the finite-size porous structures. Assuming plane strain conditions, 2D FE models were constructed using ABAQUS element type *CPE6MH* with a mesh sweeping seed size of 0.5 *mm*.

After determining the pattern transformation (the lowest eigenmode) from a buckling analysis, an imperfection in the form of the most critical eigenmode was introduced into the mesh, scaled so that its magnitude was two orders of magnitude smaller than the hole size.

As the experiments were performed under displacement-controlled conditions, load-displacement analysis were then performed imposing vertical displacements at the top surface of the FE model, while fixing the horizontal degrees of freedom. All the degrees of freedom of the bottom surface were fixed.

B.4.2 Instability Analysis for Infinitely Periodic Solids

Our results demonstrate that buckling in elastic plates with carefully designed arrangement of holes may be exploited to induce either the formation of chiral patterns and/or negative Poisson's ratio. However, so far we only focused on the response of structures with $\psi \simeq 0.5$, and did not explore the effect of the void-volume-fraction ψ, which can be used to control the critical strain at buckling. Since our results clearly show that the FE simulations were able to accurately reproduce the experimental results, we investigated numerically the effect of ψ on the instability of the structured plates. For the sake of computation efficiency, we focused on infinite periodic structures, and performed all the analysis on a single unit cell using appropriate boundary conditions[168,11]. It is well

known that along the loading path periodic structures can suddenly change their periodicity due to either microscopic instability (*i.e.*, instability with wavelengths that are of the order of the size of the microstructure) or macroscopic instability (*i.e*, instability with much larger wavelengths than the size of the microstructure)[168,11]. In the following we provide a detailed description of the numerical analysis performed to detect both microscopic and macroscopic instabilities.

Infinite periodic structures In this section, we consider infinite planar periodic solids under plane strain conditions (Fig. B.5-A). The periodic solid is characterized by a unit cell spanned by the lattice vectors A_1 and A_2 in the undeformed configuration (Fig. B.5-B) and any spatial function $V(X)$ must satisfy the periodic condition

$$V(X + R) = V(X) \tag{B.7}$$

where with $R = p_1 A_1 + p_2 A_2$, p_1 and p_2 being integers. For later use, we also introduce the reciprocal lattice vectors (Fig. B.5-C)

$$B_1 = 2\pi \frac{A_2 \times A_3}{||A_1 \times A_2||} , \quad B_2 = 2\pi \frac{A_3 \times A_1}{||A_1 \times A_2||} \tag{B.8}$$

where $A_3 = (A_1 \times A_2) / ||A_1 \times A_2||$, so that $A_i \cdot B_j = 2\pi\delta_{ij}$, δ_{ij} being the Kronecker delta. Thus, the reciprocal lattice vector G can be expressed by $G = q_1 B_1 + q_2 B_2$, q_1 and q_2 being integers. Figure B.5-C illustrates the reciprocal unit spanned by the primitive reciprocal lattice vectors B_1 and B_2.

Incremental formulation The deformation of the unit cell is described by the deformation gradient

$$F = \frac{\partial x}{\partial x_0}, \tag{B.9}$$

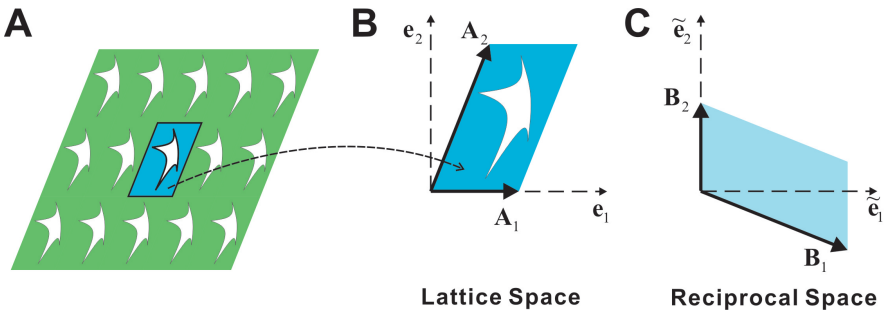

Figure B.5: (A) Schematic of infinite periodic structure in two dimensional space. (B) Primitive unit spanned by the primitive lattice vectors A_1 and A_2. Basis vectors are denoted by e_1 and e_2. (C) The corresponding reciprocal unit spanned by the primitive reciprocal lattice vectors B_1 and B_2. Basis vectors $\tilde{e}_i$ are defined by $\tilde{e}_i = \frac{2}{||A_1 \times A_2||} e_i$ for $i = 1, 2$.

mapping a point in the material from the reference position x_o to its current location x. The material is assumed to be non-linear elastic, characterized by a stored-energy function $W = W(F)$, which is defined in the reference configuration. The first Piola-Kirchhoff stress S is thus related to the deformation gradient F by

$$S = \frac{\partial W}{\partial F}. \tag{B.10}$$

In the absence of body forces, the equation of motions in the reference configuration can be written as

$$\mathrm{Div}\, S = \varrho_o \frac{D^2 x}{Dt^2}, \tag{B.11}$$

where Div represents the divergence operator in the undeformed/reference configuration, D/Dt is the material time derivative and ϱ_o denotes the reference mass density.

To investigate the stability of the periodic solid, incremental deformations superimposed upon a given state of finite deformation are considered. Denoting with $\dot{S}$ the increment of the first Piola-Kirchhoff stress, the incremental forms of the governing equations is given by

$$\mathrm{Div}\, \dot{S} = \varrho_o \frac{D^2 \dot{x}}{Dt^2}, \tag{B.12}$$

where $\dot{\mathrm{x}}$ denotes the incremental displacements. Furthermore, linearization of the constitutive equation B.10 yields

$$\dot{\mathrm{S}} = \mathbb{L} : \dot{\mathrm{F}}, \quad \text{with } \mathbb{L}_{ijkl} = \frac{\partial^2 W}{\partial F_{ij} \partial F_{kl}}, \tag{B.13}$$

where $\dot{\mathrm{F}}$ denotes the incremental deformation gradient, and $\mathbb{L}$ denotes incremental modulus (*i.e.* elasticity tensor).

To detect microscopic instabilities, we investigate the propagation of small-amplitude elastic waves defined by

$$\dot{\mathrm{x}}(\mathrm{X}, t) = \dot{\tilde{\mathrm{x}}}(\mathrm{X}) \exp(-i\omega t) \,, \tag{B.14}$$

where ω is the angular frequency of the propagating wave, and $\dot{\tilde{\mathrm{x}}}$ denotes the magnitude of the incremental displacement. It follows from B.13 that

$$\dot{\mathrm{S}}(\mathrm{X}, t) = \dot{\tilde{\mathrm{S}}}(\mathrm{X}) \exp(-i\omega t) \,, \tag{B.15}$$

so that equations B.12 become

$$\mathrm{Div}\dot{\tilde{\mathrm{S}}} = \varrho_0 \, \omega^2 \dot{\tilde{\mathrm{x}}} \,, \tag{B.16}$$

which represent the frequency-domain wave equations.

Microscopic instabilities Although microscopic (local) buckling modes may alter the initial periodicity of the solid, they can be still detected by studying the response of a single unit cell and investigating the propagation of small-amplitude waves with arbitrary wave vector $\hat{\mathrm{K}}$ superimposed on the current state of deformation [49,12]. While a real angular frequency ω corresponds to a propagating wave, a complex ω identifies a perturbation exponentially growing with time. Therefore, the transition between a stable and an unstable configuration is detected when the frequency vanishes (i.e. $\omega = 0$) and the new periodicity of the solid introduced by instability can be easily obtained by

the corresponding wave vector.

To detect the onset of microscopic instabilities, we first deform the primitive unit cell to a certain extent and then investigate the propagation of elastic waves with different wave vector

$$\hat{\mathrm{K}} = \hat{K}_1 \mathrm{B}_1 + \hat{K}_2 \mathrm{B}_2, \tag{B.17}$$

$\hat{K}_1$ and $\hat{K}_2$ being two real numbers. For each wave vector $\hat{\mathrm{K}}$, the angular frequency ω is determined by solving the frequency domain equation B.16. In this analysis quasi-periodic boundary conditions are applied, so that

$$\dot{\tilde{\mathrm{x}}}(\mathrm{X} + \hat{\mathrm{R}}) = \dot{\tilde{\mathrm{x}}}(\mathrm{X}) \exp(i\hat{\mathrm{K}} \cdot \hat{\mathrm{R}}), \tag{B.18}$$

$\hat{\mathrm{R}}$ denoting the distance in the current configuration between each pair of nodes periodically located on the boundary. Since most commercial finite-element packages do not support the complex-valued displacements introduced by B.18, following Aberg and Gudmundson[129] we split any complex-valued spatial function $\varphi(\mathrm{X})$ into a real and an imaginary part,

$$\varphi(\mathrm{X}) = \varphi(\mathrm{X})^{re} + i\varphi(\mathrm{X})^{im}. \tag{B.19}$$

The problem is then solved using two identical finite-element meshes for the unit cell, one for the real part and the other for the imaginary part, coupled by

$$\dot{\tilde{\mathrm{x}}}^{re}(\mathrm{X} + \hat{\mathrm{R}}) = \dot{\tilde{\mathrm{x}}}^{re}(\mathrm{X}) \cos(\hat{\mathrm{K}} \cdot \hat{\mathrm{R}}) - \dot{\tilde{\mathrm{x}}}^{im}(\mathrm{X}) \sin(\hat{\mathrm{K}} \cdot \hat{\mathrm{R}}), \tag{B.20}$$

$$\dot{\tilde{\mathrm{x}}}^{im}(\mathrm{X} + \hat{\mathrm{R}}) = \dot{\tilde{\mathrm{x}}}^{re}(\mathrm{X}) \sin(\hat{\mathrm{K}} \cdot \hat{\mathrm{R}}) + \dot{\tilde{\mathrm{x}}}^{im}(\mathrm{X}) \cos(\hat{\mathrm{K}} \cdot \hat{\mathrm{R}}). \tag{B.21}$$

A microscopic instability is detected at the first point along the loading path for which a wave

vector $\hat{\mathrm{K}}_{cr} = \hat{K}_{1,cr}\mathrm{B}_1 + \hat{K}_{2,cr}\mathrm{B}_2$ exist such that the corresponding angular frequency ω is zero. The instability will result in an enlarged unit cell with $n_1 \times n_2$ primitive unit cells, where

$$n_1 = \frac{1}{\check{K}_{1,cr}}, \text{ and } n_2 = \frac{1}{\check{K}_{2,cr}}. \tag{B.22}$$

Macroscopic instabilities Following Geymonat et al.[49], we investigate macroscopic instabilities by detecting loss of strong ellipticity of the overall response of the periodic structure. Specifically, macroscopic instabilities may develop whenever the condition

$$(\mathrm{m} \otimes \mathrm{M}): \quad [\mathbb{L}^H : (\mathrm{m} \otimes \mathrm{M})] > 0\,, \tag{B.23}$$

$$\text{for all} \quad \mathrm{m} \otimes \mathrm{M} \neq 0 \tag{B.24}$$

is first violated along the loading path, $\mathbb{L}^H$ denoting the homogenized incremental modulus.

In this study, 2D FE simulations on the primitive cell (see Fig. B.6) are performed to detect macroscopic instabilities applying periodic boundary conditions B.7. Operationally, after determining the principal solution, the components of $\mathbb{L}^H$ are identified by subjecting the unit cells to four independent linear perturbations of the macroscopic deformation gradient[12]. Then loss of ellipticity is examined by checking condition B.23 at every $\pi/360$ radian increment.

Results Here, FE simulations are performed to compute both microscopic and macroscopic instabilities under uniaxial compression for structures characterized by a wide range of void-volume-fractions, $\psi \in (0.4, 0.6)$. Note that higher levels of porosity would lead to structures characterized by very thin ligaments, making them fragile. On the other hand, for smaller values of porosity the response of the structures would be highly affected by the material nonlinearity.

The results of the instability analyses are summarized in Fig. B.6, where the critical strain for both macroscopic and microscopic instability is reported as a function of ψ. As expected, the critical

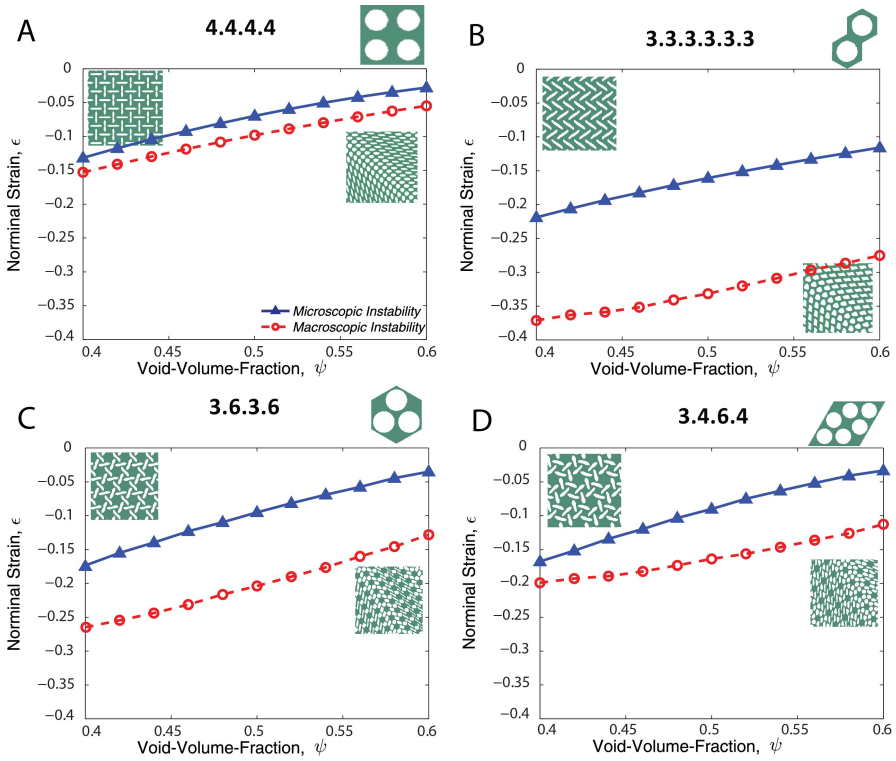

Figure B.6: Nominal strain ε at the onset of microscopic and macroscopic instabilities as a function of the void-volume-fraction ψ. The results confirm that microscopic buckling is always critical with for the considered range of ψ.

nominal strains at instability decrease for increasing values of ψ due to the reduction of the structural stiffness regardless of the types of instability. Interestingly, within the considered range of void-volume-fraction for all configurations the critical nominal strains for microscopic instability is found to be always smaller than that for macroscopic instability. Thus, these results indicate that for all configurations the folded patterns induced by microscopic buckling will emerge for a wide range of void-volume-fraction.

C

Supporting Information for Chapter 4

C.1 Fabrication

We first describe the response of the material we used to fabricate our samples, then provide a summary of all samples we fabricated for this study.

C.1.1 Material

Natural latex rubber was used to fabricate the experimental samples for this study. The material was purchased in sheet form (1/8 inch thick) from McMaster Carr. The response of the elastic sheets was tested under uniaxial tension. The experimentally measured stress-strain curve is reported in Fig. C.1 (red line), from which the initial shear modulus was measured to be $\mu_o = 0.38$ MPa.

The observed constitutive behavior is modeled as hyperelastic. Let $\mathrm{F} = \frac{\partial \mathrm{x}}{\partial \mathrm{X}}$ be the deformation gradient, mapping a material point from the reference position X to its current location x and J be its determinant, $J = \det\mathrm{F}$. For an isotropic hyperelastic material the strain energy density W can be expressed as a function of the invariants of the right Cauchy-Green tensor $\mathrm{C} = \mathrm{F}^T\mathrm{F}$ (or, alternatively, also the left Cauchy-Green tensor $\mathrm{B} = \mathrm{F}\mathrm{F}^T$). In particular, the behavior of nearly incompressible materials is effectively described by splitting the deformation locally into volume-changing ($J^{1/3}\mathrm{I}$) and distortional ($\overline{\mathrm{F}}$) components as

$$\mathrm{F} = (J^{1/3}\mathrm{I})\overline{\mathrm{F}}, \tag{C.1}$$

where I denotes the identity matrix.

The response of the latex rubber's is modeled using a Neo-Hookean hyperelastic material model, modified to include compressibility (with a high bulk modulus).

$$W = \frac{\mu_o}{2}(\bar{I}_1 - 3) + \frac{K_o}{2}(J-1)^2, \tag{C.2}$$

where μ_o and K_o are the initial shear and bulk moduli and $\bar{I}_1 = \mathrm{tr}(\overline{\mathrm{F}}^T\overline{\mathrm{F}})$. The nominal (first Piola-Kirchoff) stress is then given by

$$\mathrm{S} = \frac{\partial W}{\partial \mathrm{F}} = \left[\mu_o \mathrm{dev}\overline{\mathrm{B}} + K_o J(J-1)\right]\mathrm{F}^{-T}, \tag{C.3}$$

where $\overline{\mathrm{B}} = \overline{\mathrm{F}}\overline{\mathrm{F}}^T$ and dev is the deviatoric operator.

In all our simulations we used $K_o/\mu_o \approx 2500$. Fig. C.1 shows that the Neo-Hookean model captures the behavior well up to a nominal strain of about 0.8 which covers the majority of the strain levels studied.

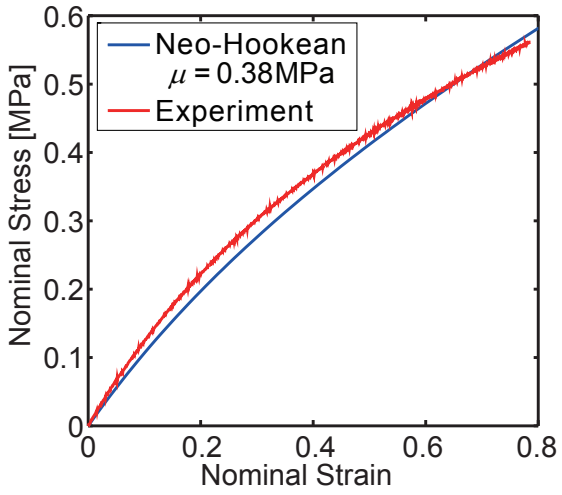

Figure C.1: Nominal stress versus nominal strain in uniaxial tension for the rubber sheet. Comparison between experimental data and model predictions.

C.1.2 Summary of fabricated samples

In Table C.1 we provide a list of all samples fabricated and tested for this study.

.

	kagome − cut	*square − cut*	*rhombi − trihexagonal − cut*	*Y − cut*	*Z − cut*
Rotational symmetry	6-fold	4-fold	6-fold	3-fold	2-fold
Axis of symmetry	0	2	0	3	0
ϑ_{min}	0°	0°	0°	0°	0°
ϑ_{max}	60°	45°	60°	30°	90°
$\Delta\vartheta$	7.5°	15°	7.5°	7.5°	15°

Table C.1: The symmetry of the cut patterns are summarized here. By taking advantage of the symmetry of the cut patterns, we greatly reduce the range of the orientation angle ϑ to explore in our experiments. N-fold rotational symmetry reduce the range of the orientation angle ϑ to $\left[0^\circ, \frac{}{N}^\circ\right]$. The mirror symmetry further reduce the range to $\left[0^\circ, \frac{}{2N}^\circ\right]$. The summarized reduced range of orientation angle ϑ to be explored listed in the above table, bounded by $[\vartheta_{min}, \vartheta_{max}]$. With in the range of orientation angle ϑ for each cut pattern, samples are fabricated every $\Delta\vartheta$.

C.2 Testing

In this section we describe in detail the procedure we used to calculate the Poisson's ratio, $\bar{\nu}$, from the experimental tests.

C.2.1 Calculation of Poisson's ratio from experiments

To quantify the deformation (and thus the Poisson's ratio, $\bar{\nu}$) taking place in the porous structures during the experiments, small marker dots (with diameter$<$ $0.5mm$) were engraved to mark the vertices of the RVEs during the cutting step, as shown in Fig. 1 in the main text. The position of the markers was recorded using a high resolution digital camera (Nikon D90 SLR) and then analyzed by digital image processing (Matlab). In particular, we focused on the behavior of 9 RVEs in the central part of the samples, where the response is more uniform and not affected by boundary effects. The markers at the corners of the chosen RVEs were identified in the initial frame, and followed through the loading process.

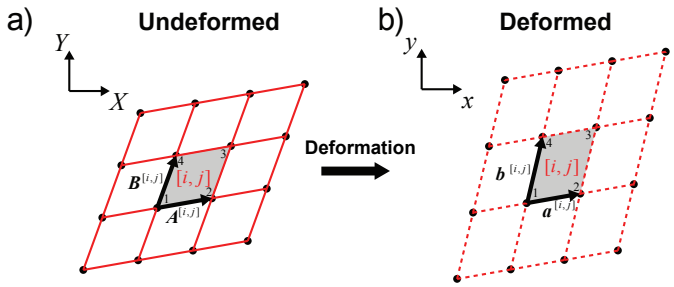

Figure C.2: Schematic diagram of the central region with 9 RVEs, which are used to calculate $\bar{\nu}$. $\mathrm{A}^{[i,j]}$ and $\mathrm{B}^{[i,j]}$ are the lattice vectors spanning the RVE in undeformed state, while $\mathrm{a}^{[i,j]}$, $\mathrm{b}^{[i,j]}$ are the lattice vectors in the deformed state.

For each RVE, local homogenized values of the engineering strain $\varepsilon_{xx}^{[i,j]}$ and $\varepsilon_{yy}^{[i,j]}$, using the fact that the lattices vectors spanning the RVE in the deformed and undeformed configuration are relat-

ed through the deformation gradient, $\mathrm{F}^{[i,j]}$, as

$$\mathrm{a}^{[i,j]} = \mathrm{F}^{[i,j]}\mathrm{A}^{[i,j]}, \qquad \mathrm{b}^{[i,j]} = \mathrm{F}^{[i,j]}\mathrm{B}^{[i,j]} \tag{C.4}$$

where

$$\mathrm{F}^{[i,j]} = \begin{pmatrix} \varepsilon_{xx}^{[i,j]} + 1 & \varepsilon_{xy}^{[i,j]} \\ \varepsilon_{yx}^{[i,j]} & \varepsilon_{yy+1}^{[i,j]} \end{pmatrix} \tag{C.5}$$

Note that the the lattice vectors in Eq. (C.4) can be easily calculated from the positions of the markers as

$$\mathrm{A}^{[i,j]} = \begin{pmatrix} A_x^{[i,j]} \\ A_y^{[i,j]} \end{pmatrix} = \frac{1}{2}\begin{pmatrix} X_2^{[i,j]} - X_1^{[i,j]} + X_3^{[i,j]} - X_4^{[i,j]} \\ Y_2^{[i,j]} - Y_1^{[i,j]} + Y_3^{[i,j]} - Y_4^{[i,j]} \end{pmatrix} \tag{C.6}$$

$$\mathrm{B}^{[i,j]} = \begin{pmatrix} B_x^{[i,j]} \\ B_y^{[i,j]} \end{pmatrix} = \frac{1}{2}\begin{pmatrix} X_4^{[i,j]} - X_1^{[i,j]} + X_3^{[i,j]} - X_2^{[i,j]} \\ Y_4^{[i,j]} - Y_1^{[i,j]} + Y_3^{[i,j]} - Y_2^{[i,j]} \end{pmatrix} \tag{C.7}$$

$$\mathrm{a}^{[i,j]} = \begin{pmatrix} a_x^{[i,j]} \\ a_y^{[i,j]} \end{pmatrix} = \frac{1}{2}\begin{pmatrix} x_2^{[i,j]} - x_1^{[i,j]} + x_3^{[i,j]} - x_4^{[i,j]} \\ y_2^{[i,j]} - y_1^{[i,j]} + y_3^{[i,j]} - y_4^{[i,j]} \end{pmatrix} \tag{C.8}$$

$$\mathrm{b}^{[i,j]} = \begin{pmatrix} b_x^{[i,j]} \\ b_y^{[i,j]} \end{pmatrix} = \frac{1}{2} \begin{pmatrix} x_4^{[i,j]} - x_1^{[i,j]} + x_3^{[i,j]} - x_2^{[i,j]} \\ y_4^{[i,j]} - y_1^{[i,j]} + y_3^{[i,j]} - y_2^{[i,j]} \end{pmatrix} \tag{C.9}$$

where $(X^{[i,j]}, Y^{[i,j]})$ and $(x^{[i,j]}, y^{[i,j]})$ denote the coordinated of the α-th vertex of the RVE in the undeformed and deformed configuration, respectively.

Finally, local homogenized values of the engineering strain for the RVE can be obtained as

$$\mathrm{F}^{[i,j]} = \begin{pmatrix} \varepsilon_{xx}^{[i,j]} + 1 & \varepsilon_{xy}^{[i,j]} \\ \varepsilon_{yx}^{[i,j]} & \varepsilon_{yy+1}^{[i,j]} \end{pmatrix} = \begin{pmatrix} a_x^{[i,j]}, & b_x^{[i,j]} \\ a_x^{[i,j]}, & b_y^{[i,j]} \end{pmatrix} \begin{pmatrix} A_x^{[i,j]}, & B_y^{[i,j]} \\ A_x^{[i,j]}, & B_y^{[i,j]} \end{pmatrix}^{-1} \tag{C.10}$$

$$= \frac{1}{A_x^{[i,j]} B_y^{[i,j]} - B_x^{[i,j]} A_y^{[i,j]}} \begin{pmatrix} a_x^{[i,j]} B_y^{[i,j]} - b_x^{[i,j]} A_y^{[i,j]}, & -a_x^{[i,j]} B_x^{[i,j]} + b_x^{[i,j]} A_x^{[i,j]} \\ a_y^{[i,j]} B_y^{[i,j]} - b_y^{[i,j]} A_y^{[i,j]}, & -a_y^{[i,j]} B_x^{[i,j]} + b_y^{[i,j]} A_x^{[i,j]} \end{pmatrix} \tag{C.11}$$

since

$$\begin{pmatrix} A_x^{[i,j]}, & B_y^{[i,j]} \\ A_x^{[i,j]}, & B_y^{[i,j]} \end{pmatrix}^{-1} = \frac{1}{A_x^{[i,j]} B_y^{[i,j]} - B_x^{[i,j]} A_y^{[i,j]}} \begin{pmatrix} B_y^{[i,j]}, & -B_x^{[i,j]} \\ -A_y^{[i,j]}, & A_x^{[i,j]} \end{pmatrix} \tag{C.12}$$

The local values of the engineering strain are then used to calculate local values of the Poisson's ratio as

$$\nu^{[i,j]} = -\frac{\varepsilon_{xx}^{[i,j]}}{\varepsilon_{yy}^{[i,j]}}, \tag{C.13}$$

and finally the ensemble average, $\bar{\nu} =< \nu^{[i,j]} >$ of the nine central RVEs under consideration is computed.

D

Supporting Information for Chapter 6

D.1 Theoretical model for buckling of a supported elastic plate

To gain more insight into the response of surface attached cellular structures, we start by investigating buckling of the individual cell edges consisting of rectangular plates of length l, height h and thickness t (see Fig. 1a) subjected to isotropic swelling.

D.1.1 Foppl-von Karman equations

For the sake of simplicity, we focus on thin plates, so that shear deformations through the thickness of the plate can be neglected, and consider a deformation that takes a point on the center-surface with coordinates $(x, y, 0)$ to its deformed state $(x + u_x(x, y), y + u_y(x, y), w(x, y))$. Assuming that the thin plate may be described as a linear elastic material with Young's modulus E, Poisson's ratio , and bending stiffness $D = Et^3/[12(1 - \nu^2)]$, then balance of forces in the plane and out of the plane directions leads to the Foppl-von Karman equations[43,174]:

$$\sigma_{ij,j} = 0, D(w_{,xxxx} + w_{,yyyy} + 2w_{,xxyy} - tw_{,ij}\sigma_{,ij}) = 0, i, j = x, y \tag{D.1}$$

where $\mathcal{A}_{,x} = \partial\mathcal{A}/\partial x$. Assuming isotropic swelling, the in-plane stresses are given by

$$\sigma_{ij} = \frac{E}{1+\nu}[\varepsilon_{ij} + \frac{\nu}{1-\nu}(\varepsilon_{xx} + \varepsilon_{yy})\delta_{ij}] - \frac{E}{1-\nu}\varepsilon_{sw}\delta_{ij} \tag{D.2}$$

where δ_{ij} is the Kronecker delta, $\varepsilon_{ij} = \frac{1}{2}(u_{i,j} + u_{j,i}) + \frac{1}{2}w_{,i}w_{,j}$ is the in-plane strain tensor and ε_{sw} denotes the strain caused by swelling of the material.

D.2 Boundary conditions

In a 2D cellular structure attached to a substrate that is very stiff and swells by a negligible amount, clamped conditions can be assumed for each individual plate at $y = 0$,

$$u_x(x, 0) = u_y(x, 0) = w(x, 0) = w_{,y}(x, 0) = 0 \tag{D.3}$$

while the condition that the boundary at y=h is free of torques and forces implies that

$$\sigma_{yy}(x,h) = \sigma_{xy}(x,h) = 0, \quad w_{,yy}(x,h) + \nu w_{,xx}(x,h) = w_{,yyy}(x,h) + (2-\nu) w_{,xxy}(x,h) = 0 \quad \text{(D.4)}$$

Finally, in a lattice where the junctions cannot move but are free to rotate for each plate the boundary conditions at $x = 0, l$ read

$$u_x(x,y) = w(x,y) = 0, w_{,xx}(x,y) + w_{,yy}(x,h) = 0, \quad at \quad x = 0, l \quad \text{(D.5)}$$

D.3 Buckling

We start by noting that Eqns. D.1-D.5 are identically satisfied when

$$u_x(x,y) = w(x,y) = 0, \quad u_y(x,y) = \varepsilon_{sw}(1+\nu)y, \quad \text{(D.6)}$$

resulting in uniform strains and stresses and zero deflection. However, this solution is not always stable and above a critical value of swelling strain, ε_{sw}^{cr}, non-planar solutions appear. To test the stability of the solution Eq. D.6, we introduce incremental deformations as follows

$$\tilde{u}_i(x,y) = u_i(x,y) + \varepsilon u_i^{(1)}(x,y), \quad \tilde{w}(x,y) = w(x,y) + \varepsilon w^{(1)}(x,y) \quad \text{(D.7)}$$

where ε is a small parameter that characterizes the size of the perturbation superimposed on the finite deformation. Introducing Eq. D.7 in Eq. D.1 and retaining only the first order terms in ε, a single non-trivial incremental equilibrium equation is obtained

$$w_{,xxxx}^{(1)} + 2w_{,xxyy}^{(1)} + w_{,yyyy}^{(1)} + \frac{Et\varepsilon_{sw}}{D} w_{,xx}^{(1)} = 0 \quad \text{(D.8)}$$

Assuming the out-of-plane deflection is of the form $w^{(1)}(x,y) = f(y)\sin\frac{m}{l}x$ (m being an integer) on substituting it into Eq. D.8 and using the boundary conditions D.3-D.5, an ordinary differential equation for $f(y)$ is obtained

$$f_{,yyyy} - \frac{2m^2\pi^2}{l^2}f_{,yy} + (\frac{m^4\pi^4}{l^4} - \frac{Et\varepsilon_{sw}}{D}\frac{m^2\pi^2}{l^2})f = 0 \tag{D.9}$$

The general solution of a fourth order differential equation like Eq. D.9 is given as,

$$f(y) = C_1 e^{-\quad y} + C_2 e^{\quad y} + C_3\cos(\beta y) + C_4\sin(\beta y) \tag{D.10}$$

where α and β are as following,

$$\alpha = \sqrt{\frac{m^2\pi^2}{l^2} + \sqrt{\frac{m^2\pi^2 Et\varepsilon_{sw}}{Dl^2}}}, \quad \beta = \sqrt{-\frac{m^2\pi^2}{l^2} + \sqrt{\frac{m^2\pi^2 Et\varepsilon_{sw}}{Dl^2}}} \tag{D.11}$$

The coefficients C_1, C_2, C_3 and C_4 in Eq. D.10 are determined by imposing the boundary conditions D.3-D.5. More specifically, the boundary conditions D.3 are satisfied if

$$C_1 = \frac{C_4\beta - C_3\alpha}{2\alpha}, \quad C_2 = -\frac{C_3\alpha + C_4\beta}{2\alpha} \tag{D.12}$$

and the function $f(y)$ can be represented in the form

$$f(y) = C_3\left[\cos(y\beta) - \cosh(y\alpha)\right] + C_4\left[\sin(y\beta) - \frac{\beta}{\alpha}\sinh(y\alpha)\right] \tag{D.13}$$

Substituting the above expression in Eq. D.4, we get two linear homogeneous equations in terms of C_3 and C_4. The critical value of swelling strain, ε_{sw}^{cr}, is determined by equating to zero the determinant of these equations.

We solve this boundary value problem numerically and study the normalized critical strain $\frac{h^2\varepsilon_{sw}^{cr}}{t^2}$

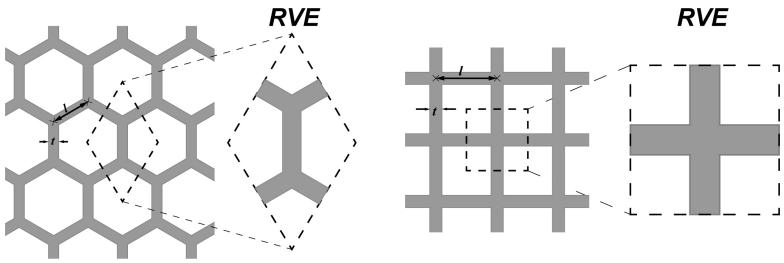

Figure D.1: Top views of hexagonal and square cellular structures. Notice that l is defined as the center-to-center distance between adjacent vertices. The magnified portions of the structure show the representative volume elements (RVE) of the corresponding architecture.

and corresponding buckling modes as a function of the plate aspect ratio l/h, as shown in Fig. 1b. It is interesting to observe that higher buckling modes (i.e. $m > 1$) can be achieved for increasing values of l/h. By contrast, we notice that for a plate with free edges both at $y = 0$ and $y = h$ only modes with half wavelength (i.e. $m = 1$) are possible.

D.4 Numerical simulations of buckling for supported cellular structures

Since our analytical model is based on the theory for thin elastic plates, to fully account for the effect of thickness, we further investigated the buckling of surface-attached lattice structures using non-linear finite element (FE) analyses. The FE calculations were conducted within the nonlinear code ABAQUS/Standard, version 6.8-2. In the numerical analyses, buckling of cellular structures of infinite planar extent perfectly bonded to a rigid substrate was investigated and for that sake of computational efficiency, the analyses were conducted on representative volume elements (RVEs) (see Fig. D.1).

The instability of the structures was investigated conducting a Bloch wave analysis[10,169], a staple of physics long used to examine electronic, photonic and phononic band structures in periodic lattices. Although instabilities may alter the initial periodicity of the solid, they can be still detected investigating the response of just one unit cell of the material introducing boundary conditions pro-

vided by Bloch theory. While a real natural frequency corresponds to a propagating wave, a complex natural frequency identifies a perturbation exponentially growing with time. Therefore, the transition between a stable and an unstable configuration is detected when the frequency vanishes and the new periodicity after instability is provided by the corresponding Bloch wave vector. Here, the finite-element method was used to perform the Bloch wave analysis[10].

Three-dimensional models corresponding to hexagonal and square lattices characterized by (l/h=2, t/h=0.37) and ($l/h = 3.17$, $t/h = 0.40$) were constructed using 20-nodes, quadratic elements (ABAQUS element type C3D20). The accuracy of each mesh was ascertained through a mesh refinement study. In the analysis the bottom surface of the structures was considered to be perfectly bonded to a rigid substrate, while the top surface was free. Moreover, a series of constraint equations were applied to the lateral surfaces of the RVE providing Floquet quasi-periodic boundary conditions. The material was modeled as elastic nearly incompressible Neo-Hookean material and swelling was used to induce buckling.

The results for the four structures (i.e. square and hexagonal lattices with ($l/h = 2$, $t/h = 0.37$) and ($l/h = 3.17$, $t/h = 0.40$)) investigated in this study are reported in Figure D.2. The same buckling mode predicted by the analytical model based on Foppl-von Karman equations is observed in the structures. More specifically, for $l/h = 2$ and $t/h = 0.37$ buckling induces the formation of an achiral pattern for both the hexagonal and square architecture. Differently, a chiral pattern is induced by mechanical instabilities when $l/h = 3.17$ and $t/h = 0.40$. Finally, we note that for a square lattice with $l/h = 2$ and $t/h = 0.37$ at the onset of instability the initial periodicity is broken, leading to an enlarged RVE with 2×2 original RVEs.

The numerical simulations thus confirm that by simply controlling the aspect ratio of supported-cellular structure in initial honeycomb structure either achiral or chiral configurations can be formed.

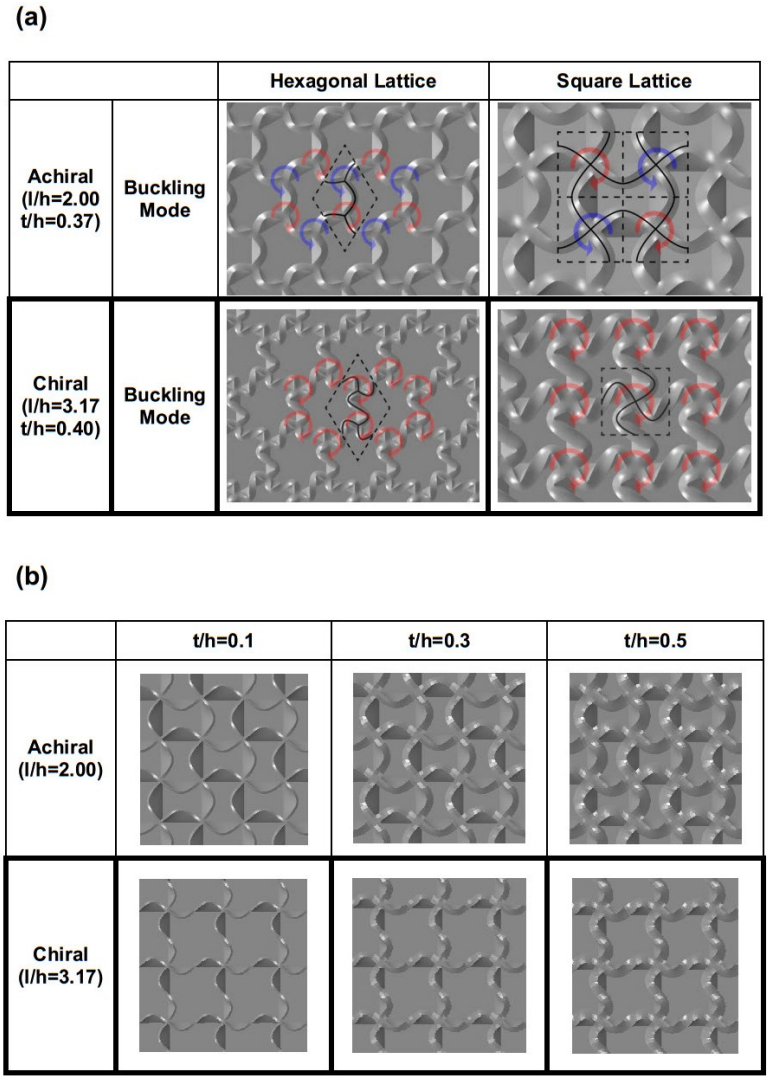

Figure D.2: (a) Critical buckling modes predicted by numerical analysis. Buckling modes predicted by the Bloch wave analysis for supported hexagonal and square lattices with ($l/h = 2, t/h = 0.37$) and ($l/h = 3.17$, $t/h = 0.40$). The handedness of adjacent vertices has been highlight with red (right-handed) or blue (left-handed) arrows. The top views of buckled patterns are outlined by solid curves on the top surface of the structure to facilitate visualization. (b) Critical buckling modes predicted by numerical analysis for supported square lattices with $t/h = 0.1, 0.3$ and 0.5. The buckling mode is found not to be affected by t/h. This confirms that buckling-induces pattern of supported cellular structures is dictated by the aspect ratio l/h.

D.5 Experimental verification of the stability diagram

Having ascertained the critical design parameters, to verify the validity of our analytical model we fabricated surface-attached cellular structures with aspect ratio l/h that swept through different domains in the stability diagram. More specifically, we started with macro-scale honeycomb structures ($l = 5mm$) comprising 19 hexagons and made from silicone rubber (see Fabrication section for details). We fabricated 13 samples with fixed dimension in length and thickness ($l = 5\ mm$, $t = 0.9\ mm$) and variable h, such that $l/h = 1, 1.33, ., 4.66, 5$, as indicated by markers spanning across the three regime in Fig. D.3a. Immersing the architecture in hexane swelled the polymer, and within a few seconds the initially straight cell walls buckled to yield either chiral, achiral or mixed patterns (Fig. D.3b), as predicted by the stability diagram (Fig. 6.1). This set of experimental results clearly confirms the validity of our analytical model.

D.6 Fabrication

D.6.1 Macro-scale structures.

Macro-scale ($l = 5\ mm$) surface-attached hexagonal and square cellular structures were fabricated by making negative molds using a 3D printer (Connex 500 available from Objet, Ltd.) and replicating positive structures with a silicone rubber (Elite Double 32 available from Zhermack). Before replication, a releasing agent (Easy Release 200 available from Smooth-On, Inc.) was sprayed on to the molds for easy separation. The structures were attached to rigid back plates.

D.6.2 Micro-scale structures.

Two micro-scale different surface-attached hexagonal structures were fabricated for this study, with aspect ratios that corresponded to both achiral ($l/h = 2, t/h = 0.37$) and chiral ($l/h = 3.17$,

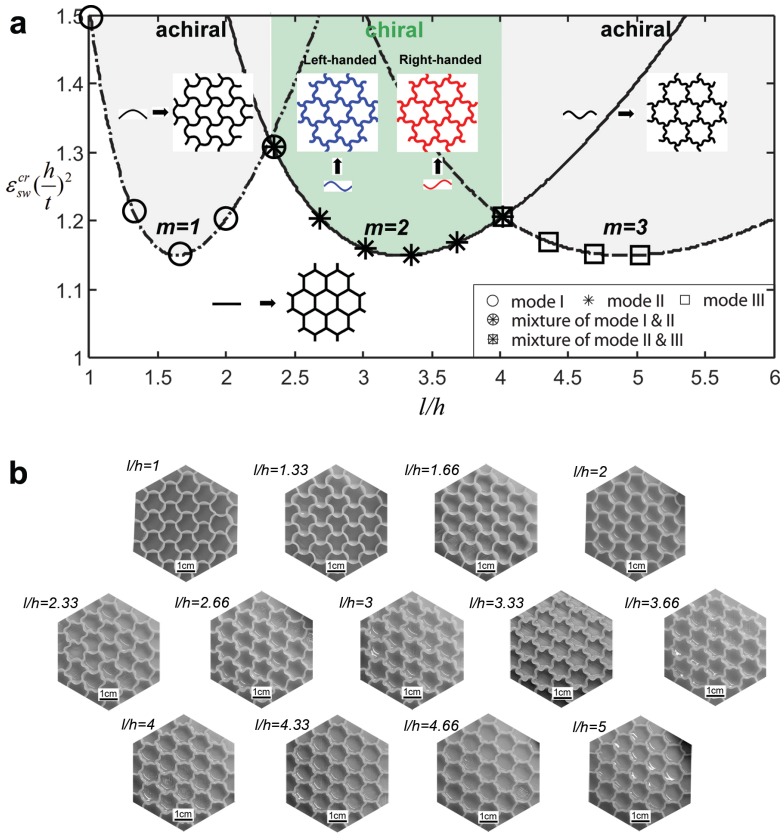

Figure D.3: Experimental verification of the stability diagram. (a) To verify the validity of our analytical model, we fabricated macroscale honeycomb structures ($l = 5\,mm, t = 0.9\,mm, h = 1 - 5\,mm$) made from silicone rubber with different aspect ratio l/h, as indicated by the markers in the stability diagram. (b) Buckling patterns observed in samples with different l/h. Modes characterized by $m = 1$, $m = 2$ and $m = 3$ are observed, exactly as predicted by the analytical model. Moreover, mixtures of modes with $m = 1 - 2$ and $m = 2 - 3$ are found for geometries lying on the boundary of adjacent regimes (Figure S3(a)).

$t/h = 0.40$) structures. The honeycomb structures yielding an achiral buckled pattern comprise individual plates with a thickness of 3.7 m, a length of 20 m, and a height of 10 m. The prochiral structures consist of an array of plates with thickness of 2.5 m, a length of 20 m, and a height of 6.3 m. The different aspect ratio honeycomb structures used for this study were first fabricated in $< 100 >$ Si wafers. The wafers were vapor primed with Hexamethyldisilazane (HMDS) to improve photo resist adhesion. SPR700 was used as a resist. Nikon 5 i-line stepper was used to expose the coated wafers followed by post exposure bake and resist development using Microposit MF CD26. Descumming was performed prior to Bosch advanced silicon etch6 in an STS deep reactive ion etching (DRIE) tool. C4F8 and SF6 chemistry was used for Si etching. Veeco profilometers and cross sectional SEM (Zeiss) was used to characterize and optimize exposure conditions etch rate and etch profile. The Si wafers were given a final overcoat of C4F8 to aid in the replication process. Scalloping on the plates of honeycomb structures is the result of the Bosch etch process[104,5] and is also visible in the polymer replicas. Replicas of the silicon masters were fabricated using soft lithography-based methods with commercially available UV-curable epoxy (UVO-114 from Epoxy Technology, Billerica, MA) as described in a previous paper[125].

D.7 Buckling-induced pattern formation through swelling

Swelling was used to trigger instability in the considered supported cellular structures. Buckling occurred due to compressive stresses arising from the geometric constraint that suppresses swelling near the rigid substrate where the structure is clamped.

D.7.1 Macro-scale structures.

Instability of fabricated structures was induced by swelling the structures with hexane. We started by rapidly immersing the samples in hexane. We observed the formation of buckled pattern-

s in excellent agreement with the analytical predictions, but characterized by multiple domains that evolved from different nucleation sites. To make defect-free samples, we carefully controlled nucleation and propagation of the pattern. A plastic tube (Intramedic polyethylene tubing with ID=0.38 *mm*, OD=1.09 *mm* available from Becton, Dickinson and Company) was used to gradually wet the samples starting from a single location and the solvent was introduced through a syringe pump (PHD 2000 available from Harvard Apparatus) at a flow rate of $0.1 - 0.4mL/min$. The resulting patterns were recorded using Nikon D90 digital SLR camera.

D.7.2 Micro-scale structures.

Buckling was induced by swelling the structures with *N*-methyl-2-pyrrolidone (NMP) (available from Sigma Aldrich). We started by rapidly immersing the structures in the solvent, leading to the formation of multiple domains. To make defect-free samples, we floated them on the solvent so that the structure swelled from one side by wetting. The resulting patterns were recorded by optical microscope (Leica DMRX connected to a QImaging Evolution VF cooled color CCD camera).

D.8 Buckling-induced pattern formation through compression

We demonstrated that the pattern formation can be extended to different stimuli, by inducing buckling through mechanical loading. We performed compression experiment on microscale honeycomb structures made of UV curable epoxy and comprising an array of plates with a thickness of 3.7 m, a length of 20 m, and a height of 10 m ($l/h = 2$, $t/h = 0.37$). Figure D.4 shows the compressed (left) vs. uncompressed (right) areas of a single sample. An exceptionally uniform achiral buckled pattern is observed in the compressed area.

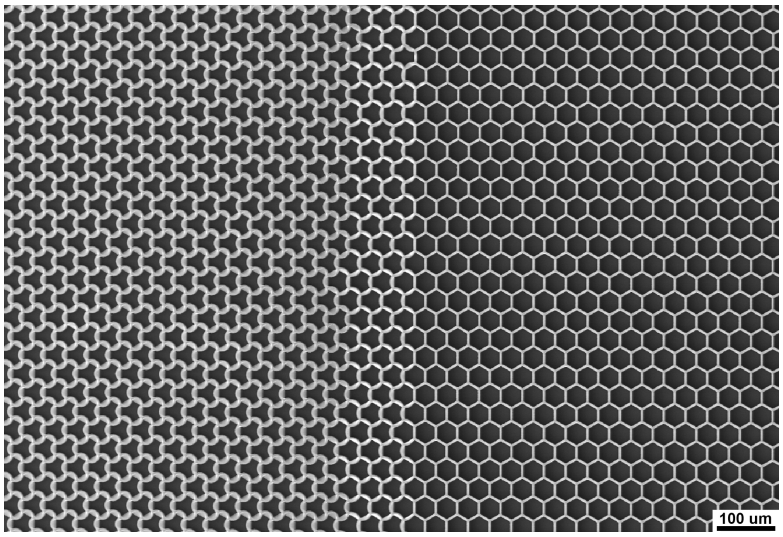

Figure D.4: Scanning electron microscope (SEM) image of buckled patterns formed by compression of surface-attached honeycombs. Compression was applied to the left half of a micro-scale honeycomb structure (l/h=2, t/h=0.37). The compressed region shows a uniform, 1 st mode buckled pattern.

E

Supporting Information for Chapter 5

E.1 Periodic networks of rigid polygons

To identify periodic porous elastic structures with multiple folding mechanisms, we investigate the flexibility of periodic planar networks built from rigid corner-connected (hinged) polygons, which can rotate freely around the hinges. First, we show that a network of connected squares has a single folding mechanism. Then, as previously demonstrated by Guest *et al.*[76], we show that in planar

networks built from equilateral triangles the number of folding mechanisms grows with the size of unit cell.

E.1.1 Network of rigid squares

We start by investigating the folding mechanisms of a network of connected squares. To demonstrate that this structure has a single folding mechanism, we consider unit cells of different sizes and determine their folding mechanisms by enforcing geometric compatibility. We first focus on a unit cell consisting of two connected squares and show that in this case no folding mechanism is supported by the network. Then, we consider a unit cell comprising four squares and show that in this case only one folding mechanism exists. Our simple analysis can be extended to larger unit cells, indicating that only one single folding mechanism is possible for this network (for the sake of brevity here we do not report results for unit cells with more than four squares).

Unit cell with two squares

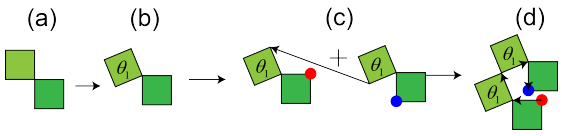

Figure E.1: Geometrical compatibility of a unit cell with two squares. ϑ_1 indicates the rotation angle of the light-green square. Geometrical compatibility between adjacent unit cells requires the red and blue markers overlap.

Here we consider a unit cell consisting of two corner-connected squares with edge L_0 (see Fig. E.1-a). If one of the two squares rotate by an angle ϑ_1, geometrical compatibility requires that the red and blue circular markers in Fig. E.1-c overlap, yielding

$$L_0 \cos(\pi) + L_0 \cos\left(\frac{\pi}{2} + \vartheta_1\right) + L_0 \cos(0 + \vartheta_1) + L_0 \cos(-\frac{\pi}{2}) = 0, \tag{E.1}$$

$$L_0 \sin(\pi) + L_0 \sin(\frac{\pi}{2} + \vartheta_1) + L_0 \sin(0 + \vartheta_1) + L_0 \sin(-\frac{\pi}{2}) = 0.$$

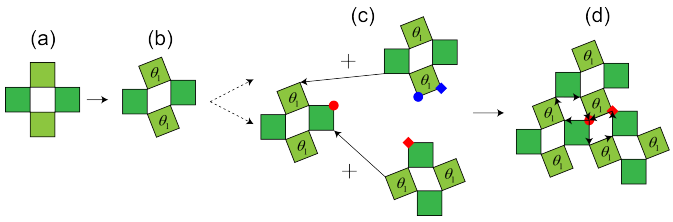

Figure E.2: Geometrical compatibility of a unit cell with four squares. ϑ_1 indicates the rotation angle of the light-green squares. Geometrical compatibility between adjacent unit cells requires that the red and blue markers overlap in pairs (i.e. red round/diamond marker overlap with blue round/diamond markers).

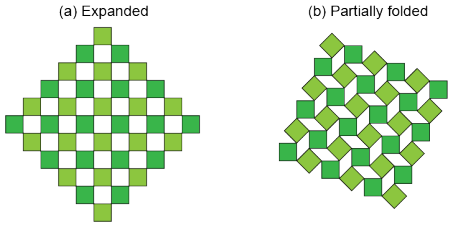

Figure E.3: The folding mechanism for a network of rigid squares. (a) Expanded configuration. (b) Partially folded configuration.

It is easy to show that Eqs. (E.1) are both satisfied only when $\vartheta_1 = 0$, indicating that no folding mechanism is supported by the network when a unit cell consisting of two squares is considered.

Unit cell with four squares

Next, we focus on a unit cell consisting of four corner-connected squares with edge L_0 (see Fig. E.2-a). First, we notice that compatibility within the unit cell requires that opposite squares undergo the same rotation. Therefore, without loss of generality, we assume that two of the four squares rotate by an angle ϑ_1 and two do not rotate (see Fig. E.2-b). It is easy to see that in this case compatibility between adjacent unit cells is also satisfied (Fig. E.2-c and d), indicating that the folding mechanism shown in Fig. E.2-d is supported by the structure. Although, for the sake of brevity, here we do not include analysis for unit cells of larger size, these are straightforward. Such analysis indicate that this folding mechanism is the only one supported by the structure, resulting in a pattern of rhombic, elongated holes with the major axis perpendicular to each other (see Fig. E.3).

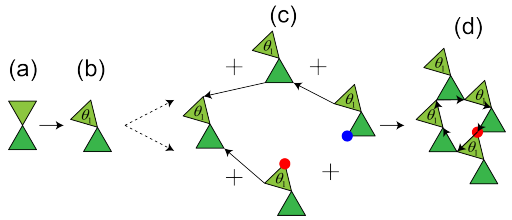

Figure E.4: Geometrical compatibility of a unit cell with two triangles. ϑ_1 indicates the rotation angle of the light-green triangle. Geometrical compatibility between adjacent unit cells requires the red and blue markers overlap.

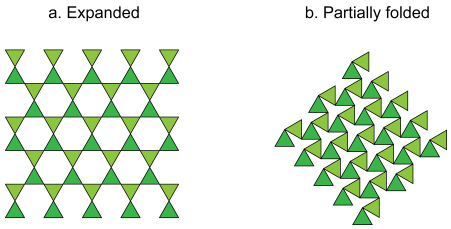

Figure E.5: The folding mechanism of network of rigid triangles with a unit cell with two triangles. (a) Expanded configuration. (b) Partially folded configuration.

E.1.2 Network of rigid triangles

We now proceed to investigate the folding mechanisms of a network of connected triangles arranged to form a kagome structure. First, we consider a unit cell consisting of only two triangles, which is the smallest unit cell for the network, and identify one folding mechanism for the system. Then, we focus on a larger unit cell comprising four triangles and find an additional folding mechanism. Finally, we establish a simple rule that enables us to easily construct the folding mechanisms for unit cells of arbitrary size.

Unit cell with two triangles

Here we consider a unit cell consisting of two corner-connected triangles with edge L_0 (see Fig. E.4-a). If one of the two triangles rotates by an angle ϑ_1 (see Fig. E.4-b), geometrical compatibility requires that the red and blue circular markers in Fig. E.4-c overlap, yielding

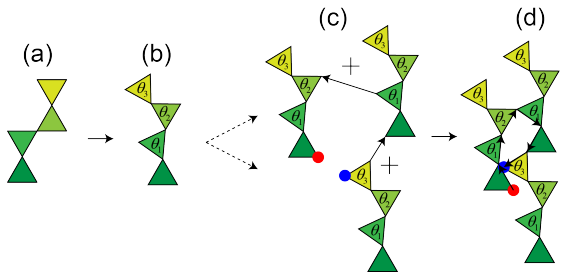

Figure E.6: Geometrical compatibility of a unit cell with four triangles. ϑ_1, ϑ_2, and ϑ_3 indicates the rotation of the green, light-green and yellow triangles, respectively. Geometrical constraints between adjacent unit cells require the red and blue markers overlap.

$$L_o \cos(\frac{2\pi}{3}) + L_o \cos(\frac{\pi}{3} + \vartheta_1) + L_o \cos(o) + L_o \cos(-\frac{\pi}{3} \tag{E.2}$$

$$+\vartheta_1) + L_o \cos(-\frac{2\pi}{3}) + L_o \cos(-\pi + \vartheta_1) = o, \tag{E.3}$$

$$L_o \sin(\frac{2\pi}{3}) + L_o \sin(\frac{\pi}{3} + \vartheta_1) + L_o \sin(o) + L_o \sin(-\frac{\pi}{3}$$

$$+\vartheta_1) + L_o \sin(-\frac{2\pi}{3}) + L_o \sin(-\pi + \vartheta_1) = o. \tag{E.4}$$

It is easy to see that Eqs. (E.2) are automatically satisfied for any choice of $o < \vartheta_1 < 2\,\pi/3$, indicating that the folding mechanism shown in Fig. E.4-d is supported by the structure. Such folding mechanism results in the formation of a pattern where all hexagonal holes progressively reduce to 3 point star-like shapes (see Fig. E.5).

Unit cell with four triangles

Next, we focus on a unit cell comprising of four corner-connected triangles, as shown in Fig. E.6-a. Without loss of generality we assume that one triangle does not rotate, while the other three triangles rotate by angles ϑ_1, ϑ_2 and ϑ_3 (Fig. E.6-b). Geometrical compatibility between adjacent unit cells

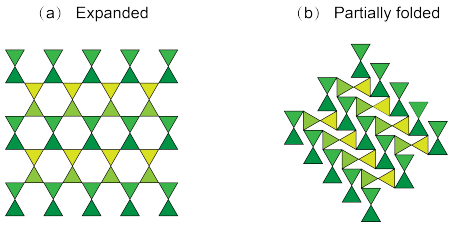

Figure E.7: The additional folding mechanism of network of rigid triangles with a unit cell of four triangles. (a) Expanded configuration. (b) Partially folded configuration.

requires

$$L_0 \cos(\frac{2\pi}{3}) + L_0 \cos(\frac{\pi}{3} + \vartheta_1) + L_0 \cos(\vartheta_2) + L_0 \cos(-\frac{\pi}{3} \tag{E.5}$$

$$+\vartheta_1) + L_0 \cos(-\frac{2\pi}{3}) + L_0 \cos(-\pi + \vartheta_3) = 0, \tag{E.6}$$

$$L_0 \sin(\frac{2\pi}{3}) + L_0 \sin(\frac{\pi}{3} + \vartheta_1) + L_0 \sin(\vartheta_2) + L_0 \sin(-\frac{\pi}{3}$$

$$+\vartheta_1) + L_0 \sin(-\frac{2\pi}{3}) + L_0 \sin(-\pi + \vartheta_3) = 0, \tag{E.7}$$

which can be easily simplified to

$$-1 + \cos(\vartheta_1) + \cos(\vartheta_2) - \cos(\vartheta_3) = 0, \tag{E.8}$$

$$\sin(\vartheta_1) + \sin(\vartheta_2) - \sin(\vartheta_3) = 0.$$

Eqs. (E.8) are automatically satisfied for

$$\begin{cases} \vartheta_1 = \vartheta_3, \\ \vartheta_2 = 0, \end{cases} \tag{E.9}$$

and

$$\begin{cases} \vartheta_1 = 0, \\ \vartheta_2 = \vartheta_3. \end{cases} \tag{E.10}$$

The first solution (Eqs. (E.9)) results in the formation of the same pattern found when investigating the unit cell consisting of two triangles, as shown in Fig. E.5. The second solution (Eqs. (E.10)) is associated to the formation of a pattern of sheared voids where the shear direction alternates back and forth from row to row (see Fig. E.7).

E.1.3 Folding mechanisms for larger unit cells

Additional folding mechanisms for the kagome network can be identified by repeating similar calculations as reported above for larger unit cells. Furthermore, the construction of additional folding mechanisms is greatly facilitated by the observation that geometric compatibility requires the triangles to rotate by $\pm\alpha$ (i.e. by the same amount either in clockwise or anti-clockwise direction, see magenta and cyan triangles in Fig. E.8) or not to rotate at all (i.e. $\alpha = 0$, see yellow triangles in Fig. E.8). Although here, for the sake of brevity, we do not report the calculations to identify the folding mechanisms for larger unit cells, in Fig. E.8 we show several of them.

E.2 Finite Element Simulations

E.2.1 Stability analysis: chiral pattern as linear combination of the X- and Z-mode

As shown in Fig. 3 of the main text our stability analysis reveals that for all considered values of ϑ (i.e. $\pi < \vartheta < 3\pi/2$), the X- and Z-modes are always triggered either as first or second mode. In particular, for $\pi < \vartheta < 5\pi/4$ the critical loading parameter λ_{cr} associated to the X-mode is found to be always lower than that associated to the Z-mode, so that the X-mode is expected to emerge

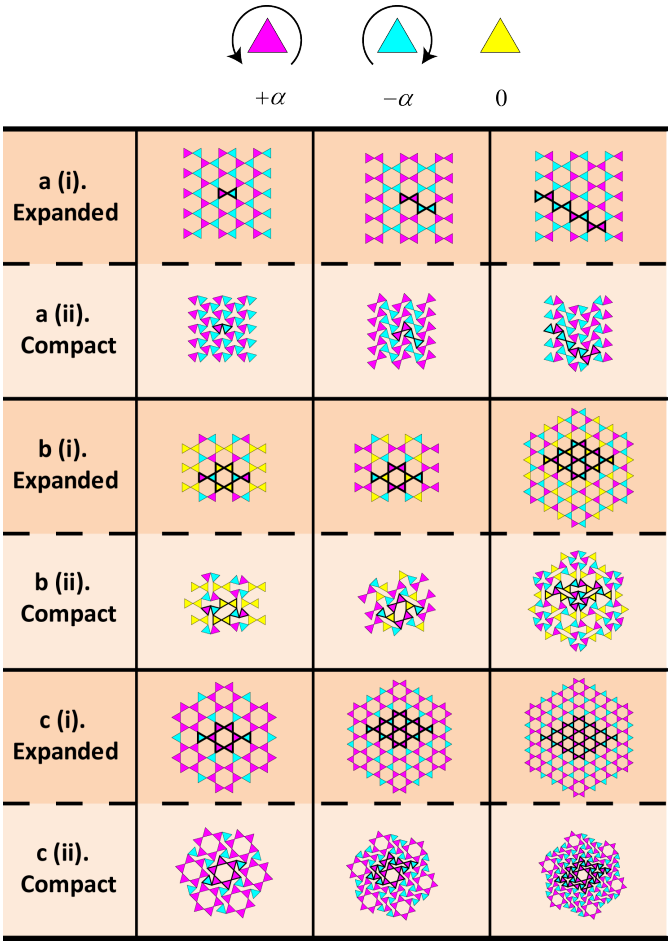

Figure E.8: Nine folding mechanisms for a triangular network of connected triangles. The unit cell for each folding mechanism is outlined in black.

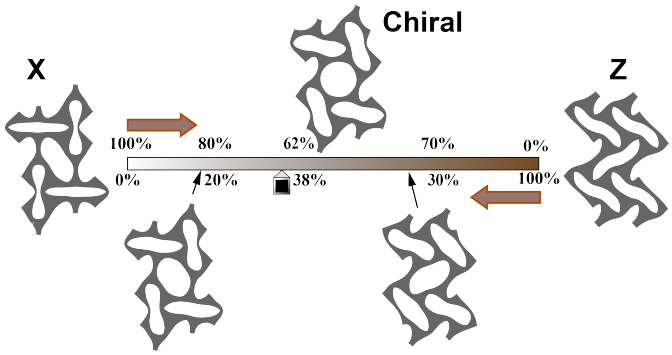

Figure E.9: Schematic illustration of superimposition of X- and Z-modes. The chiral mode appears by a linear combination of the X- and Z- modes.

during deformation for this range of loading path angles. By contrast, the Z-mode is expected to be triggered when $5\pi/4 < \vartheta < 3\pi/2$, since in this case the lowest critical loading parameter is that corresponding to the Z-mode. Interestingly, for $\vartheta = 5\pi/4$ both the X- and Z-modes are characterized by the same critical loading parameter, so that any linear combination of the two modes is a valid eigenmode.

In Fig. E.9 we report both the X- and Z-modes and three linear combinations of them. Interestingly, one of these linear combinations corresponds to a chiral pattern comprising six highly deformed voids surrounding an undeformed one, resembling that reported in Fig. 1-e of the main text for the kagome network.

Next, guided by the stability analysis we conduct a post-buckling analysis on a RVE consisting of 2×2 unit cells by applying periodic boundary conditions and introducing a geometrical imperfection with the form of the first two eigenmodes (i.e. a linear combination of the X- and Z- modes). As shown in Fig. 4-c of the main text, for $\vartheta = 5\pi/4$ a chiral pattern resembling that reported in Fig. E.9 emerges.

E.2.2 Elastic wave propagation analysis

In order to obtain the dispersion relation for a triangular array of circular holes in an elastomeric matrix and to investigate the effect of the applied deformation on the propagation of elastic waves, frequency domain wave propagation analyses are performed on both the undeformed and deformed configurations generated by the post-buckling analysis using the finite element method[11,175]. To work with the complex-valued displacements of the Bloch-wave calculation within the confines of a commercial code, all fields are split into real and imaginary parts[11]. In this way the equilibrium equations split into two sets of uncoupled equations for the real and imaginary parts. Thus, the eigenfrequency ω can be computed for any wave vector k using two identical finite-element meshes for the RVE, one for the real part and the other for the imaginary part, and coupling them by Bloch-type displacement boundary conditions.

The phononic bandgaps are identified by checking all eigenfrequency $\omega(\mathrm{k})$ for all k vectors in the irreducible Brillouin zone. The bandgaps (i.e. range in frequencies for which the propagation of waves is barred) are given by the frequency ranges within which no $\omega(\mathrm{k})$ exists. Numerically, a discrete set of k vectors in the irreducible Brillouin zone need to be chosen in the analysis. For the simulations presented in this paper, five-segment wave-vector paths $\mathrm{G}-\mathrm{X}-\mathrm{M}-\mathrm{G}-\mathrm{Y}-\mathrm{M}$ defining the perimeter and the diagonal of the irreducible Brillouin zone are considered and the eigenfrequencies $\omega(\mathrm{k})$ are calculated for twenty points uniformly distributed on each line segment.

Note that all the calculations are performed on an enlarged unit cell (comprising 2×2 unit cells) with size dictated by the new periodicity introduced by buckling, as shown in Fig. E.10-a. Such RVE is spanned by the lattice vectors $\mathrm{a}_1 = [a, 0]$ and $\mathrm{a}_2 = [0, \sqrt{3}a]$, where a is the center-to-center distance between adjacent holes and can be expressed as a function of the porosity ψ_0 and hole di-

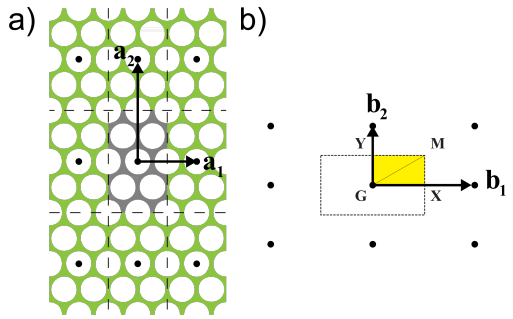

Figure E.10: (a) Schematic of the structure in the undeformed configuration. The considered RVE spanned by the lattice vectors a_1 and a_2 is shown in grey. (b) The corresponding Brillouin zone in reciprocal space is spanned by the vectors b_1 and b_2.

ameter D_o as $a = \left(\frac{\sqrt{3}}{6}\frac{D_o^2}{o}\right)^{1/2}$. Therefore the reciprocal space is defined by,

$$b_1 = 2\pi\frac{a_2 \times z}{\| z \|^2}, \quad b_2 = 2\pi\frac{z \times a_1}{\| z \|^2}, \tag{E.11}$$

where $z = a_1 \times a_2$.

E.3 Experiments

E.3.1 Biaxial compression tests

To verify findings from numerical models that show multiple folding mechanisms depending on the loading directions, we did experiments using a custom set-up that can control the loading in two orthogonal directions independently providing the capability to test the sample in arbitrary biaxial loading conditions. (see Fig. E.11-a)

Biaxial compression tests were conducted on two perpendicularly placed linear quasi-static stages (model SLP-35 from Nippon Pulse America Inc.) in a displacement-controlled manner. The stages were configured to realize an optimal spatial resolution of 1 μm. The fine movement of the stages was coordinated through a LabView program and the ratio between the engineering strains in two

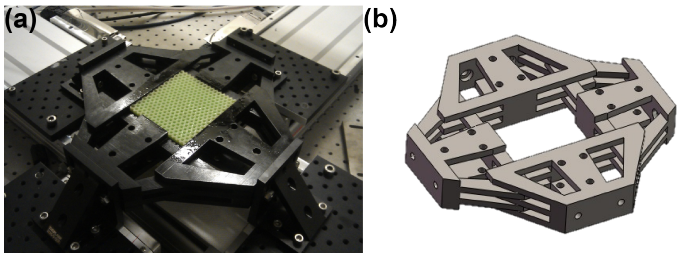

Figure E.11: (a) Picture of the biaxial setup used for our compression test. (b) Sketch of the biaxial compression fixture whused for our compression experiments.

directions was kept constant during the biaxial test. The specimens were compressed through a set of customary compression fixtures, which were designed to ensure them not to collide during the compression tests (see Fig. E.11-b). The overall fixture set consisted of two pairs of parts with each pair for the compressive movement in one of two orthogonal directions. The specimen was not clamped to the fixtures because the friction between the specimen and fixture surface was enough to hold the specimen. Lubricant was used on surfaces of fixtures to reduce friction and boundary effects. The compression tests were performed at the cross-head velocity of $5mm/min$ until the structure was densified. During the test, a Nikon D90 SLR camera was used to capture the resulting patterns from the sample.

E.3.2 Wave propagation tests

To investigate the effect of different instability-induced patterns on the propagation of small amplitude elastic waves in the periodic structure, we conducted wave propagation tests for the the udeformed sample and for three deformed configurations obtained by different loading path angles $\vartheta = \pi, 5\pi/4$ and $3\pi/2$, but under the same areal strain, $\varepsilon_{Area} = -0.24$.

The overall set-up for the tests is shown in Fig. E.12. All components were placed on top of a passive optical table (model PTM11104 from Thorlabs) to isolate from ambient vibrations. First, a Gaussian white noise was generated from the amplifier and was used to control the shaker (mod-

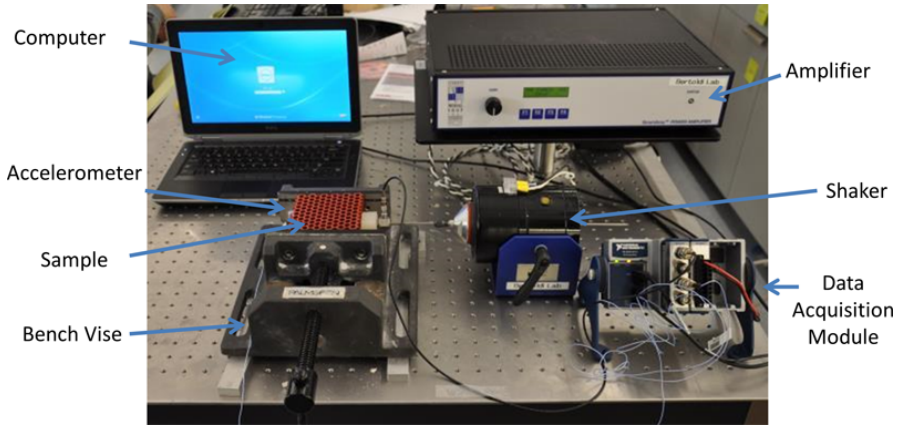

Figure E.12: Picture of the set-up used for our wave propagation tests.

el K2025E013 from The Modal Shop). The dynamic response was recorded using a miniature accelerometer (352C22 PCB Piezotronics) attached to the far end of the sample. To apply a uniform in-plane wave, we used a PTFE (Polytetrafluoroethylene) block to increase the contact area between the shaker and the sample. Furthermore, to effectively transmit the vibration from the shaker to the sample, all contact interfaces (shaker/PTFE block, PTFE block/sample, sample/accelerometer) were temporarily super-glued.

The input force signals were detected at the shaker (input) from a load cell. The acceleration at the far end of the sample (output) was detected using an ultra-light piezo-electric accelerometer. The detected signal was acquired through a data acquisition module and further processed and recorded by a computer. The transmittance was computed as the ratio between the output acceleration signal recorded at the far end of the sample and the input force signal from the load cell (i.e., $\|\mathcal{A}(\omega)/F(\omega)\|$).

A bench vise was used to apply the desired value of deformation to the sample (see Fig. E.13). In Fig. E.13-b and -c we show the sample deformed into the in X-mode and Z-mode, respectively. In these cases, the shaker was directly connected to one end of the sample. Differently, when the system was deformed equibiaxially, four clamps are needed, so that all four edges of the sample were in

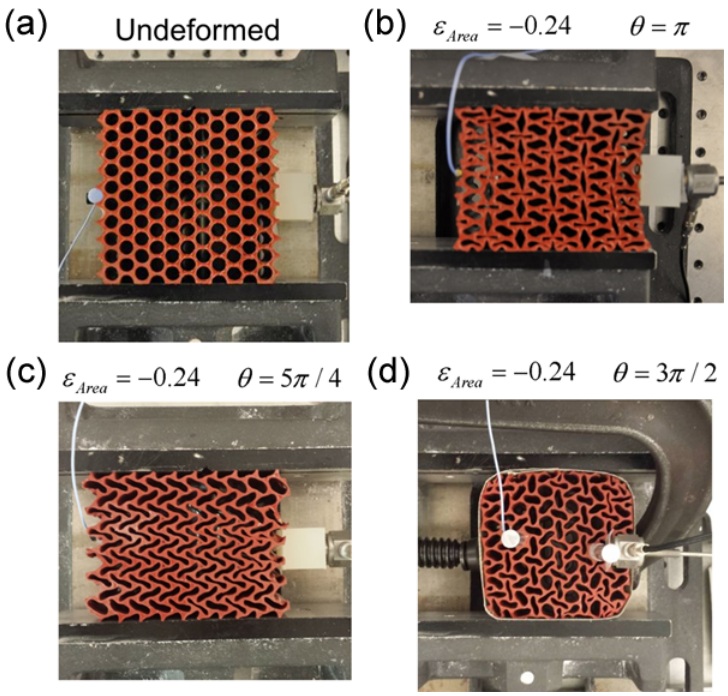

Figure E.13: (a) Picture of the undeformed sample with the shaker and accelerometer connected to it. (b) Picture of the sample deformed into the X-mode with the shaker and accelerometer connected to it. (c) Picture of the sample deformed into the Z-mode with the shaker and accelerometer connected to it. (d) Picture of the sample deformed into the chiral mode with the shaker and accelerometer connected to it.

contact with the fixture (see Fig. E.13-d). In this case the input wave from the shaker was transmitted through an inserted long rod and the output wave was detected from another inserted long rod away from the input.

F

Supporting Information for Chapter 7

F.1 Fabrication

We first describe the direct ink writing approach used to fabricate most of our structures, followed by a brief description of the manufacture of larger structures using a molding approach.

F.1.1 Direct Ink Writing

Samples were manufactured using direct ink writing, a facile extrusion-based 3D printing method. A viscoelastic polydimethylsiloxane (PDMS) ink was extruded through a tapered nozzle (with various nozzles used depending on the desired structure size—200 μm inner diameter tapered nozzle from Nordson EFD and 102 μm and 51 μm tapered nozzles from GPD Global). Ink extrusion was pressure controlled via Nordson EFD Ultimus V pressure box, with the nozzle precisely positioned using a custom 3D positioning stage (Aerotech). Fig. F.1 shows a few images of the printing process in which 3D architectures are fabricated in a layerwise build sequence.

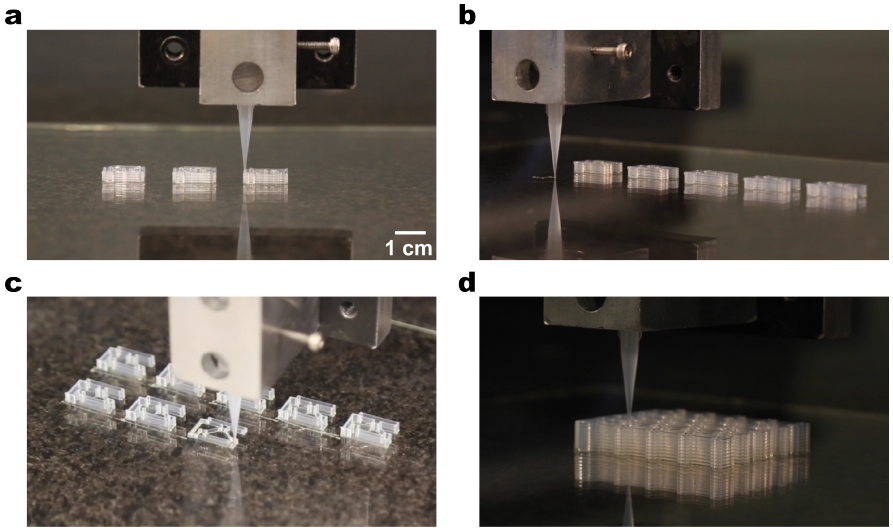

Figure F.1: a,b,c,d, Images of the direct ink writing process, in which a viscoelastic PDMS ink is extruded in filamentary form using a custom-built 3D robotic stage.

The PDMS-based ink is created by mixing Dow Corning SE-1700 (85 wt.%) with Dow Corning Sylgard 184 (15 wt.%). The viscoelastic yield properties are tailored to ensure that the uncured ink both flows readily during printing, yet maintains its shape until it is permanently cross-linked in a subsequent curing step (100°C for 30 min). After curing, the horizontal supporting members of the structure are infilled with epoxy (Momentive Epon 828) to prevent structural bending that would

disrupt the precise geometries of the elastomeric beams. As a result, the mechanical deformation of the printed structures is determined solely by the elastomeric beams. The shear-thinning and viscoelastic yield behavior of the PDMS ink is shown in Fig. F.2. Rheology measurements were made using a TA Instruments AR 2000EX rheometer with both 40 mm diameter plates (both flat as well as 2° cone).

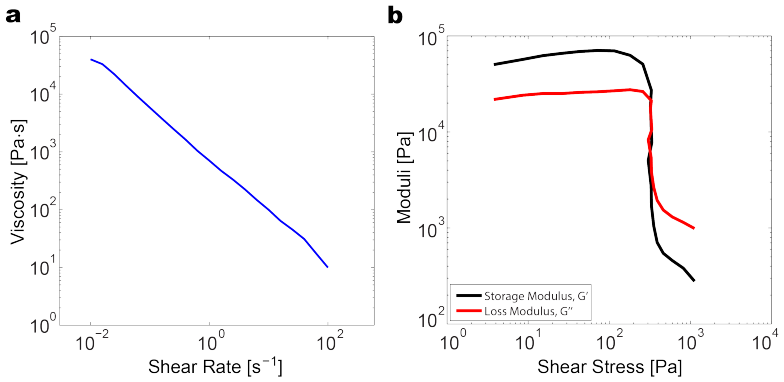

Figure F.2: **a** The viscosity of the PDMS ink is shown for shear rates relevant to the extrusion used during 3D printing. **b** The shear elastic and loss moduli of the ink as a function of shear stress.

The cured PDMS ink was tested under uniaxial tension using a single-axis Instron. The tests show that the material exhibits a behavior typical for elastomers: large strain elastic behavior with negligible rate dependence and negligible hysteresis during a loading-unloading cycle. The material behavior at a strain rate of 0.0087 s^{-1} is reported in Fig. F.3. The observed constitutive behavior is modeled as hyperelastic. Let $\mathrm{F} = \frac{\partial \mathrm{x}}{\partial \mathrm{X}}$ be the deformation gradient, mapping a material point from the reference position X to its current location x and J be its determinant, $J = \det\mathrm{F}$. For an isotropic hyperelastic material the strain energy density W can be expressed as a function of the invariants of the right Cauchy-Green tensor $\mathrm{C} = \mathrm{F}^T\mathrm{F}$ (or, alternatively, also the left Cauchy-Green tensor $\mathrm{B} = \mathrm{F}\mathrm{F}^T$). In particular, the behavior of nearly incompressible materials is effectively described by

splitting the deformation locally into volume-changing ($J^{1/3}\mathrm{I}$) and distortional ($\overline{\mathrm{F}}$) components as

$$\mathrm{F} = (J^{1/3}\mathrm{I})\overline{\mathrm{F}}, \tag{F.1}$$

where I denotes the identity matrix.

The PDMS stress-strain behavior is modeled using a Neo-Hookean model, modified to include compressibility (with a high bulk modulus):

$$W = \frac{\mu_0}{2}(\bar{I}_1 - 3) + \frac{K_0}{2}(J-1)^2, \tag{F.2}$$

where μ_0 and K_0 are the initial shear and bulk moduli and $\bar{I}_1 = \mathrm{tr}(\overline{\mathrm{F}}^T\overline{\mathrm{F}})$. The nominal (first Piola-Kirchoff) stress is then given by

$$\mathrm{S} = \frac{\partial W}{\partial \mathrm{F}} = \left[\mu_0 \mathrm{dev}\overline{\mathrm{B}} + K_0 J(J-1)\right]\mathrm{F}^{-T}, \tag{F.3}$$

where $\overline{\mathrm{B}} = \overline{\mathrm{F}}\overline{\mathrm{F}}^T$ and dev is the deviatoric operator

The material was modeled as nearly incompressible, characterized by $K_0/\mu_0 \approx 2500$. From the uniaxial tension data shown in Fig. F.3, the initial shear modulus was measured to be $\mu_0 = 0.32$ MPa. Fig. F.3 shows that the Neo-Hookean model captures the behavior very well up to a strain of about 1.0 which covers the majority of the strain levels studied.

F.1.2 Molding Approach

To manufacture larger structures (i.e., for L at the centimeter scale or larger) a molding approach is used. First, a negative mold was fabricated using a 3D printer (Connex 500 available from Objet, Ltd.) with VeroBlue (product number: RGD840, Objet) material. Then, the structures were cast using a silicone rubber (Mold Max 10 from Smooth-On). Before replication, a releasing agent

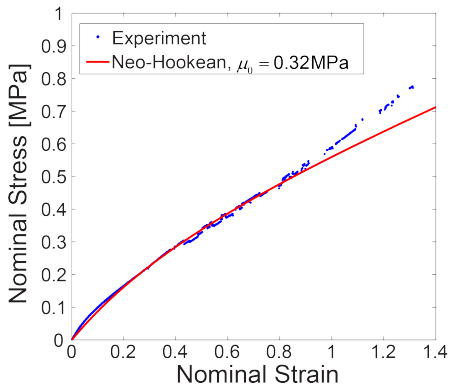

Figure F.3: Nominal stress versus nominal strain in uniaxial tension for the cured PDMS-based ink. Comparison between experimental data and model predictions.

(Easy Release 200 available from Smooth-On, Inc.) was sprayed on to the molds for easy separation. The casted mixture was first placed in vacuum for degassing and was allowed to set at room temperature for curing.

In the resulting structures each beam has length $L = 6$ mm, thickness t = 1 mm and out-of-plane height d=30 mm to minimize out-of-plane buckling. The overall sizes of the sample is $W(\text{width}) \times H(\text{height}) \times D(\text{thickness}) = 10.6 \times 10.8 \times 3.0$ cm. As shown in Fig. F.5, the structure is characterized by multiple stable configurations that can be triggered by applying a compressive force and that are maintained also when the force is removed.

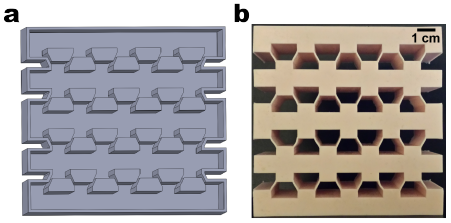

Figure F.4: a, 3D model of the negative mold. **b,** Sample manufactured using the mold and cast approach.

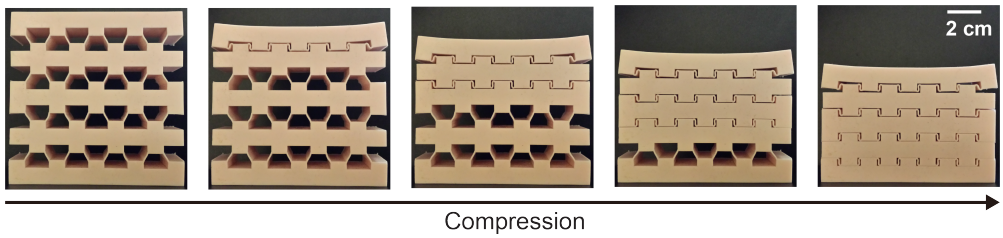

Figure F.5: Sequential images of a multistable structure manufactured using a mold and cast approach when loaded by hands. The structure is clearly multistable, retaining its deformed shape after release.

F.2 Testing

In this Section we describe the mechanical tests that we used to characterize the response of the structures.

F.2.1 Uniaxial Compression Tests

For stress-strain measurements, we used an Instron 5566 universal testing machine with a 10 N load cell. The specimens were compressed using flat compression fixtures. To test whether their response was rate-dependent, they were compressed at three different speeds—10 mm/s, 1 mm/s and 0.1 mm/s (in addition to higher rate impact tests discussed elsewhere). During the tests, the deformation of the samples was recorded every two seconds using a Nikon D90 digital SLR camera.

In most of our tests the specimens were unattached to the compression fixtures. In this case, the samples briefly lost contact with the compression plates during loading after the snap-though instability (see Fig. F.6a, third snapshot), resulting in a zero measured force during this time (see Fig. 3b in the main text and Fig. F.7). Moreover, if the structure is multistable, the deformed configuration is retained after unloading.

In a different set of tests the samples were glued to the compression plates. As shown in Fig. 3b in the main text and Fig. F.7 (continuous blue line), in this case the brief period of tensile reaction force occurring after the instability is recorded. Note that for the glued sample the initial configuration was always recovered after unloading since the glue allowed a tensile force to be applied to the structure during withdrawal of the compression plate (see Fig. F.6b).

Finally in Fig. F.7, we show the raw data collected from the compression test of the multistable structure shown in Fig. 3a in the main text (the normalized data are reported in Fig. 3b in the main text). Note that the measured force required to collapse a line of beams ($F_{collapse} \sim 3.1N$) is in excellent agreement with the acceleration peaks observed during the drop tests ($a \sim 80$ m/s^2, see

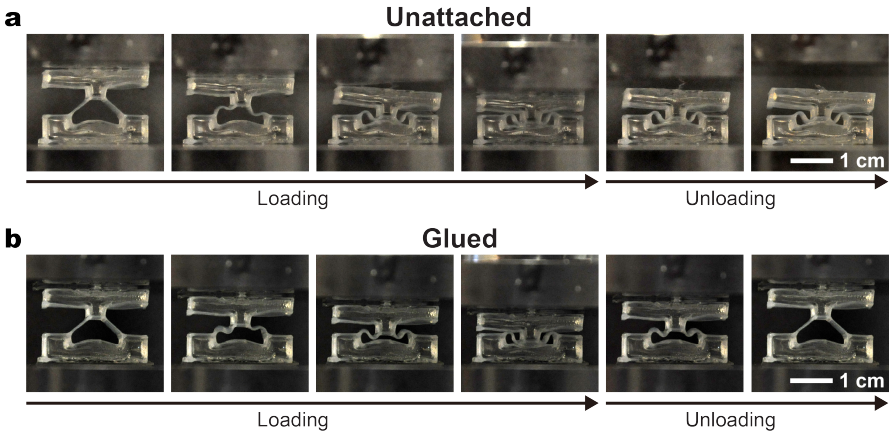

Figure F.6: a, Sequential images of the unattached bistable unit cell loaded vertically. The sample lost contact with the upper plate during loading after the instability and retained its deformed shape after unloading. **b,** Sequential images of the glued bistable unit cell loaded vertically. The sample was always attached to the plates and recovered its original shape after unloading.

Fig. 4a-b in the main text). In fact, this value of acceleration corresponds to a force $F = m \times a = 0.125\,g \times 80 m/s^2 = 10\,N$ ($m = 0.125$ g being the mass of the egg), that is approximately $3F_{collapse}$, with the factor three introduced because three identical samples arranged in parallel were used for the drop tests (see Fig. F.8a-b).

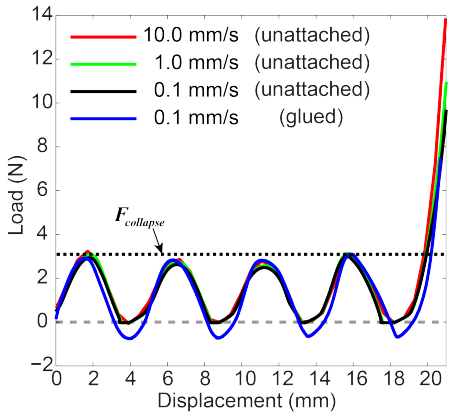

Figure F.7: Force-displacement curves for the multistable structure shown in Fig 2a of the main text at multiple strain rates. The overall dimensions of the sample are W×H×D=68.5 × 52 × 14.8 mm³

F.2.2 Drop Tests

We also characterized the ability of the system to provide protection during impact by dropping the samples from different heights, h, while recording the acceleration with a piezoelectric accelerometer (PCB Piezotronics, Inc., model number: 352C23) attached to their top. The acceleration was recorded at intervals of 0.1 ms using a National Instrument data acquisition system (NI 9234). To limit the out-of-plane motion, we used three identical samples connected in parallel by an acrylic fixture (see Fig. F.8a-b). Moreover, to ensure accuracy and consistency across the measurements, a set-up comprising a slide rail and a stage was used to guide the fall of the sample (see Fig. F.8c). We conducted experiments by dropping the samples from three different heights (h = 5.0 cm, 7.5 cm and 10.0 cm) and repeated each test 10 times. All experiments were conducted on an optical table (Newport Corporation).

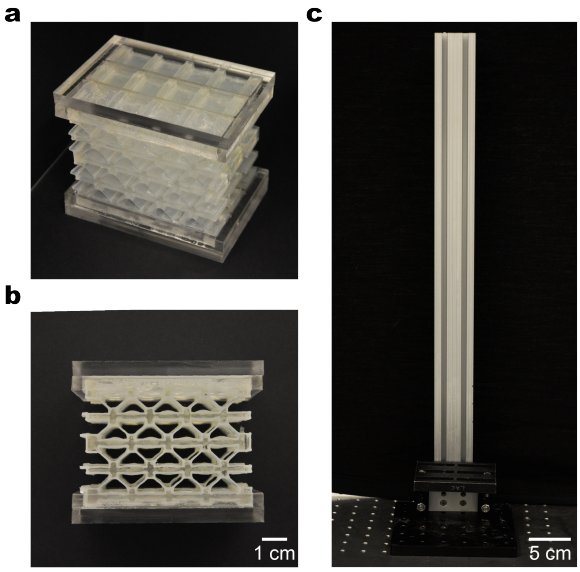

Figure F.8: a,b, Two different views of the assembled structure used for the drop tests. It consists of three identical multistable structures connected in parallel by an acrylic fixture on top and bottom; **c,** Dropping tower set-up consisting of a rail and a stage.

To illustrate the energy-absorbing capability of our multistable structures, we also dropped multistable and control samples with raw eggs attached to their top. Also in this case, we used three identical samples connected in parallel by an acrylic fixture (see Fig. F.8a-b) and the slide rail and stage (see Fig. F.8c). The samples were tested by dropping them from $h = 12.5$ cm with a raw egg attached on their top using a thin layer of adhesive (VHB tape). The eggs were placed such that the load from the impact was applied to their shortest axis. The drop test was recorded using a Phantom V9 high speed camera at 1000 pictures per second. Movie S5 shows a comparison between the multistable (left) and control (right) sample. Note that the movie is played at 20 fps (i.e. 50 times slower than the actual time scale). As shown in Fig. 4e in the main text, the eggs attached to the energy-absorbing structure could be preserved while the eggs on the control samples broke upon impact.

F.3 Numerical simulations

F.3.1 Finite Element analysis of elastic tilted beams

The commercial finite element (FE) code ABAQUS/Explicit (version 6.12) was used for simulating the response of elastic beams characterized by different combinations of ϑ and t/L. Assuming plane strain conditions, 2D FE models were constructed using ABAQUS element type *CPE6MH* and accuracy of each mesh was ascertained through a mesh refinement study. Each tilted beam was deformed by applying a vertical displacement to one of the ends, while completely constraining the motion of the other end. Moreover, the motion in the horizontal direction was constrained, as shown in Fig. 2c in the main text. Quasi-static conditions were ensured by monitoring the kinetic energy and introducing a small damping factor. The response of the material was captured using an almost incompressible Neo-Hookean model with initial shear modulus $\mu_0 = 0.32$ MPa and $K_0/\mu_0 = 2500$.

In each simulation, we monitored the evolution of the reaction force in the vertical direction. We then used the force-displacement data to calculate both the energy absorbed by the beam (E_{in}) and the energy cost for the beam to snap back to its undeformed configuration (E_{out}). The results are reported in Tables F.1 and F.2 (these data were used to generate the surface plots reported in Fig. 2e in the main text).

It is useful to compare these results to those obtained by experiments. We were particularly interested in understanding the transition between snap-through behavior with bistability and snap-through behavior without bistability. Fig. F.9 shows a comparison of experimental and simulated responses in this region of geometries, with the numbers indicating the E_{out} energy barrier as shown in Table F.2. The region of bistability determined experimentally is merely a subset of the region obtained with simulations. The simulated bistable region includes all shaded and colored cells in Fig. F.9. The grey cells indicate a subset of those geometries that are predicted to be bistable by sim-

ulations, but for which experiments show a snap-through response without bistability. Notice that these E_{out} energy values tend to be an order of magnitude smaller than the corresponding E_{out} values for the most stable configurations (i.e., those on the far left of the bistable region). In other words, the energy barrier to recovery is predicted by simulations to be very small for the right of the table. As a result, any small defects in the manufactured structures in this region would be sufficient to disrupt bistability, resulting in rapid recovery of the initial configuration upon unloading. Another region of discrepancy is indicated as the "Transition" zone (green stripes) in Fig. F.9. Here, E_{out} values are still sufficiently small that a combination of manufacturing defects and material time dependency are able to disrupt bistability. This zone consisted of geometries that exhibit ambiguous experimental results (e.g., for samples with the same prescribed geometry some were bistable and some were not, due to subtle imperfections) or geometries that were initially bistable upon loading, but soon recovered due to viscoelastic time dependency in the PDMS beams.

Table F.1: Normalized energy absorbed by the beam ($E_{in}/t\,d\,L\mu_o$) for different values of ϑ and t/L. (μ_o: shear modulus, $t\,d\,L$: volume of the beam, N: no snap-through)

ϑ and t/L	0.1	0.11	0.12	0.13	0.14	0.15	0.16	0.17	0.18	0.19	0.2
5	N	N	N	N	N	N	N	N	N	N	N
10	0	0	0	0	0	N	N	N	N	N	N
15	0	0	0	0	0	0	0	0	0	0	0
20	7.69×10^{-3}	8.46×10^{-3}	0	0	0	0	0	0	0	0	0
25	1.54×10^{-2}	1.65×10^{-2}	1.77×10^{-2}	1.92×10^{-2}	2.12×10^{-2}	0	0	0	0	0	0
30	2.38×10^{-2}	2.73×10^{-2}	1.88×10^{-2}	3.27×10^{-2}	3.50×10^{-2}	3.81×10^{-2}	4.15×10^{-2}	0	0	0	0
35	3.31×10^{-2}	3.88×10^{-2}	4.50×10^{-2}	5.04×10^{-2}	5.50×10^{-2}	5.88×10^{-2}	6.27×10^{-2}	6.81×10^{-2}	7.38×10^{-2}	8.04×10^{-2}	0
40	4.38×10^{-2}	5.19×10^{-2}	6.04×10^{-2}	6.92×10^{-2}	7.77×10^{-2}	8.50×10^{-2}	9.12×10^{-2}	9.73×10^{-2}	1.04×10^{-1}	1.12×10^{-1}	1.21×10^{-1}
45	5.69×10^{-2}	6.69×10^{-2}	7.81×10^{-2}	9.00×10^{-2}	1.02×10^{-1}	1.13×10^{-1}	1.24×10^{-1}	1.33×10^{-1}	1.41×10^{-1}	1.50×10^{-1}	1.62×10^{-1}
50	7.15×10^{-2}	8.42×10^{-2}	9.81×10^{-2}	1.13×10^{-1}	1.28×10^{-1}	1.44×10^{-1}	1.58×10^{-1}	1.71×10^{-1}	1.83×10^{-1}	1.95×10^{-1}	2.07×10^{-1}
55	8.81×10^{-2}	1.03×10^{-1}	1.20×10^{-1}	1.29×10^{-1}	1.58×10^{-1}	1.77×10^{-1}	1.95×10^{-1}	2.12×10^{-1}	2.27×10^{-1}	2.43×10^{-1}	0
60	1.06×10^{-1}	1.25×10^{-1}	1.45×10^{-1}	1.67×10^{-1}	1.89×10^{-1}	2.13×10^{-1}	2.36×10^{-1}	2.57×10^{-1}	2.75×10^{-1}	2.95×10^{-1}	0
65	1.27×10^{-1}	1.49×10^{-1}	1.72×10^{-1}	1.97×10^{-1}	2.25×10^{-1}	2.55×10^{-1}	2.83×10^{-1}	3.06×10^{-1}	3.31×10^{-1}	3.56×10^{-1}	0
70	1.52×10^{-1}	1.77×10^{-1}	2.03×10^{-1}	2.34×10^{-1}	2.67×10^{-1}	3.01×10^{-1}	3.33×10^{-1}	3.63×10^{-1}	3.95×10^{-1}	4.29×10^{-1}	N
75	1.82×10^{-1}	2.12×10^{-1}	2.44×10^{-1}	2.80×10^{-1}	3.19×10^{-1}	N	N	N	N	N	N
80	N	N	N	N	N	N	N	N	N	N	N
85	N	N	N	N	N	N	N	N	N	N	N
90	N	N	N	N	N	N	N	N	N	N	N

Table F.2: Normalized energy cost for the beam to snap back to its undeformed configuration ($E_{out}/tL\mu_o$) for different ϑ and t/L values. (μ_o: shear modulus, $t\,d\,L$: volume of the beam, N: no snap-through)

ϑ and t/L	0.1	0.11	0.12	0.13	0.14	0.15	0.16	0.17	0.18	0.19	0.2
5	N	N	N	N	N	N	N	N	N	N	N
10	0	0	0	0	0	N	N	N	N	N	N
15	0	0	0	0	0	0	0	0	0	0	0
20	2.67×10^{-4}	1.35×10^{-4}	0	0	0	0	0	0	0	0	0
25	1.23×10^{-3}	9.22×10^{-4}	5.65×10^{-4}	3.10×10^{-4}	4.55×10^{-5}	0	0	0	0	0	0
30	2.52×10^{-3}	2.46×10^{-3}	1.46×10^{-3}	1.09×10^{-3}	6.77×10^{-4}	2.74×10^{-4}	0	0	0	0	0
35	3.37×10^{-3}	3.71×10^{-3}	3.85×10^{-3}	3.73×10^{-3}	3.12×10^{-3}	2.23×10^{-3}	1.65×10^{-3}	1.16×10^{-3}	5.08×10^{-4}	5.58×10^{-5}	0
40	3.85×10^{-3}	4.62×10^{-3}	5.00×10^{-3}	5.38×10^{-3}	5.00×10^{-3}	4.62×10^{-3}	3.81×10^{-3}	2.85×10^{-3}	2.10×10^{-3}	1.28×10^{-3}	3.22×10^{-4}
45	4.62×10^{-3}	5.38×10^{-3}	5.77×10^{-3}	6.15×10^{-3}	6.54×10^{-3}	5.77×10^{-3}	5.77×10^{-3}	4.62×10^{-3}	3.33×10^{-3}	2.42×10^{-3}	8.53×10^{-4}
50	6.15×10^{-3}	6.54×10^{-3}	6.92×10^{-3}	6.92×10^{-3}	6.92×10^{-3}	6.54×10^{-3}	6.15×10^{-3}	5.77×10^{-3}	4.23×10^{-3}	2.30×10^{-3}	1.56×10^{-4}
55	7.31×10^{-3}	8.08×10^{-3}	7.69×10^{-3}	7.31×10^{-3}	7.31×10^{-3}	7.31×10^{-3}	6.15×10^{-3}	5.77×10^{-3}	3.85×10^{-3}	1.79×10^{-3}	0
60	8.46×10^{-3}	8.46×10^{-3}	8.46×10^{-3}	8.46×10^{-3}	8.08×10^{-3}	8.08×10^{-3}	7.69×10^{-3}	5.77×10^{-3}	2.67×10^{-3}	5.77×10^{-4}	0
65	9.62×10^{-3}	8.85×10^{-3}	8.85×10^{-3}	8.46×10^{-3}	8.46×10^{-3}	9.23×10^{-3}	7.31×10^{-3}	5.38×10^{-3}	3.08×10^{-3}	4.33×10^{-4}	0
70	1.04×10^{-2}	1.08×10^{-2}	9.23×10^{-3}	1.00×10^{-2}	1.12×10^{-2}	7.69×10^{-3}	6.92×10^{-3}	5.00×10^{-3}	2.23×10^{-3}	5.78×10^{-5}	N
75	1.15×10^{-2}	1.08×10^{-2}	1.27×10^{-2}	1.27×10^{-2}	1.42×10^{-2}	N	N	N	N	N	N
80	N	N	N	N	N	N	N	N	N	N	N
85	N	N	N	N	N	N	N	N	N	N	N
90	N	N	N	N	N	N	N	N	N	N	N

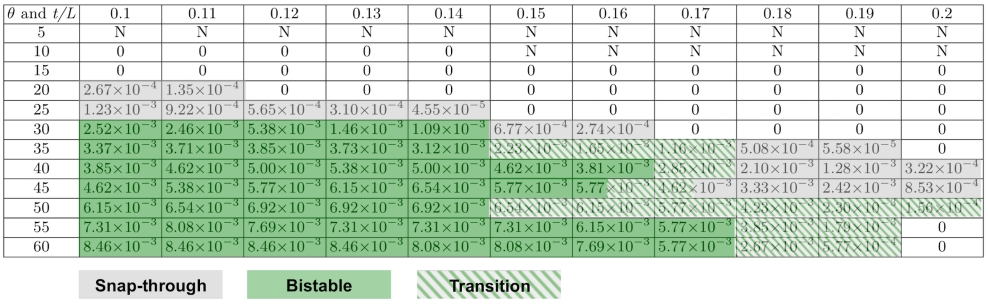

Figure F.9: A comparison of the mechanical response of geometries as determined by simulation and by experiment. All shaded and colored cells are predicted by simulation to be bistable. However, manufactured structures only show unambiguous bistability for the region indicated in green. The region with green stripes includes some ambiguous responses (e.g., where a sample is initially bistable upon deformation, but eventually recovers its initial configuration due to time dependency of the material). The grey region consists of geometries that experimentally are not bistable but are predicted to be bistable by simulation (notice the low energy barriers in this case, indicating that small defects are enough to disrupt the expected bistability).

F.3.2 Analysis of multistable structures

The FE simulations of individual elastic tilted beams described above were also used to predict the response of the multistable structures. In fact, the structure shown in Fig. 3a in the main text consists of four rows of eight parallel tilted beams, with each of these rows arranged in series. Moreover, the horizontal layers (infilled with epoxy) are much stiffer than the beams, so that they behave as rigid bodies and only the beams deform.

To predict the response of a multistable structure, we began by fitting the numerically obtained force-displacement curve of the corresponding individual beam with a polynomial. In particular, for the structure shown in Fig. 3a in the main text we used the FE results obtained for a single beam with $\vartheta = 40^o$ and $t/L = 0.12$ and fit the force-displacement curve with a polynomial of degree 10 (see Fig. F.10),

$$\begin{aligned} P(u) =& 0.0005u^{10} - 0.0133u^9 + 0.1395u^8 - 0.8079u^7 + 2.8184u^6 - 5.9982u^5 \\ &+ 7.3955u^4 - 4.2852u^3 - 0.2205u^2 + 1.2877u \end{aligned} \tag{F.4}$$

Note that the polynomial above was obtained for a beam with $L = 5.06$ mm, out-of-plane thickness $d = 14.8$ mm and shear modulus $\mu_o = 0.32$ MPa.

Therefore, each beam in the multistable structure can be treated as a non-linear spring, whose force-displacement behavior is given by Eq. (F.4). Moreover, each layer of beams consists of eight of such non-linear springs in parallel, so that

$$P_{row-i}(u_{row-i}) = 8P(u_{row-i}), \quad i = 1, 2, 3, 4, \tag{F.5}$$

where P_{row-i} and u_{row-i} are the total force and the displacement of the i-th row of beams. Furthermore, each structure consists of four such layers arranged in series, so that equilibrium and compati-

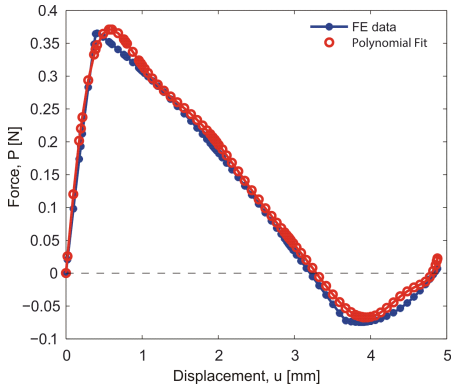

Figure F.10: Force-displacement curve for a tilted elastic beam with $\vartheta = 40^o$, $t/L = 0.12$, $L = 5.06$ mm, out-of-plane thickness $d = 14.8$ mm and shear modulus $\mu_o = 0.32$ MPa. Both the FE results (blue line) and the polynomial fit (red line) are shown.

bility require that

$$u = \sum_{i=1}^{4} u_{row-i}, \tag{F.6}$$

$$P_{row-1}(u_{row-1}) = P_{row-2}(u_{row-2}), \tag{F.7}$$

$$P_{row-2}(u_{row-2}) = P_{row-3}(u_{row-3}), \tag{F.8}$$

$$P_{row-3}(u_{row-3}) = P_{row-4}(u_{row-4}). \tag{F.9}$$

The system of non-linear equations (F.6) is solved numerically for increasing values of the applied displacement u using the trust-region-dogleg algorithm implemented in Matlab. Finally, to capture the sequential, rather than simultaneous, collapse of the rows observed in the experiments (due to imperfections), small perturbations were introduced into Eqns. (F.6). More specifically the terms $P_{row-i}(u_{row-i})$ were multiplied by a coefficient close to 1.0 (i.e. we use $\alpha_i P_{row-i}(u_{row-i})$ with $\alpha_1 = 0.94$, $\alpha_2 = 0.99$, $\alpha_3 = 1.02$ and $\alpha_4 = 1.04$).

References

[1] Agrawal, S. K., Kumar, S., & Yim, M. (2002). Polyhedral single degree-of-freedom expanding structures: Design and prototypes. *Journal of Mechanical Design*, 124(3), 473–478. 10.1115/1.1480413.

[2] Ahn, B. Y., Duoss, E. B., Motala, M. J., Guo, X., Park, S.-I., Xiong, Y., Yoon, J., Nuzzo, R. G., Rogers, J. A., & Lewis, J. A. (2009). Omnidirectional printing of flexible, stretchable, and spanning silver microelectrodes. *Science*, 323, 1590–1593.

[3] Almgren, R. (1985). An isotropic three-dimensional structure with poisson's ratio = -1. *Journal of Elasticity*, 15(4), 427–430.

[4] Arruda, E. M. & Boyce, M. C. (1993). A three-dimensional constitutive model for the large stretch behavior of rubber elastic materials. *Journal of the Mechanics and Physics of Solids*, 41(2), 389 – 412.

[5] Ayon, A. A., Braff, R., Lin, C. C., Sawin, H. H., & Schmidt, M. A. (1999). Characterization of a time multiplexed inductively coupled plasma etcher. *J. Electrochem. Soc.*, 146(1), 339–349.

[6] Baggetto, L., Danilov, D., & Notten, P. H. L. (2011). Honeycomb-structured silicon: Remarkable morphological changes induced by electrochemical (de)lithiation. *Advanced Materials*, 23(13), 1563–1566.

[7] Baughman, R., Shacklette, J., Zakhidov, A., & Stafstrom, S. (1998). Negative poisson's ratios as a common feature of cubic metals. *Nature*, 392, 362–365.

[8] Bazant, Z. P. & Cedolin, L. (1991). *Stability of Structures : Elastic, Inelastic, Fracture, and Damage Theories*. Oxford University Press.

[9] Bendsoe, M., Olhoff, N., Sigmund, O., & Mechanics, I. (2006). *IUTAM Symposium on Topological Design Optimization of Structures, Machines and Materials: Status and Perspectives*. Springer.

[10] Bertoldi, K. & Boyce, M. (2008a). Mechanically-triggered transformations of phononic band gaps in periodic elastomeric structures. *Phys. Rev. B*, 77, 052105.

[11] Bertoldi, K. & Boyce, M. C. (2008b). Wave propagation and instabilities in monolithic and periodically structured elastomeric materials undergoing large deformations. *Phys. Rev. B*, 78, 184107.

[12] Bertoldi, K., Boyce, M. C., Deschanel, S., Prange, S. M., & Mullin, T. (2008). Mechanics of deformation-triggered pattern transformations and superelastic behavior in periodic elastomeric structures. *J. Mech. Phys. Solids*, 56, 2642–2668.

[13] Bertoldi, K., Reis, P., Willshaw, S., & Mullin, T. (2010a). Negative poisson's ratio behavior induced by an elastic instability. *Adv. Mater.*, 22, 361–366.

[14] Bertoldi, K., Reis, P. M., Willshaw, S., & Mullin, T. (2010b). Negative Poisson's ratio behavior induced by an elastic instability. *Adv. Mater.*, 22, 361–6.

[15] Bettini, P., Airoldi, A., Sala, G., Di Landro, L., Ruzzene, M., & Spadoni, A. (2010). Composite chiral structures for morphing airfoils: Numerical analyses and development of a manufacturing process. *Compos. Part B-Eng.*, 41, 133–147.

[16] Bordacs, S., Kezsmarki, I., Szaller, D., Demk o, L., Kida, N., Murakawa, H., Onose, Y., Shimano, R., Room, T., Nagel, U., Miyahara, S., Furukawa, N., & Tokura, Y. (2012). Chirality of matter shows up via spin excitations. *Nature Physics*, 8, 734–738.

[17] Bria, D. & Djafari-Rouhani, B. (2002). Omnidirectional elastic band gap in finite lamellar structures. *Phys. Rev. E*, 66(5), 056609.

[18] Caddock, B. & Evans, K. (1989). Microporous materials with negative poisson's ratios. i. microstructure and mechanical properties. *J. Phys. D: Appl. Phys.*, 22(12), 1877.

[19] Casadei, F., Beck, B., Cunefare, K. A., & Ruzzene, M. (2012). Vibration control of plates through hybrid configurations of periodic piezoelectric shunts. *Int. J. Solids Struct.*, 23, 1169.

[20] Casadei, F., Dozio, L., Ruzzene, M., & Cunefare, K. (2010). Periodic shunted arrays for the control of noise radiation in an enclosure. *J. Sound. Vib.*, 329, 3632.

[21] Chan, E. & Crosby, A. (2006). Fabricating microlens arrays by surface wrinkling. *Advanced Materials*, 18(24), 3238–3242.

[22] Chan, E. P., Smith, E. J., Hayward, R., & Crosby, A. J. (2008). Surface wrinkles for smart adhesion. *Adv. Mater.*, 20(4), 711–716.

[23] Chandra, D., Yang, S., & Lin, P.-C. (2007). Strain responsive concave and convex microlens arrays. *Applied Physics Letters*, 91(25).

[24] Chetcuti, E., Ellul, B., Manicaro, E., Brincat, J., Attard, D., Gatt, R., & Grima, J. (2014). Modeling auxetic foams through semi-rigid rotating triangles. *physica status solidi (b)*, 251(2), 297–306.

[25] Cho, Y., Shin, J., Costa, A., Kim, T., Kunin, V., Li, J., Lee, S., Yang, S., Han, H., Choi, I., & Srolovitz, D. (2014). Engineering the shape and structure of materials by fractal cut. *Proceedings of the National Academy of Sciences*, 111(49), 17390–17395.

[26] Choi, J. & Lakes, R. (1992). Non-linear properties of polymer cellular materials with a negative poisson's ratio. *J. Mater. Sci.*, 27(17), 4678–4684.

[27] Chung, J. & Waas, A. (2001). In-plane biaxial crush response of polycarbonate honeycombs. *J. Eng. Mech.*, 127(2), 180–193.

[28] Clinton, J. D. (1971). Advanced structural geometry studies. part 2: A geometric transformation concept for expanding rigid structures. *NASA Report CR-1735*, (CR-1735).

[29] Colby, R. H. (2007). Polyelectrolyte gels: Ionic partners split up. *Nat Mater*, 6(6), 401–402. 10.1038/nmat1908.

[30] Correa, D. M., Klatt, T., Cortes, S., Haberman, M., Kovar, D., & Seepersad, C. (2015). Negative stiffness honeycombs for recoverable shock isolation. *Rapid Prototyping Journal*, 21, 193–200.

[31] Danielsson, M., Parks, D., & Boyce, M. (2002). Three-dimensional micromechanical modeling of voided polymeric materials. *J. Mech. Phys. Solids*, 50(2), 351–379.

[32] Dawson, M. A., McKinley, G. H., & Gibson, L. J. (2008). The dynamic compressive response of open-cell foam impregnated with a newtonian fluid. *J. Appl. Mech.*, 75, 041015.

[33] Dian-Long, Y., Yao-Zong, L., Jing, Q., Hong-Gang, Z., & Zhi-Ming, L. (2005). Experimental and theoretical research on the vibrational gaps in two-dimensional three-component composite thin plates. *Chin. Phys. Lett.*, 22(8), 1958.

[34] Edlund, E., Lindgren, O., & Jacobi, M. N. (2012). Chiral surfaces self-assembling in one-component systems with isotropic interactions. *Phys. Rev. Lett.*, 108, 165502.

[35] Elnady, T., Elsabbagh, A., Akl, W., Mohamady, O., Garcia-Chocano, V. M., Torrent, D., Cervera, F., & Sánchez-Dehesa, J. (2009). Quenching of acoustic bandgaps by flow noise. *Appl. Phys. Lett.*, 94(13), 134104.

[36] Elser, D., Andersen, U. L., Korn, A., Glöckl, O., Lorenz, S., Marquardt, C., & Leuchs, G. (2006). Reduction of guided acoustic wave brillouin scattering in photonic crystal fibers. *Phys. Rev. Lett.*, 97, 133901.

[37] Eschenauer, H. A. & Olhoff, N. (2001). Topology optimization of continuum structures: A review*. *Applied Mechanics Reviews*, 54(4), 331–390. 10.1115/1.1388075.

[38] Evans, K. E. & Alderson, A. (2000). Auxetic Materials: Functional Materials and Structures from Lateral Thinking! *Adv. Mater*, 12(9), 617–628.

[39] Evans, K. E., Nkansah, M. A., Hutchinson, I. J., & Rogers, S. C. (1991). Molecular network design. *Nature*, 353, 124.

[40] Fargette, A., Neukirch, S., & Antkowiak, A. (2014). Elastocapillary Snapping: Capillarity Induces Snap-Through Instabilities in Small Elastic Beams. *Phys. Rev. Lett.*, 112, 137802.

[41] Ferjani, S., Choi, Y., Pendery, J., Petschek, R., & Rosenblatt, C. (2010). Mechanically generated surface chirality at the nanoscale. *Phys. Rev. Lett.*, 104, 257801.

[42] Florijn, B., Coulais, C., & van Hecke, M. (2014). Programmable mechanical metamaterials. *Phys. Rev. Lett.*, 113, 175503.

[43] Foppl, A. (1907). *Vorlesungen uber technische Mechanik*. Leipzig, Germany: B.G. Teubner.

[44] Forterre, Y., Skotheim, J. M., Dumais, J., & Mahadevan, L. (2005). How the venus flytrap snaps. *Nature*, 433(7024), 421–425.

[45] Frank, F. C. (1953). On spontaneous asymmetric synthesis. *Biochim. Biophys. Acta*, 11(4), 459–463.

[46] Fraternali, F., Blesgen, T., Amendola, A., & Daraio, C. (2011). Multiscale mass-spring models of carbon nanotube foams. *Journal of the Mechanics and Physics of Solids*, 59(1), 89 – 102.

[47] Gatt, R., Mizzi, L., Azzopardi, J., Azzopardi, K., Attard, D., Casha, A., Briffa, J., & Grima, J. (2015). Hierarchical auxetic mechanical metamaterials. *Sci. Rep.*, 5.

[48] Gent, A. N. (1996). A new constitutive relation for rubber. *Rubber Chemistry and Technology*, 69(1), 59–61.

[49] Geymonat, G., Muller, S., & Triantafyllidis, N. (1993). Homogenization of nonlinearly elastic materials, microscopic bifurcation and macroscopic loss of rank-one convexity. *Arch. Ration. Mech. Anal.*, 122, 231.

[50] Gibson, L. & Ashby, F. (1997). *Cellular Solids: Structure and Properties*. Cambridge, U.K.: Cambridge University Press.

[51] Gibson, L., Ashby, M., Zhang, J., & Triantafillou, T. (1989). Failure surfaces for cellular materials under multiaxial loads—i.modelling. *Int. J. Solids Struct.*, 31(9), 635–663.

[52] Gong, L., Kyriakides, S., & Jang, W.-Y. (2005). Compressive response of open-cell foams. part i: Morphology and elastic properties. *Int. J. Solids Struct.*, 42(5-6), 1355–1379.

[53] Gratson, G. M., Xu, M., & Lewis, J. A. (2004). Direct writing of three-dimensional webs. *Nature*, 428, 386.

[54] Green, M. M., Peterson, N. C., Sato, T., Teramoto, A., Cook, R., & Lifson, S. (1995). A helical polymer with a cooperative response to chiral information. *Science*, 268(5219), 1860–1866.

[55] Grima, J., Alderson, A., & Evans, K. (2005). Auxetic behaviour from rotating rigid units. *physica status solidi (b)*, 242(3), 561–575.

[56] Grima, J. N., Jackson, R., Alderson, A., & Evans, K. (2000). Do zeolites have negative poisson's ratios? *Advanced Materials*, 12(24), 1912–1918.

[57] Grinthal, A., Kang, S. H., Epstein, A. K., Aizenberg, M., Khan, M., & Aizenberg, J. (2012). Steering nanofibers: An integrative approach to bio-inspired fiber fabrication and assembly. *Nano Today*, 7(1), 35–52.

[58] Grohol, D., Matan, K., Cho, J. H., Lee, S. H., Lynn, J. W., Nocera, D. G., & Lee, Y. S. (2005). Spin chirality on a two-dimensional frustrated lattice. *Nature Mater.*, 4(4), 323–328.

[59] Guest, S. & Pellegrino, S. (2006). Analytical models for bistable cylindrical shells. *Proceedings of the Royal Society of London A: Mathematical, Physical and Engineering Sciences*, 462(2067), 839–854.

[60] Guo, Q., Zheng, H., Chen, W., & Chen, Z. (2014). Modeling bistable behaviors in morphing structures through finite element simulations. *Biomed Mater Eng*, 24(1), 557–62.

[61] Haftka, R. T. & Grandhi, R. V. (1986). Structural shape optimization—a survey. *Computer Methods in Applied Mechanics and Engineering*, 57(1), 91–106.

[62] Hayes, A. M., Wang, A., Dempsey, B. M., & McDowell, D. L. (2004). Mechanics of linear cellular alloys. *Mech. Mater.*, 36(8), 691 – 713.

[63] Hendry, E., Carpy, T., Johnston, J., Popland, M., Mikhaylovskiy, R. V., Lapthorn, A. J., Kelly, S. M., Barron, L. D., Gadegaard, N., & Kadodwala, M. (2010). Ultrasensitive detection and characterization of biomolecules using superchiral fields. *Nat. Nanotechnol.*, 5(11), 783–787.

[64] Hoberman, C. (1990). Reversibly expandable doubly-curved truss structure.

[65] Holmes, D. & Crosby, A. (2007). Snapping surfaces. *Advanced Materials*, 19(21), 3589–3593.

[66] Hong, W., Zhao, X., Zhou, J., & Suo, Z. (2008). A theory of coupled diffusion and large deformation in polymeric gels. *Journal of the Mechanics and Physics of Solids*, 56(5), 1779 – 1793.

[67] Horozov, T. S., Binks, B. P., Aveyard, R., & Clint, J. H. (2006). Effect of particle hydrophobicity on the formatlon and collapse of fumed silica particle monolayers at the oil-water interface. *Colloid Surface A*, 282, 377–386.

[68] Hou, X., Hu, H., & Silberschmidt, V. (2014). Numerical analysis of composite structure with in-plane isotropic negative poisson's ratio: Effects of materials properties and geometry features of inclusions. *Composites Part B: Engineering*, 58, 152 – 159.

[69] Hyun, D. C., Moon, G. D., Cho, E. C., & Jeong, U. (2009). Repeated transfer of colloidal patterns by using reversible buckling process. *Adv. Funct. Mater.*, 19, 2155.

[70] Ilievski, F., Mazzeo, A. D., Shepherd, R. F., Chen, X., & Whitesides, G. M. (2011). Soft robotics for chemists. *Angewandte Chemie International Edition*, 50(8), 1890–1895.

[71] Jang, J.-H., Koh, C. Y., Bertoldi, K., Boyce, M. C., & Thomas, E. L. (2009). Combining pattern instability and shape-memory hysteresis for phononic switching. *Nano Lett.*, 9(5), 2113–2119.

[72] Jang, J.-H., Ullal, C. K., Gorishnyy, T., Tsukruk, V. V., & Thomas, E. L. (2006). Mechanically tunable three-dimensional elastomeric network/air structures via interference lithography. *Nano Lett.*, 6(4), 740–743.

[73] Jaques, J., Collet, A., & Wilen, S. H. (1994). *Enatiomers, Racemates and Resolutions*. Melbourne: Krieger Publishing Company.

[74] Kafesaki, M., Sigalas, M. M., & Garcia, N. (2000). Frequency modulation in the transmittivity of wave guides in elastic-wave band-gap materials. *Phys. Rev. Lett.*, 85, 4044–4047.

[75] Kang, S. H., Wu, N., Grinthal, A., & Aizenberg, J. (2011). Meniscus lithography: Evaporation-induced self-organization of pillar arrays into moire patterns. *Phys. Rev. Lett.*, 107(17), 177802.

[76] Kapko, V., Treacy, M., Thorpe, M., & Guest, S. (2009). On the collapse of locally isostatic networks. *Proc. R. Soc. A*, 465, 3517–3530.

[77] Keskar, N. R. & Chelikowsky, J. R. (1992). Negative poisson ratios in crystalline sio_2 from first-principles calculations. *Nature*, 358, 222–224.

[78] Khang, D.-Y., Rogers, J. A., & Lee, H. H. (2009). Mechanical buckling: Mechanics, metrology, and stretchable electronics. *Advanced Functional Materials*, 19(10), 1526–1536.

[79] Khare, K., Zhou, J., & Yang, S. (2009). Tunable open-channel microfluidics on soft poly(dimethylsiloxane) (pdms) substrates with sinusoidal grooves. *Langmuir*, 25(21), 12794–12799.

[80] Khelif, A., Choujaa, A., Benchabane, S., Djafari-Rouhani, B., & Laude, V. (2004). Guiding and bending of acoustic waves in highly confined phononic crystal waveguides. *Appl. Phys. Lett.*, 84(22), 4400–4402.

[81] Khelif, A., Djafari-Rouhani, B., Vasseur, J. O., Deymier, P. A., Lambin, P., & Dobrzynski, L. (2002). Transmittivity through straight and stublike waveguides in a two-dimensional phononic crystal. *Phys. Rev. B*, 65, 174308.

[82] Kim, H. S. & Crosby, A. J. (2011). Solvent-responsive surface via wrinkling instability. *Advanced Materials*, 23(36), 4188–4192.

[83] Kim, J. B., Kim, P., Pegard, N. C., Oh, S. J., Kagan, C. R., Fleischer, J. W., Stone, H. A., & Loo, Y.-L. (2012). Wrinkles and deep folds as photonic structures in photovoltaics. *Nat Photon*, 6(5), 327–332.

[84] Kim, S. H., Hong, K., Xie, W., Lee, K. H., Zhang, S., Lodge, T. P., & Frisbie, C. D. (2013). Electrolyte-gated transistors for organic and printed electronics. *Advanced Materials*, 25(13), 1822–1846.

[85] Kondepudi, D. K., Kaufman, R. J., & Singh, N. (1990). Chiral symmetry-breaking in sodium-chlorate crystallization. *Science*, 250(4983), 975–976.

[86] Kovacs, F., Tarnai, T., Fowler, P. W., & Guest, S. D. (2004). A class of expandable polyhedral structures. *International Journal of Solids and Structures*, 41(3–4), 1119–1137.

[87] Krishnan, D. & Johnson, H. (2009). Optical properties of two-dimensional polymer photonic crystals after deformation-induced pattern transformations. *J. Mech. Phys. Solids*, 57(9), 1500–1513.

[88] Kushwaha, M. S., Halevi, P., Dobrzynski, L., & Djafari-Rouhani, B. (1993). Acoustic band structure of periodic elastic composites. *Phys. Rev. Lett.*, 71, 2022–2025.

[89] Lagoudas, D. (2008). *Shape Memory Alloys: Modeling and Engineering Applications*. Springer.

[90] Lakes, R. S. (1987). Foam structures with a negative poisson's ratio. *Science*, 235(4792), 1038–1040.

[91] Landau, L. D. & Lifshitz, E. M. (1986). *Theory of Elasticity*. Elsevier, New York, NY, 3rd ed. edition.

[92] Larsen, U., Sigmund, O., & Bouwstra, S. (1996). Design and fabrication of compliant micromechanisms and structures with negative poisson's ratio. In *Micro Electro Mechanical Systems, 1996, MEMS '96, Proceedings. An Investigation of Micro Structures, Sensors, Actuators, Machines and Systems. IEEE, The Ninth Annual International Workshop on* (pp. 365–371).

[93] Lee, J., Singer, J., & Thomas, E. (2012a). Micro-/nanostructured mechanical metamaterials. *Advanced Materials*, 24(36), 4782–4810.

[94] Lee, J.-H., Wang, L., Boyce, M. C., & Thomas, E. L. (2012b). Periodic bicontinuous composites for high specific energy absorption. *Nano Lett.*, 12(8), 4392–4396.

[95] Lee, S.-K., Kabir, S. M. H., Sharma, B. K., Kim, B. J., Cho, J. H., & Ahn, J.-H. (2014). Photopatternable ion gel-gated graphene transistors and inverters on plastic. *Nanotechnology*, 25(1), 014002.

[96] Lewis, J. A. (2006). Direct ink writing of 3d functional materials. *Adv. Funct. Mater.*, 16, 2193–2204.

[97] Li, J., Shim, J., Deng, J., Overvelde, J., Zhu, X., Bertoldi, K., & Yang, S. (2012). Switching periodic membranes via pattern transformation and shape memory effect. *Soft Matter*, 8, 10322.

[98] Li, J.-B., Wang, Y.-S., & Zhang, C. (2013). Tuning of acoustic bandgaps in phononic crystals with helmholtz resonators. *J. Vib. Acoust.*, 135, 031015.

[99] Link, D. R., Natale, G., Shao, R., Maclennan, J. E., Clark, N. A., Korblova, E., & Walba, D. M. (1997). Spontaneous formation of macroscopic chiral domains in a fluid smectic phase of achiral molecules. *Science*, 278, 1924–1927.

[100] Lu, C., Mohwald, H., & Fery, A. (2007). A lithography-free method for directed colloidal crystal assembly based on wrinkling. *Soft Matter*, 3, 1530–1536.

[101] Luna, J. I., Ciriza, J., Garcia-Ojeda, M. E., Kong, M., Herren, A., Lieu, D. K., Li, R. A., Fowlkes, C. C., Khine, M., & McCloskey, K. E. (2011). Multiscale biomimetic topography for the alignment of neonatal and embryonic stem cell-derived heart cells. *Tissue Engineering Part C-Methods*, 17(5), 579–588.

[102] Maldovan, M. (2013). Narrow low frequency spectrum and heat management by thermocrystals. *Phys. Rev. Lett.*, 110, 025902.

[103] Maldovan, M. & Thomas, E. L. (2009). *Periodic Materials and Interference lithography for Photonics, Phononics and Mechanics*. Weinheim: Wiley,-VCH.

[104] Maluf, N. (2000). *An Introduction to Microelectromechanical Systems Engineering*. Norwood, MA: Artech House.

[105] Matsumoto, E. A. & Kamien, R. D. (2009). Elastic-instability triggered pattern formation. *Phys. Rev. E*, 80, 021604.

[106] Meza, L. R., Das, S., & Greer, J. R. (2014). Strong, lightweight, and recoverable three-dimensional ceramic nanolattices. *Science*, 345(6202), 1322–1326.

[107] Mitschke, H., Schwerdtfeger, J., Schury, F., Stingl, M., K□ner, C., Singer, R., Robins, V., Mecke, K., & Schr□er-Turk, G. (2011). Finding auxetic frameworks in periodic tessellations. *Advanced Materials*, 23(22-23), 2669–2674.

[108] Mooney, M. (1940). A theory of large elastic deformation. *Journal of Applied Physics*, 11(9), 582–592.

[109] Movchan, A., Movchan, N., & Haq, S. (2006). Localised vibration modes and stop bands for continuous and discrete periodic structures. *Mat. Sci. Eng.*, 431, 175–183.

[110] Mullin, T., Deschanel, S., Bertoldi, K., & Boyce, M. C. (2007). Pattern transformation triggered by deformation. *Phys. Rev. Lett.*, 99, 084301.

[111] Needham, D. & Nunn, R. (1990). Elastic deformation and failure of lipid bilayer membranes containing cholesterol. *Biophys. J.*, 58(4), 997–1009.

[112] Newnham, R. (2004). *Properties of Materials : Anisotropy, Symmetry, Structure: Anisotropy, Symmetry, Structure*. OUP Oxford.

[113] Noorduin, W. L., Bode, A. A. C., van der Meijden, M., Meekes, H., van Etteger, A. F., van Enckevort, W. J. P., Christianen, P. C. M., Kaptein, B., Kellogg, R. M., Rasing, T., & Vlieg, E. (2009). Complete chiral symmetry breaking of an amino acid derivative directed by circularly polarized light. *Nature Chemistry*, 1(9), 729–732.

[114] Ogden, R. W. (1972). Large deformation isotropic elasticity - correlation of theory and experiment for compressible rubberlike solids. *Proceedings of the Royal Society of London Series a-Mathematical and Physical Sciences*, 328(1575), 567.

[115] Ogden, R. W. (1998). *Nonlinear Elastic Deformations*. Dover.

[116] Ohno, N., Okumura, D., & Noguchi, H. (2002). Microscopic symmetric bifurcation condition of cellular solids based on a homogenization theory of finite deformation. *J. Mech. Phys. Solids*, 50(5), 1125 – 1153.

[117] Overvelde, J., S., S., & Bertoldi, K. (2012). Compaction through buckling in 2d periodic, soft and porous structures: Effect of pore shape. *Adv. Mater.*, 24, 2337–2342.

[118] Overvelde, J. T. & Bertoldi, K. (2014). Relating pore shape to the non-linear response of periodic elastomeric structures. *Journal of the Mechanics and Physics of Solids*, 64(0), 351–366.

[119] Pandey, A., Moulton, D., Vella, D., & Holmes, D. (2014). Dynamics of Snapping Beams and Jumping Poppers. *EPL-Europhys. Lett.*, 105, 24001.

[120] Papka, S. & Kyriakides, S. (1999a). Biaxial crushing of honeycombs: –part i: Experiments. *Int. J. Solids Struct.*, 36(29), 4367 – 4396.

[121] Papka, S. & Kyriakides, S. (1999b). In-plane biaxial crushing of honeycombs: –part ii: Analysis. *Int. J. Solids Struct.*, 36(29), 4397 – 4423.

[122] Papka, S. D. & Kyriakides, S. (1994). In-plane compressive response and crushing of honeycomb. *J. Mech. Phys. Solids*, 42, 1499 – 1532.

[123] Patil, H. S. & Vaijapurkar, S. (2007). Study of the geometry and folding pattern of leaves of mimosa pudica. *Journal of Bionic Engineering*, 4(1), 19–23.

[124] Pellegrino, S. & Sciences, I. C. f. M. (2001). *Deployable Structures*. Springer.

[125] Pokroy, B., Epstein, A. K., Persson-Gulda, M. C. M., & Aizenberg, J. (2009a). Fabrication of bioinspired actuated nanostructures with arbitrary geometry and stiffness. *Advanced Materials*, 21(4), 463–469.

[126] Pokroy, B., Kang, S. H., Mahadevan, L., & Aizenberg, J. (2009b). Self-organization of a mesoscale bristle into ordered, hierarchical helical assemblies. *Science*, 323(5911), 237–240.

[127] Prall, D. & Lakes, R. S. (1997). Properties of a chiral honeycomb with a poisson's ratio of -1. *Int. J. Mech. Sci.*, 39, 305.

[128] Pugsley, A. & Macaulay, M. (1960). The large-scale crumpling of thin cylindrical columns. *Q. J. Mech. Appl. Math.*, 13, 1–9.

[129] Åberg, M. & Gudmundson, P. (1997). The usage of standard finite element codes for computation of dispersion relations in materials with periodic microstructure. *J. Acoust. Soc. Am.*, 102, 2007–2013.

[130] Rahmawan, Y., Moon, M.-W., Kim, K.-S., Lee, K.-R., & Suh, K.-Y. (2010). Wrinkled, dual-scale structures of diamond-like carbon (dlc) for superhydrophobicity. *Langmuir*, 26(1), 484–491.

[131] Reid, S. R. (1993). Plastic deformation mechanisms in axially compressed metal tubes used as impact energy absorbers. *Int. J. Mech. Sci.*, 35, 1035–1052.

[132] Richard, J. & Leo, R. (1988). Note on a random isotropic granular material with negative poisson's ratio. *International Journal of Engineering Science*, 26(4), 373 – 383.

[133] Rogers, J. A. (2013). A clear advance in soft actuators. *Science*, 341(6149), 968–969.

[134] Rogers, J. A., Someya, T., & Huang, Y. (2010). Materials and mechanics for stretchable electronics. *Science*, 327(5973), 1603–1607.

[135] Salari-Sharif, L., Schaedler, T., & Valdevit, L. (2014). Energy Dissipation Mechanisms in Hollow Metallic Microlattices. *Journal of Materials Research*, 29, 1755–1770.

[136] Scarpa, F., Blain, S., Lew, T., Perrott, D., Ruzzene, M., & Yates, J. (2007). Elastic buckling of hexagonal chiral cell honeycombs. *Composites Part A: Applied Science and Manufacturing*, 38(2), 280 – 289.

[137] Schaedler, T., Jacobsen, A., Torrents, A., Sorensen, A., Lian, J., Greer, J., Valdevit, L., & Carter, W. (2011). Ultralight metallic microlattices. *Science*, 334, 962–965.

[138] Schurig, D., Mock, J. J., Justice, B. J., Cummer, S. A., Pendry, J. B., Starr, A. F., & Smith, D. R. (2006). Metamaterial electromagnetic cloak at microwave frequencies. *Science*, 314(5801), 977–980.

[139] Schwerdtfeger, J., Schury, F., Stingl, M., Wein, F., Singer, R., & K□ner, C. (2012). Mechanical characterisation of a periodic auxetic structure produced by sebm. *Phys. Status Solidi B*, 249, 1347–1352.

[140] Sharon, E., Marder, M., & Swinney, H. L. (2004). Leaves, flowers and garbage bags: Making waves. *American Scientist*, 92(3), 254–261.

[141] Shim, J., Perdigou, C., Chen, E. R., Bertoldi, K., & Reis, P. M. (2012). Buckling-induced encapsulation of structured elastic shells under pressure. *Proceedings of the National Academy of Sciences*, 109(16), 5978–5983.

[142] Shim, J., Shan, S., Kosmrlj, A., Kang, S., Chen, E., Weaver, J., & Bertoldi, K. (2013). Harnessing instabilities for design of soft reconfigurable auxetic/chiral materials. *Soft Matter*, 9, 8198–8202.

[143] Shipman, P. D. & Newell, A. C. (2004). Phyllotactic patterns on plants. *Phys. Rev. Lett.*, 92(16), 168102.

[144] Shufrin, I., Pasternak, E., & Dyskin, A. (2012). Planar isotropic structures with negative poisson's ratio. *International Journal of Solids and Structures*, 49(17), 2239 – 2253.

[145] Silverberg, J. L., Noar, R. D., Packer, M. S., Harrison, M. J., Henley, C. L., Cohen, I., & Gerbode, S. J. (2012). 3d imaging and mechanical modeling of helical buckling in medicago truncatula plant roots. *Proc Natl Acad Sci U S A*, 109(42), 16794–9.

[146] Singamaneni, S., Bertoldi, K., Chang, S., Jang, J., Young, S. L., Thomas, E. L., Boyce, M. C., & Tsukruk, V. V. (2009a). Bifurcated mechanical behavior of deformed periodic porous solids. *Adv. Funct. Mater.*, 19, 1426.

[147] Singamaneni, S., Bertoldi, K., Chang, S., Jang, J.-H., Thomas, E. L., Boyce, M. C., & Tsukruk, V. V. (2009b). Instabilities and pattern transformation in periodic, porous elastoplastic solid coatings. *ACS Applied Materials & Interfaces*, 1(1), 42–47.

[148] Singamaneni, S., McConney, M. E., & Tsukruk, V. V. (2010). Swelling-induced folding in confined nanoscale responsive polymer gels. *ACS Nano*, 4(4), 2327–2337.

[149] Singamaneni, S. & Tsukruk, V. V. (2010). Buckling instabilities in periodic composite polymeric materials. *Soft Matter*, 6(22), 5681–5692.

[150] Smay, J. E., Cesarano III, J., & Lewis, J. A. (2002). Colloidal inks for directed assembly of 3d periodic structures. *Langmuir*, 18(14), 5429–5437.

[151] Soai, K., Shibata, T., Morioka, H., & Choji, K. (1995). Asymmetric autocatalysis and amplification of enantiomeric excess of a chiral molecule. *Nature*, 378(6559), 767–768.

[152] Son, K., Guasto, J. S., & Stocker, R. (2013). Bacteria can exploit a flagellar buckling instability to change direction. *Nat Phys*, 9(8), 494–498.

[153] Song, F., Zhou, J., Xu, X., Xu, Y., & Bai, Y. (2008). Effect of a negative poisson ratio in the tension of ceramics. *Phys. Rev. Lett.*, 100, 245502.

[154] Soukoulis, C. M. & Wegener, M. (2011). Past achievements and future challenges in the development of three-dimensional photonic metamaterials. *Nature Photonics*, 5(9), 523–530.

[155] Spadoni, A., Ruzzene, M., & Scarpa, F. (2005). Global and local linear buckling behavior of a chiral cellular structure. *Physica Status Solidi B-Basic Solid State Physics*, 242(3), 695–709.

[156] Sun, J.-H. & Wu, T.-T. (2005). Analyses of mode coupling in joined parallel phononic crystal waveguides. *Phys. Rev. B*, 71, 174303.

[157] Sun, J.-H. & Wu, T.-T. (2006). Guided surface acoustic waves in phononic crystal waveguides. *IEEE Ultrasonics Symposium*, 1, 673.

[158] Sun, J.-H. & Wu, T.-T. (2007). Propagation of acoustic waves in phononic-crystal plates and waveguides using a finite-difference time-domain method. *Phys. Rev. B*, 76, 104304.

[159] Sun, J.-Y., Zhao, X., Illeperuma, W. R. K., Chaudhuri, O., Oh, K. H., Mooney, D. J., Vlassak, J. J., & Suo, Z. (2012). Highly stretchable and tough hydrogels. *Nature*, 489(7414), 133–136.

[160] Suo, Z. (2010). Theory of dielectric elastomers. *Acta Mechanica Solida Sinica*, 23(6), 549 – 578.

[161] Sutherland, R. L., Mäthger, L. M., Hanlon, R. T., Urbas, A. M., & Stone, M. O. (2008). Cephalopod coloration model. ii. multiple layer skin effects. *Journal of the Optical Society of America A*, 25(8), 2044–2054.

[162] Tattersall, H. G. & Tappin, G. (1966). The work of fracture and its measurement in metals, ceramics and other materials. *J. Mater. Sci.*, 1, 296–301.

[163] Taylor, M., Francesconi, L., Gerend□, M., Shanian, A., Carson, C., & Bertoldi, K. (2014). Low porosity metallic periodic structures with negative poisson's ratio. *Advanced Materials*, 26(15), 2365–2370.

[164] Timoshenko, S. (1935). Buckling of flat curved bars and slightly curved plates. *J. Appl. Mech.*, 2, 17–20.

[165] Timoshenko, S. & Gere, J. M. (1961). *Theory of elastic stability*. New York: McGraw-Hill, 2nd edition.

[166] Ting, T. & Chen, T. (2005). Poisson's ratio for anisotropic elastic materials can have no bounds. *The Quarterly Journal of Mechanics and Applied Mathematics*, 58(1), 73–82.

[167] Tirumala, V. R., Stafford, C. M., Ocola, L. E., Douglas, J. F., & Mahadevan, L. (2012). Geometric control of rippling in supported polymer nanolines. *Nano Lett.*, 12(3), 1516–1521.

[168] Triantafyllidis, N. & Maker, B. N. (1985). On the comparison between microscopic and macroscopic instability machanisms in a class of fibre-reinforced composites. *J. Appl. Mech. - T. ASME*, 52, 794–800.

[169] Triantafyllidis, N., Nestorovic, M. D., & Schraad, M. W. (2006). Failure surfaces for finitely strained two-phase periodic solids under general in-plane loading. *Journal of Applied Mechanics-Transactions of the Asme*, 73(3), 505–515.

[170] Vasseur, J. O., Djafari-Rouhani, B., Dobrzynski, L., Kushwaha, M. S., & Halevi, P. (1994). Complete acoustic band gaps in periodic fibre reinforced composite materials: the carbon/epoxy composite and some metallic systems. *J. Phys. Condesed Mat.*, 6, 8759.

[171] Vasseur, J. O., Hennion, A., Rouhani, B., Duval, F., Dubus, B., & Pennec, Y. (2007). Waveguiding in two-dimensional piezoelectric phononic crystal plates. *J. Appl. Phys.*, 101, 114904.

[172] Viedma, C. (2005). Chiral symmetry breaking during crystallization: Complete chiral purity induced by nonlinear autocatalysis and recycling. *Phys. Rev. Lett.*, 94(6), 065504.

[173] Vignolini, S., Yufa, N. A., Cunha, P. S., Guldin, S., Rushkin, I., Stefik, M., Hur, K., Wiesner, U., Baumberg, J. J., & Steiner, U. (2012). A 3d optical metamaterial made by self-assembly. *Advanced Materials*, 24(10), 23–27.

[174] Von Karman, T. (1910). Festigkeitsprobleme im maschinenbau. *Encyk. D. Math. Wiss. IV*.

[175] Wang, P., Shim, J., & Bertoldi, K. (2013). Effects of geometric and material non-linearities on the tunable response of phononic crystals. *Phys. Rev. B*, 88, 014304.

[176] Weintraub, M. (1952). Leaf movements in mimosa pudica l. *New Phytologist*, 50(3), 357–382.

[177] Wierzbicki, T. & Abramowicz, W. (1983). On the crushing mechanics of thin-walled structures. *J. Appl. Mech.*, 50(4a), 727–734.

[178] Wohlhart, K. (2001). New regular polyhedral linkages. *Proceedings of the Second Workshop on Computational Kinematics*, (pp. 239–248).

[179] Wojciechowski, K. & Branka, A. (1989). Negative poisson ratio in a two-dimensional "isotropic" solid. *Phys. Rev. A*, 40, 7222–7225.

[180] Wu, E. & Jiang, W. (1997). Axial crush of metallic honeycombs. *Int. J. Impact Eng.*, 19(5-6), 439–456.

[181] Xiaonan, H., Hong, H., & Vadim, S. (2012). A novel concept to develop composite structures with isotropic negative poisson's ratio: Effects of random inclusions. *Composites Science and Technology*, 72(15), 1848 – 1854.

[182] Yang, S., Khare, K., & Lin, P. C. (2010). Harnessing surface wrinkle patterns in soft matter. *Adv. Funct. Mater.*, 20, 2550.

[183] Yao, X., Hu, Y., Grinthal, A., Wong, T.-S., Mahadevan, L., & Aizenberg, J. (2013). Adaptive fluid-infused porous films with tunable transparency and wettability. *Nat. Mater.*, 12, 529–534.

[184] Yeh, H. & Zhang, R. (1999). A study of negative poisson's ratio in randomly oriented quasi-isotropic composite laminates. *Journal of Composite Materials*, 33(19), 1843–1857.

[185] Yeoh, O. H. (1993). Some forms of the strain energy function for rubber. *Rubber Chem. Technol.*, 66, 754–771.

[186] Yin, J., Cao, Z., Li, C., Sheinman, I., & Chen, X. (2008). Stress-driven buckling patterns in spheroidal core/shell structures. *Proceedings of the National Academy of Sciences*, 105(49), 19132–19135.

[187] Yoon, H., Ghosh, A., Han, J. Y., Sung, S. H., Lee, W. B., & Char, K. (2012). Lateral buckling of high aspect ratio janus nanowalls. *Adv. Funct. Mater.*, 22, 3723.

[188] Zhang, S., Park, Y. S., Li, J., Lu, X., Zhang, W., & Zhang, X. (2009). Negative refractive index in chiral metamaterials. *Phys. Rev. Lett.*, 102(2), 023901.

[189] Zhang, Y., Matsumoto, E. A., Peter, A., Lin, P. C., Kamien, R. D., & Yang, S. (2008). One-step nanoscale assembly of complex structures via harnessing of elastic instability. *Nano Lett.*, 8(4), 1192–1196.

[190] Zhou, X.-Z., Wang, Y.-S., & Zhang, C. (2009). Effects of material parameters on elastic band gaps of two-dimensional solid phononic crystals. *J. Appl. Phys.*, 106, 014903.

[191] Zupan, M., Chen, C., & Fleck, N. A. (2003). The plastic collapse and energy absorption capacity of egg-box panels. *Int. J. Mech. Sci.*, 45, 851–871.

This thesis was typeset using LaTeX, originally developed by Leslie Lamport and based on Donald Knuth's TeX. The body text is set in 11 point Egenolff-Berner Garamond, a revival of Claude Garamont's humanist typeface.

The above illustration, "Science Experiment 02", was created by Ben Schlitter and released under CC BY-NC-ND 3.0. A template that can be used to format a PhD thesis with this look and feel has been released under the permissive MIT (XII) license, and can be found online at github.com/suchow/Dissertate or from its author, Jordan Suchow, at suchow@post.harvard.edu.